# HIGH PERFORMANCE TRIBOELECTRIC NANOGENERATOR AND ITS APPLICATIONS

A Dissertation
Presented to
The Academic Faculty

by

Changsheng Wu

In Partial Fulfillment
of the Requirements for the Degree
DOCTOR OF PHILOSOPHY in the
SCHOOL OF MATERIALS SCIENCE AND ENGINEERING

Georgia Institute of Technology
AUGUST 2019

# HIGH PERFORMANCE TRIBOELECTRIC NANOGENERATOR AND ITS APPLICATIONS

Approved by:

Dr. Zhong Lin Wang, Advisor
School of Materials Science and Engineering
*Georgia Institute of Technology*

Dr. C. P. Wong
School of Materials Science and Engineering
*Georgia Institute of Technology*

Dr. Meilin Liu
School of Materials Science and Engineering
*Georgia Institute of Technology*

Dr. Younan Xia
Department of Biomedical Engineering
*Georgia Institute of Technology*

Dr. David L. McDowell
School of Materials Science and Engineering
*Georgia Institute of Technology*

Date Approved: [April 25, 2019]

To my family and friends

# ACKNOWLEDGEMENTS

Firstly, I would like to express my sincere gratidue to my advisor Prof. Zhong Lin Wang for his continuous support and invaluable guidance in my research. As an exceptional researcher, he is my role model for his thorough knowledge in physics and nanotechnology, indefatigable diligence, and overwhelming passion for scientific innovation. It is my great fortune and honor in having him as my advisor and learning from him in the past four years. I would also like to thank the rest of my committee members, Prof. Liu, Prof. McDowell, Prof. Wong, and Prof. Xia for their insightful advice on my doctoral research and dissertation.

My sincere thanks also go to my fellow lab mates for their strong support and help. In particular, I would not be able to start my research so smoothly without the mentorship of Dr. Long Lin, when I joined the group without much knowledge in the field of nanogenerator. It is fortunate for me to have a close collaboration and friendship with Dr. Wenbo Ding, whose expertise in signal processing and data analysis is indispensable for my works related to human machine interfacing. Besides, I would like to thank Drs. Yunlong Zi, Jie Wang, Hengyu Guo, Peng Jiang, Ruiyuan Liu, Qiu Jiang, Yejing Dai, Jisu Jiang, Xin Wang, Jiyu Wang, Tiejun Zhang, Dong Lin, and many other for their kind help.

Last but not least, I would like to thank my family for their selfless love and endless support. My parents have given me the best they have during my growing up,

and without their spiritual and financial support, my academic journey till today would not be possible. I would also like to take this chance to memorize my grandparents, who enlightened me the significance of knowledge and planted the seeds of being a scientist when I was young. My deepest gratitude goes to my wife, Lisha Liu, who has gone through the difficulties and happiness together with me throughout my Ph.D. life. Her accompany will be my biggest treasure for the rest of my life.

# TABLE OF CONTENTS

# LIST OF FIGURES

# LIST OF SYMBOLS AND ABBREVIATIONS

| | |
|---|---|
| AC | alternating current |
| Ag | Silver |
| Al | aluminum |
| CCD | charge coupled device |
| CRT | cathode ray tube |
| Cu | copper |
| DC | direct current |
| EMG | electromagnetic generator |
| HMI | human machine interfacing |
| HV | high voltage |
| LED | light-emitting diode |
| NW | nanowire |
| PENG | piezoelectric nanogenerator |
| PET | polyethylene terephthalate |
| PTFE | polytetrafluoroethylene |
| PU | polyurethane |
| RPM | Revolutions per minute |
| TDD | transdermal drug delivery |
| TENG | triboelectric nanogenerator |

# SUMMARY

As the world is marching into the era of the internet of things (IoT) and artificial intelligence, the most vital development for hardware is a multifunctional array of sensing systems, which forms the foundation of the fourth industrial revolution towards an intelligent world. Given the need for mobility of these multitudes of sensors, the success of the IoT calls for distributed energy sources, which can be provided by solar, thermal, wind, and mechanical triggering/vibrations. The triboelectric nanogenerator (TENG) for mechanical energy harvesting developed by Z.L. Wang's group is one of the best choices for this energy for the new era, since triboelectrification is a universal and ubiquitous effect with an abundant choice of materials. The development of self-powered active sensors enabled by TENG is revolutionary compared to externally powered passive sensors, similar to the advance from wired to wireless communication.

In this work, fundamental performance-limiting factors of TENG were studied and various strategies, such as the optimization of materials, structures and operation environment, were investigated to enhance its electrical outputs. Furthermore, the application of TENG in three major fields, including micro/nano power sources, self-powered sensors, and direct high voltage (HV) power sources, was explored. Self-powered electrically-assisted transdermal drug delivery driven by biomechanical motions was demonstrated for non-invasive, on-demand drug administration with feedback control. Self-powered wireless optical transmission of mechanical agitation signals was proposed to solve the issue of power supply for optical wireless communications. Smart keyboard with active pressure sensing was developed for keystroke dynamics-based cyber security.

The HV of TENG was successfully applied to drive field emission of electrons and electrohydrodynamic jet printing, with unique merits of low cost, enhanced safety and portability. With solid understanding of both the fundamentals and applications, a roadmap is proposed for the research and commercialization of TENG in the next 10 years. This work not only provides insights and solutions for developing high performance TENG, but also broadens its application in a variety of multidisciplinary fields that have a huge impact on people's daily life in the era of IoT.

# CHAPTER 1. INTRODUCTION OF TRIBOELECTRIC NANOGENERATOR

The triboelectric effect is ubiquitous in our everyday life and results from two different materials coming into contact. It is generally regarded as a negative effect in industry given that the electrostatic charges induced from it can lead to ignition, dust explosions, dielectric breakdown, electronic damage, etc. From an energy point of view, those electrostatic charges constitute a capacitive energy device when the two triboelectric surfaces are separated, which led to the invention of early electrostatic generators such as the "friction machine" and Van de Graaff generator.[1] By coupling this triboelectric effect and electrostatic induction, the triboelectric nanogenerator (TENG) was first invented by the Wang group in 2012 to effectively harness ambient mechanical energy that is ubiquitous but usually wasted in our everyday life.[2] More specifically, triboelectrification/contact electrification provides static polarized charges on material surfaces in contact, while electrostatic induction drives the transformation of mechanical energy to electricity through the change in electrical potential induced by mechanically-agitated separation. Over the past 6 years, this TENG concept has been expanded to different working modes[3-8] to enable broad application scenarios, such as mechanical vibrations, human motions, wind and water waves.[9, 10]

In addition to versatile operation modes, the TENG has many other merits, including broad material availability, light weight, low cost, and high efficiency even at low operation frequencies. In principle, any material with distinct charge affinity can be used to construct a TENG, which results in a broad range of materials at opposite ends of

the triboelectric series capable of high performance. Among them, polytetrafluoroethylene (PTFE) and silicone are commonly used materials for attaining net negative triboelectric charges while nylon and metal are for net positive charges. Most current TENGs are polymer-based and flexible, easy to fabricate, cost-effective and highly portable,[11] while high-temperature TENGs are built from durable ceramics materials for extreme conditions of operation.[12, 13] Moreover, the power density of a TENG, which depends on the device structure and active materials, has been reported to be up to 500 $W/m^2$.[14] The energy harvested using TENG is sufficient to drive many small electronics and make self-powered electronics networks viable. Given the enormous number of sensors required in the era of internet of things (IoT) and existing environmental concerns associated with battery replacement on a large scale, TENG will potentially serve as a new alternative energy source of great significance and thus have also been proposed as "the energy for the new era" in 2017.[15]

### 1.1 Theoretical Origin and Model of TENG

The first TENG device, whose contact-separation design is still the basis of most current ones, consisted of a polyethylene terephthalate (PET) film and Kapton film with back electrodes coated on them (Figure 1a).[2] The device could generate AC output when the contact status between the two films changed, i.e. when it underwent cyclic pressing or bending motion. The initial explanation of the working mechanism was described in a qualitative manner. When the two active triboelectric materials, PET and Kapton, come into contact under pressing or bending, triboelectric charges will be induced on their surfaces. As the external force is released, the charged surfaces will be separated, and an electric potential difference will be built upon the two back electrodes. If the electrodes are

connected to external load, current will flow between them to screen out the electric field built up by the charged surfaces. As they are brought into contact again by external mechanical stimuli, the potential difference on the electrodes will change and current will flow back in the opposite direction. A continuous alternating current (AC) output can be obtained by repeating this operation cycle. In other words, the device operates on the coupling of two commonly observed phenomena, contact electrification and electrostatic induction, with the former providing the static polarized charges on material surfaces and the latter driving the transformation of mechanical energy to electricity via mechanically triggered change in electric potential. This qualitative description provides a straightforward understanding of contact separation TENG, but the fundamental physics model has been lacking until the mechanism origin was traced back to Maxwell's displacement current in 2017.[15, 16] Maxwell's displacement current is defined

$$\boldsymbol{J}_D = \frac{\partial \boldsymbol{D}}{\partial t} = \varepsilon \frac{\partial \boldsymbol{E}}{\partial t} + \frac{\partial \boldsymbol{P}_S}{\partial t} \tag{1}$$

where $\boldsymbol{D}$ is the displacement field, $\varepsilon$ is the permittivity of the medium, $\boldsymbol{E}$ is the electric field, and $\boldsymbol{P}_S$ is the polarization contributed by the presence of surface polarization charges contributed from piezoelectric and or triboelectric effect. The first term refers to a time-varying electric field and is tied to the origin of electromagnetic waves, while the second term presents the contribution from surface polarization and is the origin of nanogenerators. More specifically, in the piezoelectric nanogenerator (PENG), this polarization comes from piezoelectric polarization charges generated by applied strain. In TENG, external electrostatic charges induced from triboelectrification build up time-varying surface polarization as two materials in contact undergo mechanically agitated displacement.

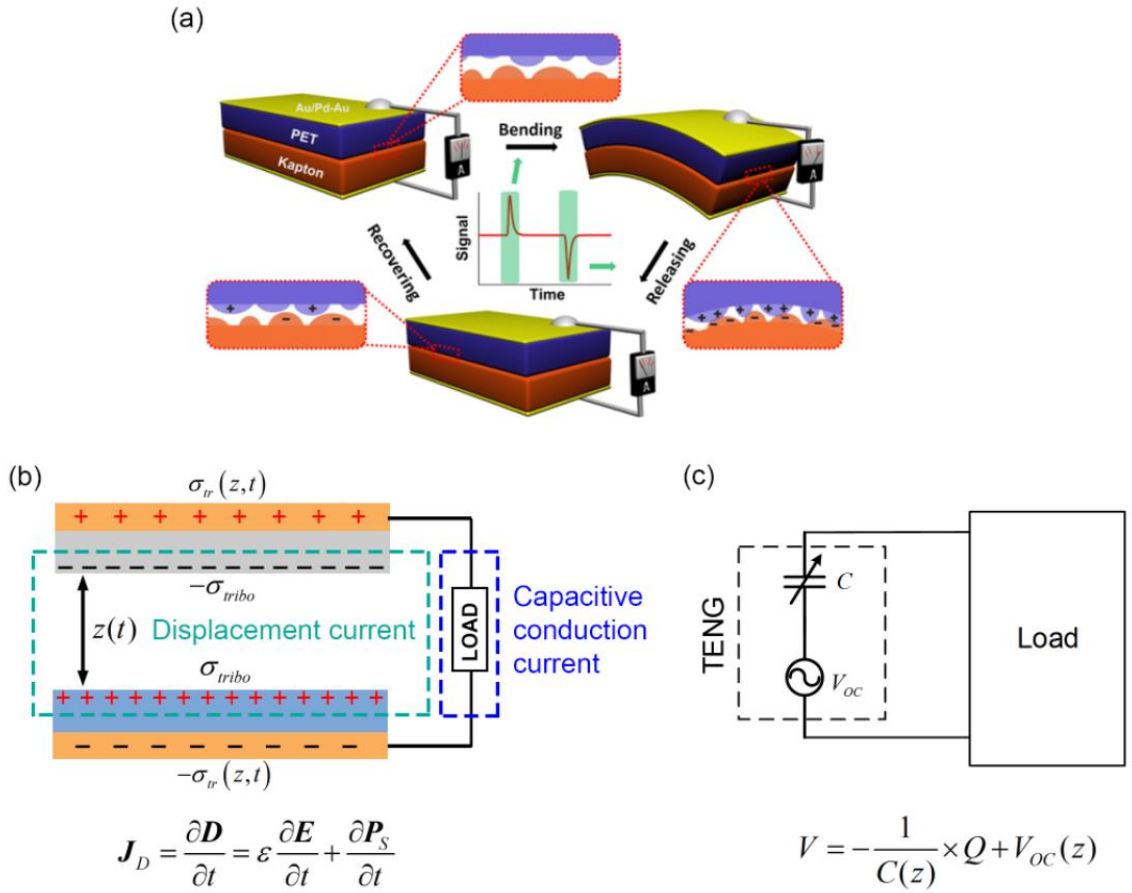


**Figure 1. Theoretical models of TENG.** (a) Schematic illustration of the first TENG and its operation cycle. Reproduced with permission.[2] Copyright 2012, Elsevier. (b) The displacement current model of a contact-separation-mode TENG. (c) The equivalent electrical circuit model of TENG. Reproduced with permission.[17] Copyright 2018, Wiley-VCH.

The basic model of a contact-separation-mode TENG is illustrated in Figure 1b. It has two electrodes connected to the external load and two dielectrics for contact electrification. The dielectric surfaces are oppositely charged due to contact electrification with a surface charge density of $\pm\sigma_{tribo}$, which is saturated after the initial contact cycles and independent of the gap distance *z*. The triboelectric charges build up an electrostatic field, which drives free electrons to flow through the external load and transfer between the electrodes. The amount of transferred charges accumulated on the electrodes, $\pm\sigma_{tr}$, is

a function of *z*, and thus, the mechanical energy which induces change in *z* is converted into electrical energy. The corresponding displacement current can be calculated as

$$J_D = \frac{\partial D_z}{\partial t} = \frac{\partial \sigma_{tr}(z,t)}{\partial t} \tag{2}$$

This displacement current is the only conduction mechanism for electricity transport in capacitive conduction and leads to the output current of TENG via electromagnetic waves and induction, rather than the flow of free charges directly across the electrodes as in a resistor.

Oppositely charged surfaces with a changing gap distance can be viewed as a capacitor with varying capacitance. This perspective gives a more intuitive representation of the TENG using the capacitor model (Figure 1c), whose current is given by

$$I = \frac{dQ}{dt} = A\frac{d\sigma_{tr}}{dt} \tag{3}$$

The result is equivalent to Equation 2 and validates that Maxwell's displacement current is the foundation of the capacitive model. The corresponding output voltage of TENG can be written as

$$V = -\frac{1}{C(z)} \times Q + V_{OC}(z) \tag{4}$$

Along with Ohm's law, this capacitive model of TENG is the theoretical tool that enables the study, design and optimization of TENG.[18-23] Another model using the distance-dependent electric field concept and Norton's theorem has also been proposed recently to more accurately simulate the output behavior of a TENG with an external

load.[24, 25] However, it should be emphasized that Maxwell's displacement current is the fundamental basis for all of these detailed electrical models.

## 1.2 Four Working Modes of TENG

Depending on the direction of the polarization change and electrode configuration, four different operation modes of the TENG have been proposed since its first report in 2012, including vertical contact-separation (CS) mode, lateral-sliding (LS) mode, single-electrode (SE) mode, and freestanding triboelectric-layer (FT) mode, as shown in Figure 2.[3] The vertical CS mode uses relative motion perpendicular to the interface, and the potential change between electrodes and thus external current flow is dictated by the gap distance between material surfaces. The lateral-sliding mode uses the relative displacement in the direction parallel to the interface, and it can be implemented in a compact package via rotation-induced sliding. The single-electrode mode takes the ground as the reference electrode and is versatile in harvesting energy from a freely moving object without attaching an electric conductor, such as a hand typing, human walking, and moving transportation. The freestanding triboelectric-layer mode is developed upon the single-electrode mode, but instead of using the ground as the reference electrode, it uses a pair of symmetric electrodes and electrical output is induced from asymmetric charge distribution as the freely moving object changes its position. One thing worth noting is that practical application of TENG is not limited to one single mode, but relies more on conjunction or hybridization of different modes to harness their full advantages. The theoretical models of all four modes have been extensively studied and can be found in previous publications.[18, 19, 21, 26, 27]

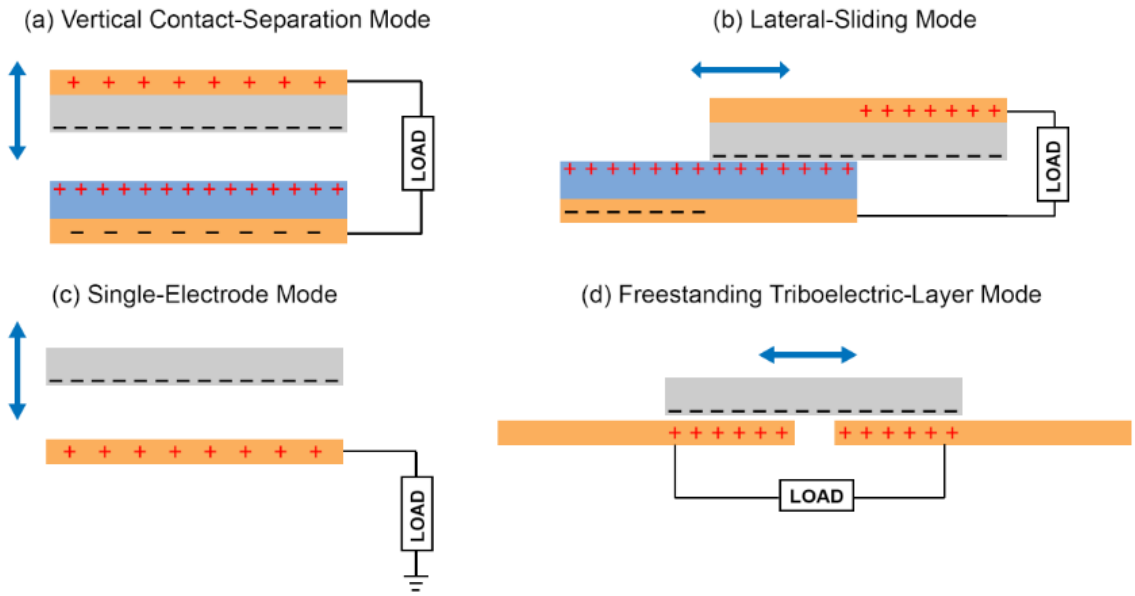


**Figure 2. Four working modes of TENG.** (a) Vertical CS mode. (b) LS mode. (c) SE mode. (d) FT mode. Reproduced with permission.[17] Copyright 2018, Wiley-VCH.

### 1.3 Major Applications of TENG

The major applications of TENG can be categorized into four areas (Figure 3): sustainable micro power sources for self-powered systems; active sensors for medical, infrastructure, environmental monitoring and human machine interfacing (HMI); basic networks units for harvesting low-frequency water energy towards large-scale blue energy; and direct power sources for high voltage (HV) instruments.

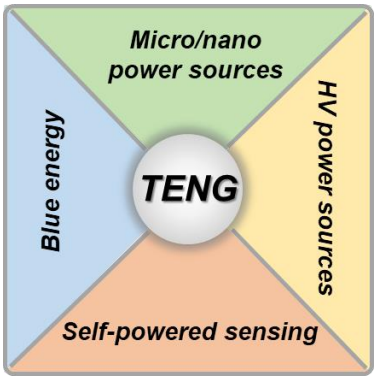


**Figure 3. Major application fields of TENG.** Reproduced with permission.[17] Copyright 2018, Wiley-VCH.

Firstly, thanks to its merits such as light weight, low cost, and abundant material and structural choices, the TENG has found vast applications as micro power sources for self-powered systems by harvesting biomechanical or ambient energy, such as human walking, heartbeats, machine vibration, and wind energy. Due to its superior performance at low frequencies, biomechanical energy harvesting using TENG is of great importance and has been explored since the very beginning phase of TENG development, with smart backpack,[28, 29] self-powered watch,[30] and acoustic energy harvester[31, 32] demonstrated. Secondly, since the TENG can transform mechanical stimuli to electrical signals directly without additional transducers, it has great potential in the field of active sensing and self-powered sensors, which requires less, if not zero, standby power consumption and simpler control circuits compared to traditional passive transistors. Relevant pioneering works include tactile touch sensors,[33-35] acoustic sensors,[31, 32, 36, 37] motion and acceleration sensors,[38-40] and chemical sensors.[41-44] Meanwhile, with the rapid growth of IoT,[45, 46] TENG has also found promising application in advanced HMI that can enable convenient, safe and novel communication between humans and external devices.[47, 48] Thirdly, the application of TENG in harvesting natural mechanical energy, such as wind energy,[49-52]

raindrop energy,[53-55] ultrasonic energy,[56] and water wave energy,[57-59] has attracted numerous research interests. Among them, the concept of using a TENG to harvest the kinetic energy of water waves in the vast oceans, i.e. blue energy,[15, 60] is particularly important, since recent studies suggest that a TENG is more effective than an electromagnetic generator (EMG) when it comes to harvesting low-frequency (<5 Hz) vibration energy.[61] Coupled TENG networks were proposed to harvest the blue energy in a large scale. It was projected that a 3D TENG network covering an ocean area the size of the US state of Georgia, spaced every 10 centimetres and stretching 10 metres deep beneath the surface, could meet the world's energy consumption today, if each unit produces a power about 1-10 mW.[60] Fourthly, The intrinsic characteristics of HV and low current renders the TENG as a novel alternative of conventional HV power sources with unprecedented portability and safety. With an easily obtainable HV of 1-10 kV, the TENG-based HV sources usually do not require sophisticated power converters, which greatly reduces the system complexity and cost. Given the limited charge transfer per operation cycle, the ideal HV application of TENG should have little requirements on current so that comparable, if not better, performance can be achieved when compared to conventional sources. Also, the lower current poses much less threat to the safety of personnel and instruments since HV could not be maintained once the limited charge is transferred.

### 1.4 Current Status around the Globe

Together with the PENG invented by the Wang group in 2006, the emerging nanogenerator technology has been widely regarded as a revolution in the field of energy harvesting and sensing, and has yielded about 195 patents.[62] Its trends, impacts and strategies towards large-scale commercialization have been studied using various

methods,[62-66] such as bibliometrics, patent analysis, tech mining, techno-economic lifetime assessment, and technology road-mapping, with the results showing that nanogenerator development is becoming more interdisciplinary and calls for efforts not only from materials science and nanotechnology, but also from computer science, information systems, public policy and many others. The international conference on Nanogenerators and Piezotronics (NGPT) was initiated in 2012 and has been held every two years ever since, with the number of attendees rising from 50 in 2012 to ~400 in 2018 and the host location switching between North America, Asia and Europe. A prestigious peer-reviewed journal, Nano Energy, was founded by the inventor of TENG, Prof. Z.L. Wang in 2012, to promote the development of nanomaterials-related energy solutions, among which the nanogenerator is an important subject. As of now, the TENG has displayed increasingly rapid development and has become the forerunner of growth in the nanogenerator field. The number of TENG-related publications has seen an exponential increase from only 8 in 2012 to about 400 in 2017, with authors hailing from over 40 countries. Several TENG-based commercial products, such as air filters[67] and face masks,[68] have been launched in local markets of China, which pioneer and pave the path towards large-scale commercialization.

## 1.5 Dissertation Scope

Despite the active research and rapid development of TENG around the globe, the technology is still in its infant phase and its practical large-scale application calls for more fundamental and technical advances. The output power density, one of the most critical parameters for energy harvesters, of TENG is limited by its intrinsic HV and low-current characteristics, while material challenges, including but not limited to flexibility,

stretchability, transience and durability, need to be addressed for a wide variety of circumstances. Furthermore, novel applications which rely more on voltage and pose little requirement on current are to be pursued in order to take full advantage of the TENG technology.

In my doctoral research, I am dedicated to developing high performance TENG and exploring its novel applications, with the aim of providing accessible and affordable solutions for fundamental challenges of energy sustainability in the era of IoT. The fundamental performance-limiting factors of TENG, such as air breakdown and mechanical energy loss, have been investigated, and corresponding solutions that can improve its output density by one order of magnitude have been proposed and demonstrated. Materials design using kirigami structures and functional polymers has been adopted to achieve TENG with unique mechanical property and functionality, which greatly broadens its applicability. Moreover, novel applications of TENG for self-powered systems, active sensing and HV instruments have been explored, with huge impact on various multidisciplinary fields ranging from biomedical treatment and advanced HMI to printed electronics and field emission.

# CHAPTER 2. HIGH PERFORMANCE TENG

The TENG technology is still in its infant phase in spite of those successful demonstrations ranging from mechanical energy harvesting to self-powered active sensing. Practical application of TENG for energy harvesting is greatly hindered by its limited output power density due to the intrinsic HV and low-current characteristics, while material challenges exist when novel applications call for certain functionalities such as stretchability and transience.

## 2.1 Achieving Ultrahigh Triboelectric Charge Density for Efficient Energy Harvesting

As an energy harvester, the commercialization and application of TENG highly depend on their power density, which is quadratically related to the triboelectric charge density. Therefore, large efforts have been devoted to increasing the amount of triboelectric charges by means of material improvement, structural optimization, surface modification, and so on. Artificial injection of ions, for example, by using corona discharging, was considered a straightforward way to increase the charge density, resulting in a high output charge density of 240 $\mu C/m^2$, but long-term stability remains an issue. [69] Very recently, a high-output charge density of 250 $\mu C/m^2$ was realized on a TENG through elastomeric materials and a fragmental contact structure [70] Nevertheless, the achievable output charge density has still been limited by the phenomenon of air breakdown in all previous studies. In this work, we report a method for increasing the triboelectric charge density by coupling surface polarization from triboelectrification and hysteretic dielectric polarization from ferroelectric material in vacuum ($P \sim 10^{-6}$ torr). Without the constraint of air breakdown, a

record-high triboelectric charge density of 1003 μC/m$^2$, which is close to the limit of dielectric breakdown, has been attained.

### *2.1.1 Air Breakdown Effect in TENG*

Typically, a simple TENG consists of two metal electrodes and a dielectric film, for example, a top copper (Cu) film and a bottom PTFE film with a back electrode attached to it (Figure 4a). When the two films are in contact, the Cu film and the PTFE film acquire net positive and net negative triboelectric charges respectively. When separated, the resulted charge separation will induce potential difference across the two Cu electrodes and subsequently current flow if the device is connected to an external circuit. The current flow is reversed when the two charged surfaces are brought into contact again[10]. In particular, a very high electrostatic field can be built between the two separated surfaces with opposite triboelectric charges, i.e., the top Cu film and the bottom PTFE film. The potential distribution between such two films can be numerically simulated using the finite-element method via the commercial software COMSOL. With a gap distance of 1 cm between the Cu and PTFE films and a surface charge density of 50 μC/m$^2$, as commonly seen in TENG, a high gap voltage ($V_{gap}$) of $2.6\times10^4$ V will occur (Figure 4b). This amount of surface charge density is adequate to give discrepancy between initial injected and final output charge density measured from a TENG connected to an external load of 100 GΩ, which confirms the existence of air breakdown phenomenon in TENG even with a low charge density under large load condition (Figure 4c). Under short-circuit condition, due to the easier charge transfer process through external circuit, $V_{gap}$ would be lower compared to other load conditions and the charge density threshold of air breakdown would be higher. In Figure 4d, an initial high charge density of 300 μC/m$^2$ is obtained via ionized-air

injection, and the maximum achieved output charge density under short circuit condition is limited to 160 μC/m$^2$ by air breakdown and decreases to 140 μC/m$^2$ within 8 s. Under any load condition, therefore, the existence of air breakdown greatly limits the maximum retainable charge density in TENG as well as other triboelectrification applications.

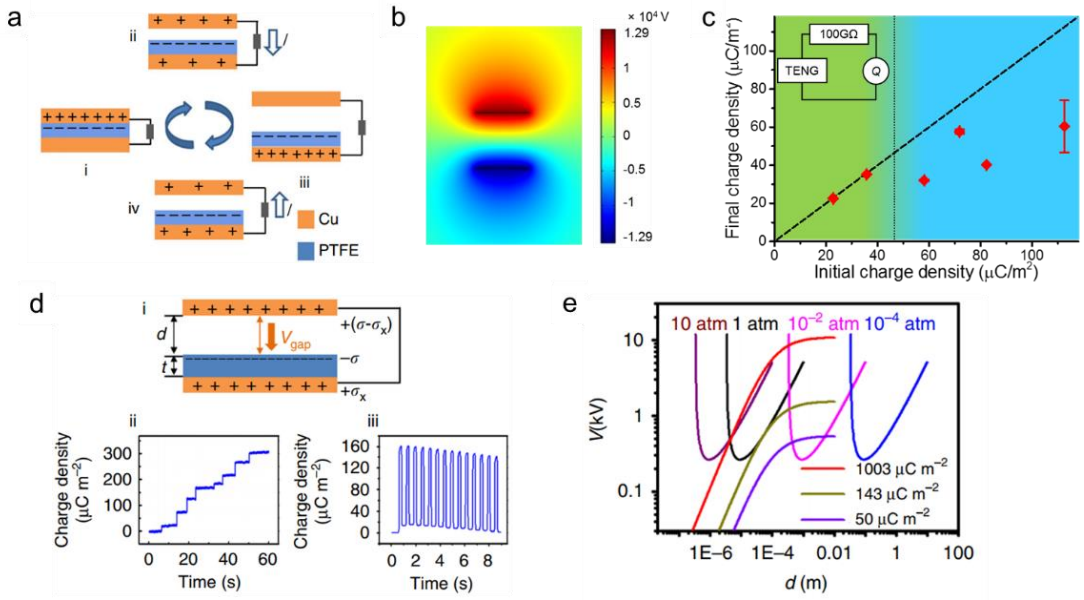


**Figure 4. Air breakdown effect in TENG.** (a) Working principle of a contact-separation-mode TENG. (b) COMSOL simulation of the potential distribution between two charged surfaces (charge density 50 μC/m$^2$, gap distance 1 cm). (c) The existence of air breakdown in TENG even at low surface charge density under open-circuit condition. (d) Air breakdown in TENG under short-circuit condition after ion injection. Bottom-left insert records the in-situ measurement of the charge flow from the ground to the bottom electrode of the PTFE film during the step-by-step ion injection process; bottom-right insert plots the charge transfer between the two electrodes of TENG operating after the ion injection. (e) Air breakdown voltage at different pressures and gap voltage of TENG with different charge densities. The thickness of PTFE film is 200 μm. Reproduced with permission.[71] Copyright 2017, Springer Nature.

Paschen's law describes the empirical relationship between the gaseous breakdown voltage ($V_b$) and the product of the gas pressure ($P$) and gap distance ($d$), and is given by

$$V_b = \frac{APd}{\ln(Pd) + B} \tag{5}$$

where $A$ and $B$ are the constants determined by the composition and the pressure of the gas. For air at standard atmospheric pressure (atm, i.e. the conventional operation condition of a TENG), $A = 2.87 \times 10^5$ V/(atm·m), and $B = 12.6$.

According to the theoretical derivation,[69] the gap voltage between contact surfaces of a Cu-PTFE TENG ($V_{gap}$) under short-circuit condition is given by

$$V_{gap} = \frac{t\sigma d}{\varepsilon_0 (t + d\varepsilon_r)} \tag{6}$$

where $t$ is the thickness of the PTFE film, $\sigma$ the triboelectric surface charge density, $\varepsilon_r$ the relative permittivity of PTFE ($\varepsilon_r \sim 2.1$), and $\varepsilon_0$ the vacuum permittivity ($\varepsilon_0 \sim 8.85 \times 10^{-12}$ F/m).

Figure 4e plots the $V_b$ of air at different pressures and $V_{gap}$ of TENG with different charge densities. To avoid air breakdown, the $V_{gap}$ must be smaller than $V_b$ at any operation gap distance ($0 < d < d_{max}$). A simple glance at the curves and equations reveals that either increasing the gaseous pressure (left-shifting the Paschen Curve) or changing to a gas with higher dielectric strength (up-shifting the Paschen Curve) will allow larger gap voltages without breakdown. However, such improvement is limited and may induce severe safety concerns, such as explosions and leaking of harmful gases. A more effective way is to shift the Paschen's curve towards the right by decreasing the air pressure. Initially as the pressure decreases, the maximum charge density allowed without breakdown would

decrease; once the distance at which the minimum breakdown voltage occurs passes the maximum operation range of TENG, the maximum charge density allowed would increase. In particular, when the pressure is so low that the whole operation range is outside of the region where the Paschen's law holds valid, there would be no concern about avalanche breakdown that would limit the retainable charge density. Therefore, the performance of TENG under high vacuum is studied and the results are presented in the following sections.

### *2.1.2 Output Performance of TENG in Vacuum*

According to our previous report, soft contact and fragmental structure can enhance the output performance of TENG. Hence a TENG with a cushioned Cu electrode and a contact area smaller than conventional TENG was fabricated as the starting point of our study, with its schematic illustrated in Figure 5a. While in contact, the foam conforms to the mechanical stress and thus improves the contact intimacy between the Cu electrode and PTFE. As a result, the triboelectric charge density of the TENG in air measures up to 120 $\mu C/m^2$ (Figure 5b). When the same cushioned TENG is operated in vacuum ($P \sim 10^{-6}$ torr), the air breakdown depicted by Paschen's law is avoided and the triboelectric charge density is boosted from 120 $\mu C/m^2$ to 660 $\mu C/m^2$ (Figure 5b). Accordingly, the open-circuit voltage increases from 20 V to 100 V (Figure 5c), the peak of short-circuit current rises from 60 $mA/m^2$ to 300 $mA/m^2$ (Figure 5d), and the maximum output power density is enhanced from 0.75 $W/m^2$ (Figure 5e) to 16 $W/m^2$ (Figure 5f) with the match-load of 20 MΩ at a fairly low frequency of 2 Hz. Experimental results also show that the performance enhancement of TENG using high vacuum is not limited by the thickness of the dielectric film.

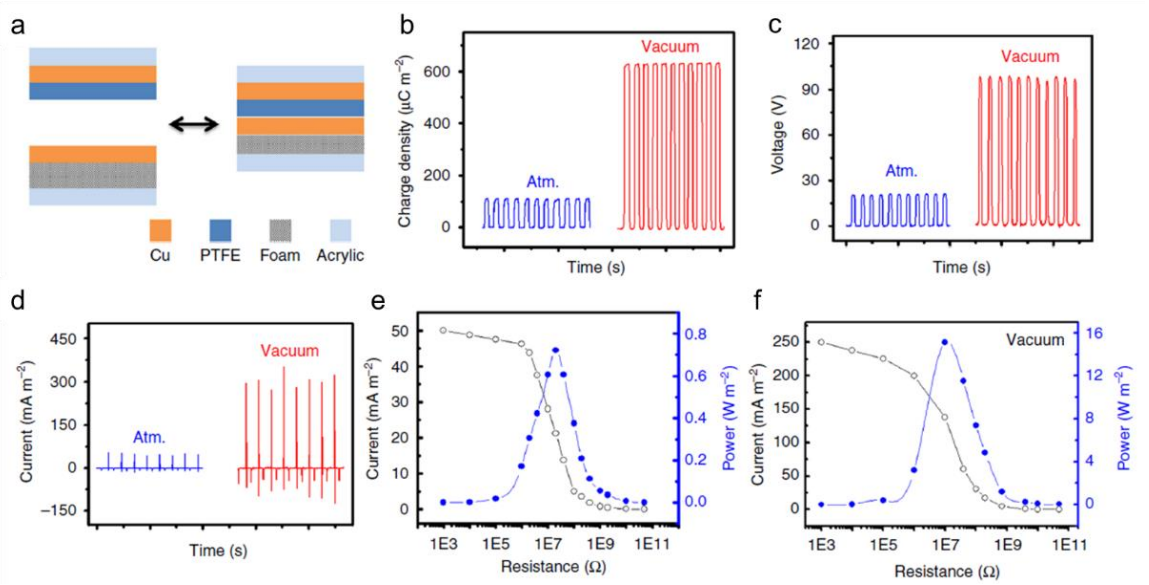


**Figure 5. Output performance of TENG in the vacuum.** (a) Schematic of TENG with a cushioned Cu electrode to increase contact intimacy during operation process. (b-d) Charge density (b), open-circuit voltage (c), and short-circuit current (d) of the TENG in atmosphere and high vacuum ($P \sim 10^{-6}$ torr). (e,f) Current density and power density of TENG with various loads in atmosphere (e) and vacuum (f). Reproduced with permission.[71] Copyright 2017, Springer Nature.

### *2.1.3 Performance Enhancement of TENG via Coupling of Surface and Dielectric Polarization*

Although the exact origin of triboelectrification is still under debate, it is known that materials with higher electron affinity, i.e., better capability of trapping electrons, can acquire more negative charges during the contact electrification process. Previous publications have reported the use of surface modification, the introduction of electric double layer effect, and the addition of a charge transport layer to enhance the triboelectric charges. Meanwhile, ferroelectric materials are known to have residual dielectric polarization after being exposed to an electrical field. The residual polarization, if properly coupled with the surface polarization on triboelectric materials, can be expected to enhance its ability to capture charges. Herein a new method of increasing triboelectric charge

density by introducing built-in dielectric polarization using ferroelectric material is proposed, and its working principle is schematically illustrated in Figure 6a. The TENG consists of a top triboelectric Cu electrode (denoted as Cu-I), a PTFE film adhered to a ferroelectric material layer, and a back Cu electrode at the bottom (denoted as Cu-II). When Cu-I and PTFE are in contact, they will acquire net opposite charges on their surfaces (i). Once Cu-I is separated from the PTFE film, the induced potential between two charged surfaces, or surface polarization, will result in a dielectric polarization inside the ferroelectric layer. Under short-circuit condition, the resultant surface polarization will also drive the positive charges on Cu-I to Cu-II (ii), until the gap increases to the maximum and an equilibrium is reached (iii). As the Cu-I approaches the PTFE, the decreased surface polarization will drive the positive charges on Cu-II back to Cu-I (iv) until Cu-I and PTFE are in contact again. Due to dielectric hysteresis, however, the polarization inside the ferroelectric material will not fully diminish, and the residual built-in dielectric polarization will act as a negative charge trap to enhance the PTFE's capability of capturing charges during contact electrification (v). In other words, the surface polarization from triboelectrification will induce built-in dielectric polarization inside the ferroelectric material, while the latter will enhance the former in subsequent contact electrification processes until an equilibrium is reached (x). This coupling of surface and dielectric polarization will greatly enhance the amount of triboelectric charges that can be generated during the operation of TENG.

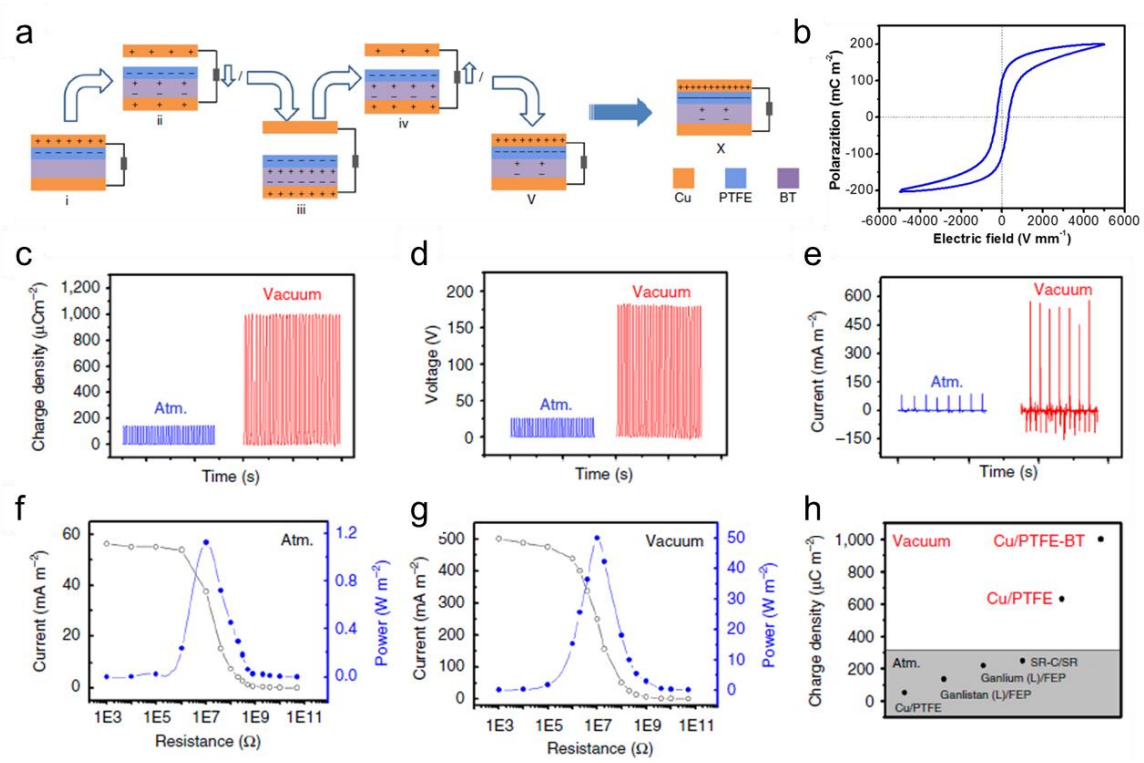


**Figure 6. Working mechanism and output performance of TENG with the coupling of surface and dielectric polarization.** (a) Working mechanism of the TENG with the integration of triboelectric material PTFE with ferroelectric material BT. (b) P-E hysteresis loop of the BT ceramics. (c-e) Charge density (c), open-circuit voltage (d), and short-circuit current (d) of the TENG in atmosphere and high vacuum. (f,g) Current density and power density of TENG with various loads at atmosphere (f) and vacuum ($P \sim 10^{-6}$ torr) (g). (h) Comparison of the output charges density measured in this work with previously reported ones. Reproduced with permission.[71] Copyright 2017, Springer Nature.

To validate the proposed mechanism, one kind of ZnO doped barium titanate (BT) material was used as the ferroelectric material. The TENG has a circular contact area with a diameter of 1 cm, and its output performance are presented in Figure 6(c-e). The output charge density is enhanced from 142 μC/m$^2$ in air to 1003 μC/m$^2$ in high vacuum ($10^{-6}$ torr), and accordingly, the open circuit voltage increases from 26 V to 180 V and the peak of short-circuit current rises from 80 mA/m$^2$ to 570 mA/m$^2$. The maximum output power density, with a load of 10 MΩ, is elevated from 1.1 W/m$^2$ to 50 W/m$^2$, which is over 45-fold enhancement (Figure 6(f-g)). It should be noted that with only BT as the bottom

triboelectric layer, the triboelectric charge density is lower than 15 μC/m$^2$ in atmosphere, while that with only PTFE is 120 μC/m$^2$. By integrating PTFE with BT, on the other hand, the charge density is 142 μC/m$^2$ in atmosphere, around the theoretical limitation of air breakdown, and a record high of 1003 μC/m$^2$ in high vacuum without air breakdown. The results are clear evidence of the synergistic effect between surface and dielectric polarization. This mechanism opens a new paradigm for TENG optimization via coupling surface polarization from triboelectrification and hysteretic dielectric polarization from ferroelectric material.

The selected milestone of TENG development is summarized in Figure 6h. Initially, the triboelectric charge density of TENG based on Cu and PTFE is around 50 μC/m$^2$. The value is improved to 134 μC/m$^2$ and 219 μC/m$^2$ when liquid metal galinstan and gallium, instead of Cu, are used respectively, due to better contact intimacy.[72] Inspired by liquid metal, soft material and fragmental contacting structure (silicon rubber mixed with carbon materials, SR-C) reach 250 μC/m$^2$.[70] In this work, the charge density in high vacuum is enhanced to 660 μC/m$^2$ simply with a cushioned Cu electrode and a fragmental structure, and further elevated to 1003 μC/m$^2$ by integrating PTFE with ferroelectric BT. Compared with the 50 μC/m$^2$ of the conventional TENG, the output triboelectric charge density has been boosted by 20-fold.

### *2.1.4 Application of TENG Working in Vacuum*

The elevated output performance of a TENG with a soft contact area of 5 cm × 5cm in high vacuum was demonstrated through driving various electronics together with an energy storage unit. Here, a supercapacitor of 1.2 mF was used. Figure 7a presents the

circuit diagram of the self-powered system, where the TENG and the supercapacitor are connected by a full-wave rectifier. The voltage of the supercapacitor is monitored by a voltmeter. When switch K1 is on and switch K2 is off, the voltage of the supercapacitor is increased by 21.49 mV after charged by the TENG in atmosphere for 10 s (Figure 7b), and the equivalent galvanostatic current ($I_{eg}$) can be calculated as 2.5 μA. When the same TENG works in high vacuum (P ~ $10^{-6}$ torr), the voltage of the supercapacitor is increased by 80.36 mV in the same time period (means 4.8 V in 10 minutes), delivering an $I_{eg}$ of 9.6 μA, which is around 4 times of that in atmosphere. Thanks to the elevated output performance in high vacuum, when an electronic watch is connected as the load, the supercapacitor can still be charged with a charging current of 7.2 μA while the electronic watch is powered simultaneously (Figure 7c). The charging current drops to 0.61 μA when the TENG works in atmosphere (Figure 7d). When a commercial humidity-temperature meter with higher power consumption is used as the load, only working in high vacuum allows the TENG to power the device and charge the supercapacitor simultaneously and sustainably (Figure 7e). The meter continues to draw power from the supercapacitor when the TENG operates in air, as indicated by the monotone decrease of supercapacitor voltage in Figure 7f. Furthermore, a light-emitting diode (LED) light bulbs array (4 groups in parallel × 8 bulbs in series, rated power 0.75 W × 32) can be lit by the TENG working in high vacuum (Figure 7g), while the one in atmosphere can only support two bulbs at the same illuminance. This brief but straight-forward comparison demo shows the output power of this TENG is enhanced in 16-fold in high vacuum.

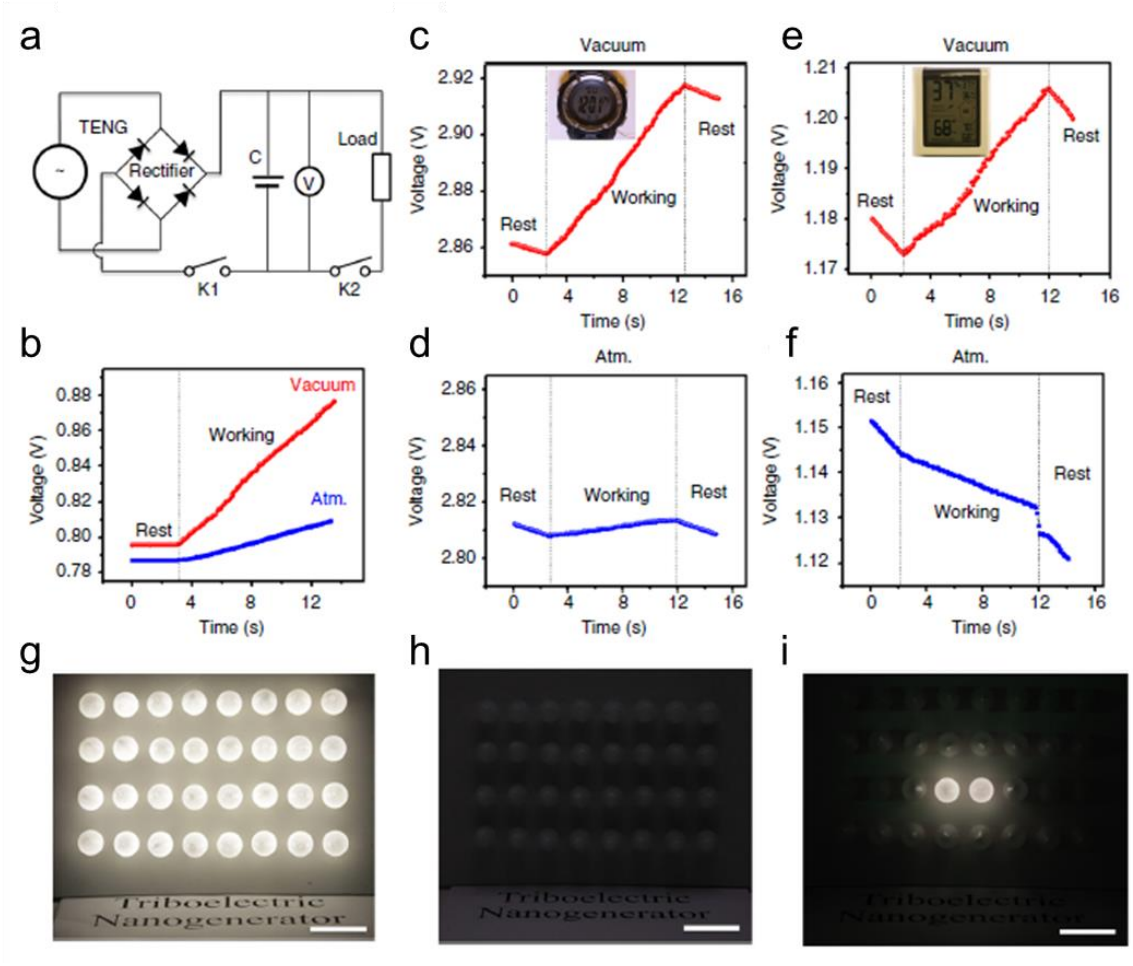


**Figure 7. Application of TENG in vacuum to drive electronics devices.** (a) Circuit diagram of the self-powered system consisting of the TENG and a supercapacitor. (b) Charging curves of the supercapacitor by pressing the TENG inatmosphere and high vacuum ($P \sim 10^{-6}$ torr). (c,d) Charging curves of the supercapacitor in high vacuum (c) and in atmosphere (d) when an electronic watch is driven by the TENG simultaneously. (e) Charging curve of the supercapacitor when a temperature-humidity meter is driven by the TENG in high vacuum simultaneously. (f) Discharging curve of the supercapacitor when the TENG in atmosphere is unable to drive the temperature-humidity meter alone. (g) Thirty-two LED light bulbs (each with rated power of 0.75 W) are lit in complete darkness by the TENG in high vacuum. (h) Thirty-two LED light bulbs cannot be lit by the TENG in atmosphere. (i) two LED light bulbs are lit in complete darkness by the TENG in high vacuum. Scale bar: 4 cm. Reproduced with permission.[71] Copyright 2017, Springer Nature.

### *2.1.5 Significance of Record-High Triboelectric Charge Density*

In this work, the triboelectric charge density of TENG is first improved to 660 μC/m$^2$ in vacuum where the limitation of air breakdown is broken through, and further to 1003 μC/m$^2$ via coupling of surface and dielectric polarization. High vacuum environments can not only guarantee better performance of TENG, but also spare TENG from performance degradation caused by the natural accumulation of dust and air moisture. The progress here sets new performance records of TENG and establishes a new optimization methodology for them. This work also provides an insight into the restricting factors on performance of TENG, making it necessary to re-estimate the upper limit of TENG to be much higher than previously expected.

The surface charge density of TENG is simultaneously limited by the triboelectrification charge density, air breakdown and dielectric breakdown, described formally as follows:

$$\sigma_{TENG} = \min\left(\sigma_{triboelectrification}, \sigma_{air\_breakdown}, \sigma_{dielectric\_breakdown}\right) \tag{7}$$

Without the concern of air breakdown, dielectric breakdown may become the next bottleneck of TENG. Concerning PTFE film, its $\sigma_{\text{dielectric\_breakdown}}$ can be calculated to be around 1115 μC/m$^2$, which is not far from our result of 1003 μC/m$^2$. Future work will involve the optimization of dielectric material to further explore the limitations of triboelectrification.

Without loss of generality, the new paradigm to enhance the triboelectric charge density of TENG in this work can be applied to other technologies involving contact electrification. Furthermore, it will benefit the long-lasting debate over the underlying

mechanism of triboelectrification and its kinetics, which calls for more experimental evidence to testify existing hypotheses, such as electron transferring by tunneling effect, mass transport, and even a hybrid of both.[73] In high vacuum, interfering factors to the triboelectrification such as dust and moisture can be reduced or even eliminated, and a much higher amount of transferred charge can be detected, both of which will favor the evidence seeking process.

In practice, our study points out an effective approach for hugely enhancing the output power of TENG, which greatly improves the prospect of large-scale blue energy using nanogenerators networks.[60] Considering that existing TENGs proposed for harvesting water wave energy are already enclosed and sealed with waterproof containers,[74, 75] it is rather straightforward and cost-effective to make them airtight and keep the inside in vacuum. The resulted boost in electrical output can reduce the size of blue-energy nets, and thus minimize the environmental impacts while meeting the energy needs especially in extreme weather conditions.

### *2.1.6 Experimental Methods*

#### 2.1.6.1 Fabrication of the TENG

For the conventional TENG with hard contact taken as the reference, a Cu film (Cu-I) was adhered to an acrylic substrate and acted as an electrode and a triboelectric material simultaneously, while the other triboelectric material, a PTFE film, was adhered to another Cu film (Cu-II) and then onto an acrylic substrate. Its Cu-I, Cu-II and PTFE film were of the same size, $3 \times 3$ cm$^2$. For the TENG with a cushioned Cu electrode and the fragmental structure, a piece of foam was placed between Cu-I and its corresponding acrylic substrate,

and PTFE and Cu-II were changed to a smaller size with a circular diameter of 1 cm. For the TENG with ferroelectric material, a piece of BT ceramic was placed between the PTFE film and Cu-II, with all others parameters kept the same. The thickness of the PTFE film was 200 μm. The TENG used for application demonstration in Figure 7 had a cushioned Cu electrode and did not involve ferroelectric material. Its Cu-I, Cu-II and PTFE film all had the same size of $5 \times 5$ cm$^2$.

#### 2.1.6.2 Preparation of Doped BT Ceramics

Samples of doped BT ceramics were synthesized by the conventional solid-state reaction process. The raw materials, BT without ZnO, were ball-milled in ethanol for 4 h. The dried mixtures were calcined at 1300 °C for 2 h, and then mixed by milling with ZnO powder for other 4 h. Mixed powder was pressed into discs with a diameter of 10 mm and consolidated by isostatic pressing at 200 MPa after adding polyvinyl alcohol, as a binder for granulation. Green compacts were sintered at 1450 °C for 4 h after burning out the binder at 650 °C for 30 min. All samples fabricated had a circular diameter of 1 cm and a thickness of around 0.6 mm.

#### 2.1.6.3 COMSOL Simulation

The 2D potential distribution between two oppositely charged surfaces of TENG, as plotted in Figure 4b, was numerically calculated using the commercial software COMSOL. The width of the device was set to be 1 cm and the thickness of both Cu and PTFE film was 200 μm. The gap distance between the Cu and PTFE film was 1 cm, and the surface charge density was 50 μC m$^{-2}$ for Figure 4b.

#### 2.1.6.4 Characterization

The vacuum environment for the TENG testing was obtained using an e-beam evaporator (Key). The contact-separation process of the TENG device was driven by the movement of a target shutter inside the vacuum chamber of the evaporator, and the external force was applied to an external knob which was connected to the target shutter. A programmable electrometer (Keithley model 6514) was adopted to test the open-circuit voltage, short-circuit current, and transferred charge density. A potentiostat (Princiton Application Research) was utilized to test the capacitance of the capacitor and the charging/discharging curves of the self-charging power system.

## 2.2 Spring-Based Resonance Coupling for Enhancing TENG Performance in Harvesting Low-Frequency Vibration Energy

Conventionally, the ambient mechanical energy is converted into electricity using EMG. The fundamental operating principle of EMG is Faraday's law of induction, and the technology maturity has enabled its wide application in both small-scale devices like RF powered tags and large-scale facilities like wind turbines and water dams. [76-78] However, its nature of linear relationship between output voltage/current and operating frequency greatly limits its effectiveness at low frequency (<5 Hz).[61] The effective output power obtained at low frequency could barely drive any electronics that has a threshold operation voltage.[79-81] In contrast, the output voltage of TENG is independent of frequency and remains in the range of 10-100 V depending on materials and structure design, resulting in a much slower declining rate of power after power management.[82-84] Considering that most ambient mechanical energy is at low frequency, therefore, TENG has a great potential in

outperforming EMG when it comes to scavenging energy from irregular human motions for powering small electronics or infrequent ocean waves for large-scale blue energy.

However, the current design of TENG is most effective for harvesting the instantaneous mechanical impact energy at the moment when the mechanical stimulation occurs, while a large portion of impact potential energy is dissipated due to the low triggering frequency. One approach is to use a spring structure to store the mechanical kinetic energy and potential energy and convert a low frequency triggering to a higher frequency oscillation, resulting in high average output power. In this work, a mechanical spring-based amplifier with the ability of amplifying both the vibration frequency and amplitude is integrated with TENG to improve its low-frequency performance. The features of amplified frequency and displacement enable the device to have a higher output power at low frequency and the performance boost can be up to 10 times in comparison to the conventional reference TENG that does not have the amplifier. The mechanical amplifier-assisted TENG (MA-TENG) also has a lower minimum working frequency (2.5 Hz) compared to its counterpart. This work introduces a fundamental concept of mechanical amplifier to the emerging field of TENG for largely enhancing its performance in harvesting low-frequency vibration energy, and thus is of great importance for future progress towards the highly anticipated prospect of large-scale blue energy. The proposed methodology of using average output power for quantitative comparison of MA-TENG and conventional reference TENG is capable of capturing the performance difference triggered by mechanical amplification (e.g. frequency upscaling), which is impossible for previously used instantaneous power that does not take into account the temporal variation

in electrical output. Therefore, the method serves as a great scheme for evaluating and standardizing TENG's performance in practical working environment.

### *2.2.1 Device Structures and Mechanism of Spring-Based Resonance Coupling*

Most conventional TENGs for harvesting vibration energy can be simplified as a single-spring resonator (referred to as SR-TENG below), and work on either contact-separation mode or single-electrode mode. In this work the single-electrode mode was chosen as the study subject but the concept applies to the contact-separation mode as well. A typical single-electrode SR-TENG consists of a single mass (denoted by $m_0$, 60.87 g) and a spring for resonant vibration, with one Cu film attached on the top base of the device and a PTFE film attached on the vibrating mass $m_0$, as illustrated in the left-hand schematic of Figure 8a. The PTFE film serves as one triboelectric layer while the Cu film functions as the other triboelectric layer as well as an electrode connected to external loads. Figure 8b and Figure 8c present the working mechanism of the single-electrode TENG under short-circuit condition and numerically calculated potential distribution of three typical states under open-circuit condition respectively. At the initial state i, the Cu electrode and PTFE film are in contact and there is no current flow or potential difference. Due to different surface electron affinities, however, the electrons will be transferred from the Cu electrode surface to the PTFE surface, leaving net positive charges on the electrode surface and net negative charges on the PTFE surface. When the electrode and PTFE film separates (state ii), the resulted charge separation will induce positive potential on the electrode relative to the ground under open-circuit condition, while under short-circuit condition, electrons will be driven from the ground to the electrode. At the maximum separation distance (state iii), the open-circuit potential on the electrode will reach its maximum value.

When the distance decreases as the PTFE film moves towards the electrode (state iv), the positive open-circuit potential on the electrode will decrease while electrons will flow from the electrode to the ground under short-circuit condition.

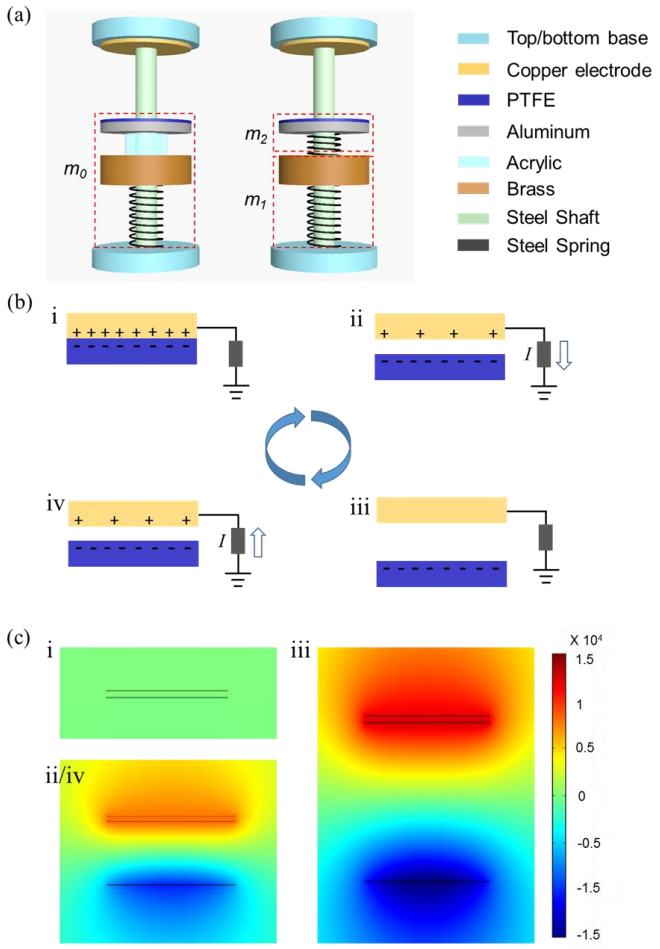


**Figure 8. Device structures for the study of spring-based resonance coupling and working mechanism.** (a) Device schematic of SR-TENG (left) and MA-TENG (right) consisting of two springs. (b) Working mechanism of the MA-TENG under short-circuit condition. (c) Numerical calculations of the potential on TENG electrodes at three typical states, as evaluated by COMSOL. Reproduced with permission.[85] Copyright 2017, Elsevier.

Under vertical vibration, the relative distance change between the electrode and the PTFE film is realized by the movement of $m_0$, whose upward velocity is obtained by

impacting with the bottom base, as illustrated in Figure 9a. In the simplest case that $m_0$ undergoes free fall before impact and the bottom base behaves like the ground, the conservation of momentum requires that velocity of $m_0$ after impact is equal to

$$v_0^{'} = e_{0,g} v_0 \tag{8}$$

where $v_0$ is the free-fall velocity and $e_{0,g}$ is the coefficient of restitution between $m_0$ and the bottom base. In perfect elastic collision, the coefficient of restitution will be 1 and $m_0$ only changes moving direction without velocity loss.

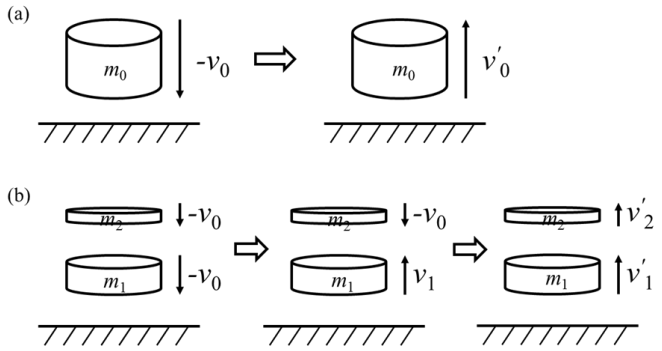


**Figure 9. Schematics of sequential collisions in TENG.** (a) SR-TENG and (b) MA-TENG. Reproduced with permission.[85] Copyright 2017, Elsevier.

A mechanical amplifier, as the name suggests, is a mechanical system used to amplify the magnitude of mechanical quantities such as velocity, frequency, displacement, *etc*.[86-88] Its origin can be dated back to the ancient times when levels and gear trains were invented, and it is ubiquitous in our everyday life, with applications ranging from small devices like diaphragms operating at resonating frequency to large systems like automotive drivetrains. With regards to mechanical energy harvesting, various types of frequency upscalers have been adopted and demonstrated to improve the performance of EMG or

piezoelectric generators operating at a frequency lower than their resonating frequency[87-89]. Inspired by the frequency-upscaling EMG and the TENG, an MA-TENG was proposed and fabricated to harvest the low-frequency vibration energy more effectively. In MA-TENG, the single mass $m_0$ in SR-TENG is split into two masses, $m_1$ (55.91 g) and $m_2$ (4.28 g) and an additional spring is introduced to achieve resonance coupling, as illustrated in the right-hand schematic of Figure 8a. Under vertical vibration, as illustrated in Figure 9b, $m_1$ will gain an upward velocity $e_{1,g}v_0$ after impacting with the bottom base, followed by the collision between $m_1$ and $m_2$. The sequential pairwise collision between the bottom base, $m_1$, and $m_2$, is capable of transferring kinetic energy from $m_1$ to $m_2$ and amplifying the velocity of final mass $m_2$ when $m_1 >> m_2$. This process is also called velocity amplification and can be described by a set of equations using rigid body mechanics.[90, 91] As in SR-TENG, the collision between the bottom base and $m_1$ can be described by

$$v_1 = e_{1,g} v_0 \tag{9}$$

As for the collision between $m_1$ and $m_2$, the first equation is given by the conservation of momentum,

$$m_1 v_1 + m_2 v_2 = m_1 v_1^{'} + m_2 v_2^{'} \tag{10}$$

where $v_i$ and $v_i^{'}$ are the velocity of $m_i$ before and after collision respectively. The kinetic energy loss during collision is accounted for by the coefficient of restitution $e_{2,0}$,

$$e_{2,1} = \frac{v_2^{'} - v_1^{'}}{v_1 - v_2} \tag{11}$$

By combining Equation 10 and 11, the velocity of $m_2$ after impact is solved as

$$v_2^{'} = \frac{m_1 v_1 \left(1 + e_{2,1}\right) + \left(m_2 - m_1 e_{2,1}\right) v_2}{m_1 + m_2} \tag{12}$$

By substituting Equation 9 and $v_2 = -v_0$ into Equation 12 and reorganizing,

$$v_2^{'} = \left[ \frac{\left(1 + e_{1,g}\right)\left(1 + e_{2,1}\right)}{1 + m_2 / m_1} - 1 \right] v_0 \tag{13}$$

Therefore, the final velocity gain of $m_2$ with respect to the $m_0$ after impact is

$$G = \frac{v_2^{'}}{v_0^{'}} = \frac{1}{e_{0,g}} \left[ \frac{\left(1 + e_{1,g}\right)\left(1 + e_{2,1}\right)}{1 + m_2 / m_1} - 1 \right] \tag{14}$$

In perfect elastic collision, the coefficients of restitution will be 1 and velocity gain is 2.72. The higher velocity of $m_2$ enables it to travel quicker and higher through the shaft than $m_0$, and thus the PTFE film in MA-TENG could be in contact with the top electrode more easily and more frequently as compared to the one in SR-TENG, even when the latter could not reach the top under the same ambient vibration. In other words, the mechanical amplifier is able to act as a frequency amplifier and a displacement amplifier simultaneously in MA-TENG. However, it is important to note that Equation 13 and 14 are derived under the strict constraints of sequential pairwise collisions and rigid-body

mechanics. In real devices under forced excitation, e.g. external vibration, the collisions take place over a finite time interval especially when springs are involved, and the sequence of impacts may vary. The velocity gain from a collision may even be smaller than 1 due to the change of impact sequence. For example, if $m_2$ collides with $m_1$ before the latter hits the base and reverses its downward moving direction, the velocity of $m_2$ will decrease instead of being amplified. Also, the bottom base, which is also under vibration, acts as an "active ground" rather than a "still ground", and its impact with the $m_0$ or $m_1$ may increase or reduce their falling velocity when $e_{i,g} > 1$ or $e_{i,g} < 1$ respectively. With all the above being accounted for, at certain frequencies, the event that the velocity gain of the masses from collision is smaller than 1 has higher chance of occurrence, and thus the electrical output may reach a local minimum.

### *2.2.2 Qualitative Comparison of Electrical Outputs of SR-TENG and MA-TENG*

The performance of SR-TENG and MA-TENG was studied under ambient vibration ranging from 2.5 Hz to 6.0 Hz. Figure 10a and Figure 10b plots their typical short-circuit current at 3.5 Hz, 4.5 Hz and 6.0 Hz frequency respectively, and the outputs at other frequencies are presented in Figure 11. The results provide a clear qualitative comparison of the electrical outputs of the two devices. At the same ambient vibration frequency, more current peaks were generated from the MA-TENG, whereas the current peaks correspond to the contact between the PTFE film and the top electrode when the $m_0$ or $m_2$ collides with the top base. Figure 10c and Figure 10d plots the typical short-circuit current outputs under ambient vibration of 6.0 Hz over a short time domain of 1 second. It can be observed that the number of peaks from SR-TENG, 6, was exactly the same as the frequency while the number of clearly distinguishable peaks from MA-TENG was at least

10, nearly double of the frequency. Therefore, the output frequency of MA-TENG has been experimentally validated to be higher than that of SR-TENG when they are under the same ambient vibration frequency, which confirms the presence of frequency amplification in MA-TENG. As elaborated above, this amplified output frequency can be attributed to the amplified velocity of $m_2$ obtained from the collision with $m_1$ since the frequency of contact increases when the PTFE film moves faster towards the top electrode. Also, the minimal vibration frequency required for achieving contact between the PTFE film and top electrode in MA-TENG (2.5 Hz) is lower than that of SR-TENG (3.5 Hz), which is owing to that the amplified velocity helps the PTFE film reach the top more easily and thus proves the existence of displacement amplification. Another point worth noting is that the average value of short-circuit current peaks of both TENGs increases as the vibration frequency increases from 2.5 Hz to 6.0 Hz. This can be well explained by the equation

$$I = \frac{dQ}{dt} \tag{15}$$

where $I$ is electrical current, $Q$ is transferred charge and $t$ is time. Firstly, when the frequency is higher, the PTFE film on $m_0$ or $m_2$ can gain a higher upward velocity, making the time $dt$ shorter; Secondly, when the velocity of $m_0$ or $m_2$ is higher, based on the Impulse-Momentum Theorem,

$$Fdt = mdv \tag{16}$$

the impact force between the PTFE film and the top electrode will be larger, resulting in more intimate contact. The more intimate contact can enhance the generation of

triboelectric charges and thus brings about higher *dQ*. With shorter *dt* and higher *dQ*, the current would be higher as the ambient frequency increases.

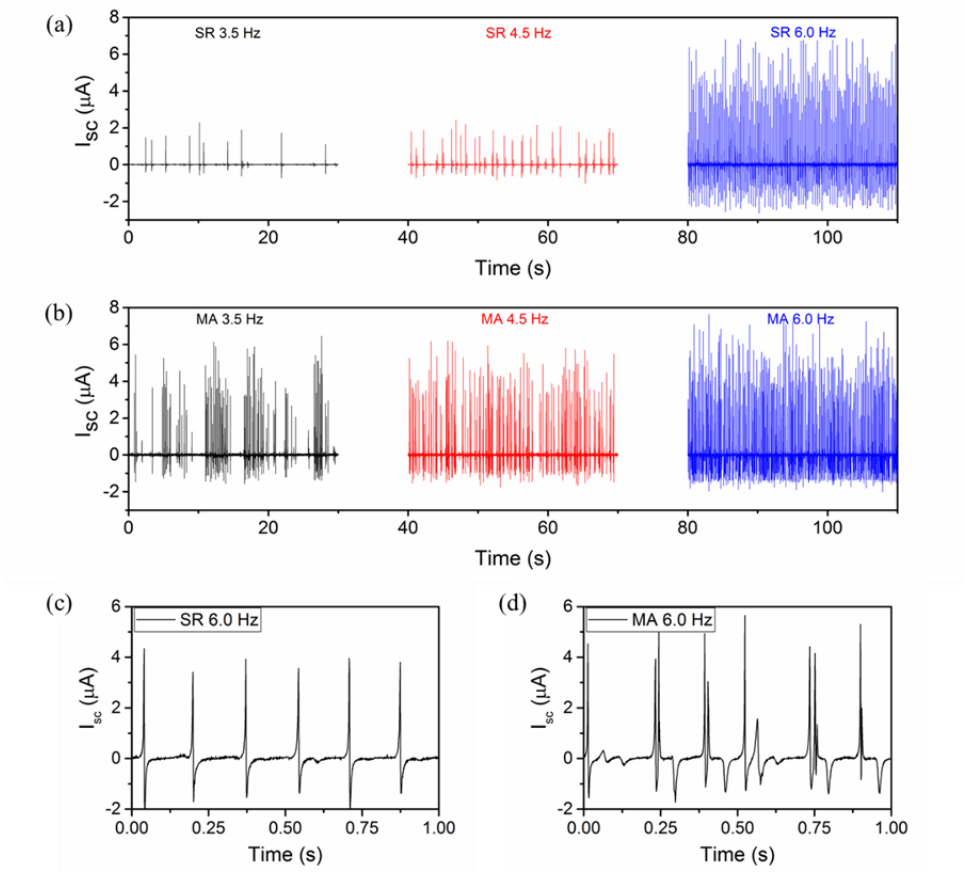


**Figure 10. Qualitative comparison of electrical outputs of SR-TENG and MA-TENG.** Typical short-circuit current of (a) MA-TENG and (b) SR-TENG operating at 3.5, 4.5 and 6.0 Hz vibration frequency over a 30-second time domain. (c) & (d) Zoom-in comparison of short-circuit current by the two configurations at 6.0 Hz in a short 1-second time domain. Reproduced with permission.[85] Copyright 2017, Elsevier.

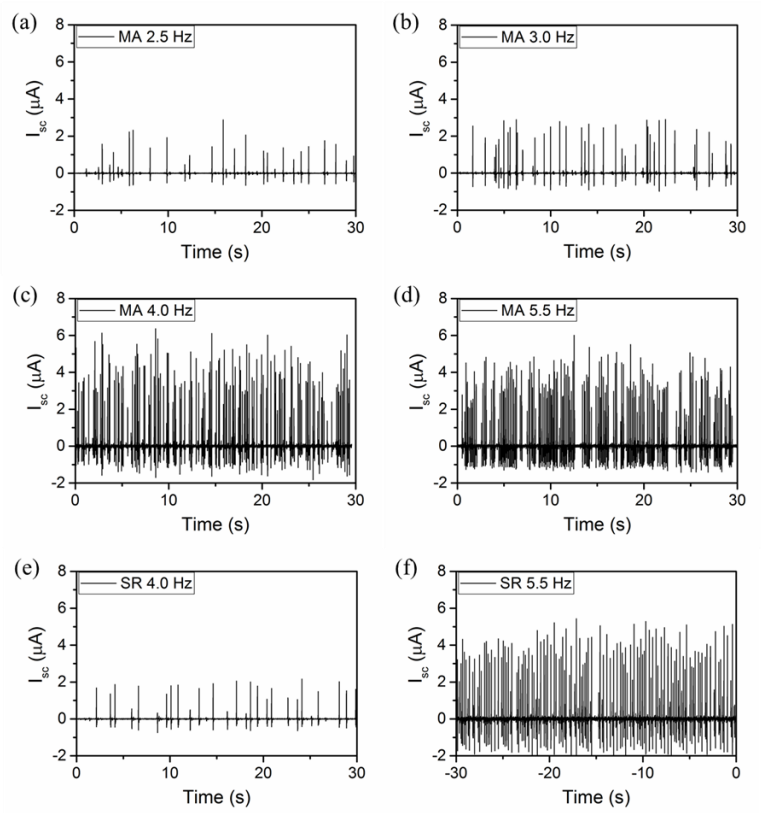


**Figure 11. Typical short-circuit current of MA-TENG and SR-TENG.** MA-TENG operating at (a) 2.5 Hz, (b) 3.0 Hz, (c) 4.0 Hz and (d) 5.5 Hz, and SR-TENG at (e) 4.0 Hz and (f) 5.5 Hz. Reproduced with permission.[85] Copyright 2017, Elsevier.

### *2.2.3 Quantitative Comparison of Electrical Outputs of SR-TENG and MA-TENG*

Although the short-circuit current has provided a strong, qualitative comparison of the two TENGs, power remains one of the most intuitive and effective measures to quantitatively evaluate the performance of electricity generation devices. Most previous work about TENG[92-95] used the concept of maximum instantaneous power to represent the strength of their output, however, instantaneous power is prone to overestimate the performance without the consideration of temporal variation. Meanwhile, the average power, albeit requiring more computational efforts to calculate, provides a more accurate

account of the actual work that can be achieved from a generator in a practical time interval. It is given by

$$P_{ave} = \int VIdt \Big/ \Delta t \tag{17}$$

where $V$ is the voltage across the applied load, $I$ is the current flowing through it, and $\Delta t$ is the length of selected time interval. Recently Zi *et al.* proposed a set of figure of merits for standardizing TENG[72] as well as a rationally designed charging cycle using TENG,[96] both of which emphasized the significance of voltage $V$ and transferred charge $Q$, or the voltage-charge transfer ($V$-$Q$) plot, on the evaluation and maximization of TENG performance. Therefore, it makes sense to expressing the power equation using $V$ and $Q$ by substituting $Idt$ with $dQ$,

$$P_{ave} = \int VdQ \Big/ \Delta t \tag{18}$$

According to both Equation 17 and 18, the length of time interval $\Delta t$ is a very critical parameter that would greatly affect the validity of calculated average power as well as the amount of required computational efforts. If $\Delta t$ is too short, the interval would not be adequate to give a reliable estimate of the long-term performance of the TENG; if it is too long, the process of experimental measurement and data analysis would be inefficient. The most straightforward choice of $\Delta t$ is the period of the electrical output. However, as seen in Figure 10, the outputs of both SR-TENG and MA-TENG under ambient vibration are not periodic from cycle to cycle. Figure 12a and Figure 12b plot typical $V$-$Q$ characteristics of SR-TENG under 3.5 Hz vibration and MA-TENG under 2.5 Hz vibration

when connected to a 20 MΩ external resistor over a 5-seconds interval respectively. The results clearly show that the work done per cycle (the area of a cycle in the plots) varies greatly and it would be insufficient to randomly chose a cycle length for $\Delta t$. The validity of the measured $V$-$Q$ plot is proven by Figure 12c, which presents the short-circuit and open-circuit $V$-$Q$ plots of the MA-TENG under 2.5 Hz vibration. In open-circuit condition, the transferred charge would be zero and the plot is nearly a vertical line at $Q$=0; while in short-circuit condition, the output voltage would be zero and the plot is nearly a horizontal line at $V$=0. To determine the proper length of time interval for calculating the average power, a convergence study by averaging the electrical work done over different time intervals was proposed and conducted, with results shown in Figure 12d. For both SR-TENG under 3.5 Hz vibration and MA-TENG under 2.5 Hz vibration, the average output power with an external load of 20 MΩ reaches a steady state when the interval approaches 30 seconds. Considering that 3.5 Hz and 2.5 Hz are the lowest ambient vibration frequencies to generate notable electricity from SR-TENG and MA-TENG respectively, it is adequate to choose the 30-seconds length for $\Delta t$ in calculating the average power when the TENGs are connected to various external loads under different vibration frequencies.

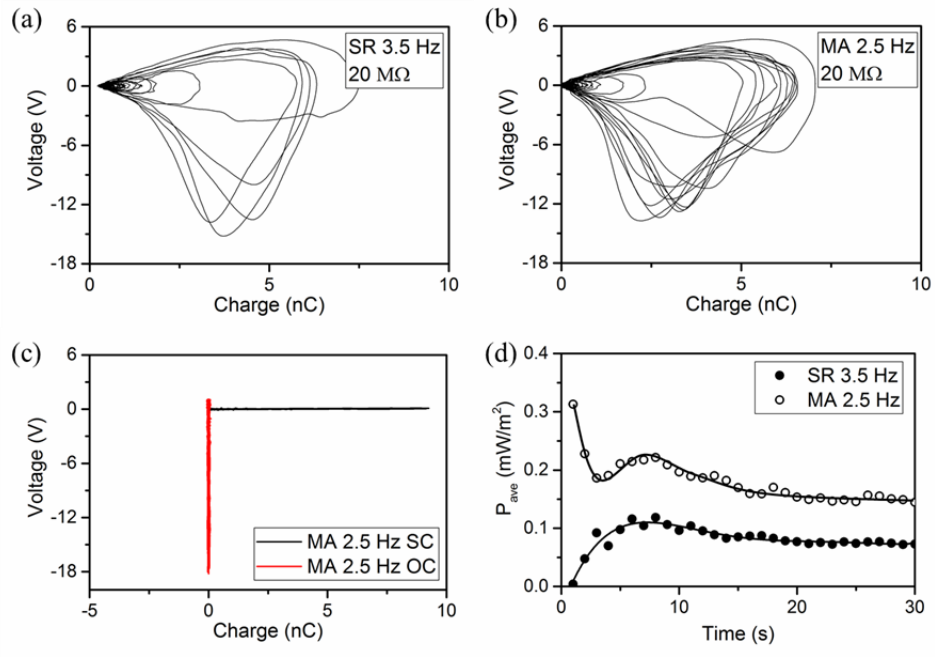


**Figure 12. Quantitative comparison of electrical outputs of SR-TENG and MA-TENG.** Typical *V*-*Q* characteristics of (a) SR-TENG at 3.5 Hz vibration, (b) MA-TENG at 2.5 Hz vibration for 5 s when connected to the matched load resistance of 20 MΩ. (c) The short-circuit and open-circuit *V*-*Q* plots of the MA-TENG at 2.5 Hz vibration. (d) Convergence study of the average output power over different length of time intervals for SR-TENG at 3.5 Hz vibration and MA-TENG at 2.5 Hz vibration. Reproduced with permission.[85] Copyright 2017, Elsevier.

The average output power of SR-TENG and MA-TENG under ambient vibration of different frequencies is presented in Figure 13. Both TENGs exhibit maximum average output power when the external load resistance is around 20 MΩ, which is independent of the ambient vibration frequency. The strong comparison of the plots in Figure 13a and Figure 13b shows that MA-TENG starts to function as an electricity generator at a lower frequency and its output is much higher than the conventional SR-TENG at the same low frequency. Meanwhile, when the frequency is higher than 5.0 Hz, the maximum output power of both TENGs, as shown in Figure 13c and Figure 13d, is about the same. It can be explained by the fact observed during experiments that the mass $m_0$ in SR-TENG and $m_1$

in MA-TENG could easily reach the top base at the same frequency as the ambient one even without velocity amplification when the vibration frequency was above 5.0 Hz. In such a case, although the collision between $m_1$ and $m_2$ brings a larger count of contact between the triboelectric layers as shown in Figure 10, the major output contribution is attributed to the more intimate contact induced when the big masses $m_0$ and $m_1$ hit the top, as evidenced by the abrupt increase of output of both TENGs when the frequency changes from under 5.0 Hz to above 5.0 Hz. The maximum output power of both TENGs under different ambient vibration frequencies is summarized in Figure 13e, which clearly shows the enhanced performance of MA-TENG at low vibration frequency, with a maximum power ratio of 10:1 at 4.0 Hz. One point worth mentioning is that the structure of the TENGs, such as mass weight, springs, device height and *etc*., were not optimized in this work, and thus it is the relative comparison of their output power, rather than the absolute values, that is the focus of discussion. To further validate the results, the TENGs were used to charge a 0.33 mF capacitor at different vibration frequencies and the voltage increase of the capacitor after 30 s charging is plotted in Figure 13f. The comparison trend is highly consistent with that in Figure 13e, demonstrating the performance enhancement of MA-TENG in practical application. Considering that no other changes necessary in the device structure or operating mode, therefore, introducing a mechanical amplifier into TENG by splitting one single mass into two masses of large weight ratio is a simple but effective way to enhance its electrical output especially at low vibration frequencies.

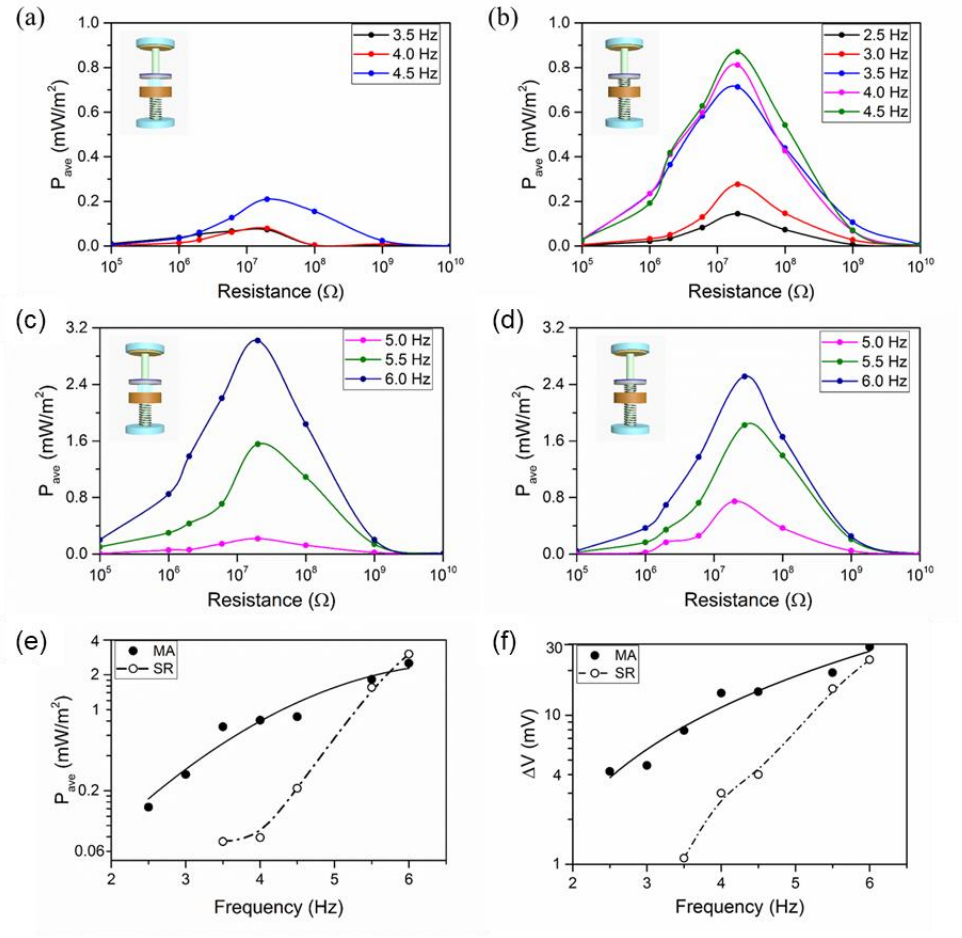


**Figure 13. Comparison of average output power of SR-TENG and MA-TENG.** Average output power of (a,c) SR-TENG and (b,d) MA-TENG with different load resistance operating at different vibration frequency. (c) Comparison of maximum output power of MA-TENG and SR-TENG at different frequencies. (d) Voltage increase of a 0.33 mF capacitor after being charged for 30 s by MA-TENG and SR-TENG operating at different frequencies. Reproduced with permission.[85] Copyright 2017, Elsevier.

In summary, a MA-TENG with amplified frequency and displacement is designed based on velocity amplification using coupled-springs in order to improve its output performance under low-frequency vibration. To quantitatively compare their performance, a new scheme of comparing different TENGs using average output power is proposed and the process of choosing the appropriate time interval for analysis is demonstrated. The scheme takes into account the temporal variation in electrical output and offers a more

accurate and convincing evaluation of TENG performance compared to previously used instantaneous power, especially in the case with infrequent or irregular mechanical input. It can serve as a standard for evaluating and comparing TENGs with different structures and operating modes in practical working environment, where the vibration is not periodic as in laboratory simulation. The corresponding analysis based on experimental results demonstrates a performance boost of the MA-TENG up to 10 times, which is further validated by the capacitor charging rate. This work serves as an important progress for the future development and application of TENG, especially for harvesting low-frequency vibration energy as well as the great prospect of blue energy.

### *2.2.4 Experimental Methods*

#### 2.2.4.1 Fabrication of SR-TENG and MA-TENG

The bases, the shaft and three masses ($m_0$, $m_1$ and $m_2$) in SR-TENG and MA-TENG were designed using SolidWorks. The detailed dimensions of $m_1$ and $m_2$ are shown in Figure 14. $m_1$ (55.91 g) is made of brass, with a diameter of 1 inch and a height of 0.5 inch; $m_2$ (4.28 g) is made of aluminum (Al), with a diameter of 1 inch and a height of 0.1 inch. $m_0$ (60.87 g) is made by binding together $m_1$ and $m_2$ with a lightweight acrylic rim to achieve a similar total weight ($m_0 \sim m_1 + m_2$). The long spring attached to $m_0$ and $m_1$ has a length of 0.75 inch and a spring constant of 2.5 lbs./inch; the short spring on $m_2$ has a length of 0.25 inch and a spring constant of 13.5 lbs./inch. The steel shaft has a diameter of 1/8 inch and a length of 3 inch. The PTFE film was pasted onto $m_0$ or $m_2$ with foam tape and the Cu film was attached to the top base using insulating Kapton tape.

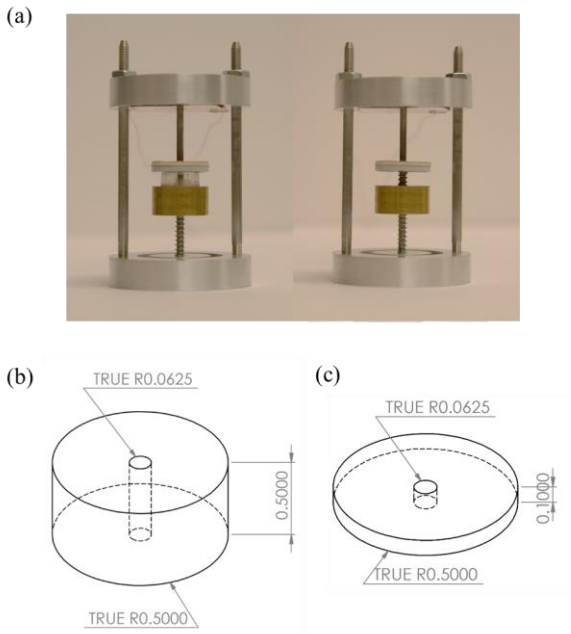


**Figure 14. Photograph and dimension of SR-TENG and MA-TENG.** (a) Photograph of fabricated devices. (b) Drawing of the brass disk $m_1$. (c) Drawing of the Al disk $m_2$. Reproduced with permission.[85] Copyright 2017, Elsevier.

2.2.4.2 Vibration Testing of TENGs

The vibration at different frequencies was stimulated using a shaker (ET-126B Electrodynamic Transducer, Labworks Inc.). The shaker was controlled using a sine servo controller (SC-121, Labworks Inc.) and a linear power amplifier (PA-151, Labworks Inc.). The short-circuit current of both TENGs was measured using a Keithley 6514 system electrometer, while the output voltage and transferred charge with different load resistance were measured by two electrometers simultaneously. The whole metal bases were grounded during measurement.

## 2.3 Stretchable Paper-Based TENG Made of Interlocking Kirigami Patterns

Over the last decade, flexible and stretchable electronics has emerged as the next-generation functional devices and has attracted extensive interests from both academia and industry. Compared to their rigid counterparts, flexible and stretchable electronics offers great deformability without sacrificing the device's performance and reliability and thus has promising applications in wearable devices, epidermal electronics, implantable devices, *etc*.[97-101] However, the stretchability of previously reported TENGs are highly dependent on their constituent materials, and materials with intrinsic elasticity like polydimethylsiloxane (PDMS) and rubber are necessary. This greatly weakens the material advantage of TENG over other energy generation technologies, and thus methods of introducing stretchability from designed structures rather than materials are meaningful. One promising approach is taking use of traditional origami or kirigami patterns, which have been proven to be successful in fabricating elastic nanocomposites,[102] solar trackers,[103] deformable lithium batteries,[104] reprogrammable mechanical metamaterials,[105] and optical devices.[106]

This work focuses on introducing a new type of highly stretchable TENG by using the traditional kirigami patterns, whose stretchability originates from the designed structures instead of constituent materials. The proposed method enables stretchable TENG to be made from materials without intrinsic stretchability, such as paper, fluorinated ethylene propylene (FEP), PTFE, PET and Kapton, and thus is very versatile. The fabricated devices sustained an ultrahigh tensile strain up to 100% and were capable of harvesting energy from various types of motions such as stretching, pressing and twisting. Simple hand clapping on the device could generate a maximum open-circuit voltage of 115.49 V and a maximum transferred charge quantity of 39.87 nC. Furthermore, the

KTENG has been demonstrated for a broad range of applications, such as powering a liquid crystal display (LCD) screen, lighting LED arrays, self-powered acceleration sensing and self-powered sensing of book opening and closing. This work presents an important progress of TENG for applications in stretchable and flexible electronics, and it will initiate new insights and directions on kirigami-based devices.

### *2.3.1 Device Structure and Working Mechanism of KTENG*

The schematic structure of the stretchable, paper-based TENG with interlocking kirigami patterns (KTENG) and related pictures are illustrated in Figure 15a. The KTENG consist of one Cu-coated paper sheet and one FEP thin film interlocked by rationally designed linear and rectangular kirigami patterns Figure 15b. The fabrication process started with laser-cutting a piece of printer paper with the linear kirigami pattern, which has been proven to be a simple but effective method of introducing super high stretchability into stiff sheets. The deformation mechanics and relationship between the unit cell parameters (denoted by horizontal spacing x, vertical spacing y and cut length l as illustrated in Figure 15b) and attainable strain have been well studied.[102] In this work, both the horizontal and vertical spacing between notches were set to be 2 mm, and the cut length was 22 mm. The resulted paper can withstand a tensile strain up to 200% without breaking. Then Cu thin film was sputter-coated onto both sides of the laser-cut paper to serve as one of the triboelectric materials and the electrode of the TENG. FEP thin film with 100 nm wide, 1 μm long nanowires (NWs) to enhance the surface charge quantity[55, 92, 107-109] was chosen as the other triboelectric material and laser-cut with the rectangular kirigami pattern, whose unit cell parameters were designed to match those of the linear kirigami on paper so that an interlocking structure could be formed. Two rectangles can fit into a single

notch of the linear kirigami as shown in Figure 15b. Finally the prepared FEP film and paper were assembled together to obtain the final device. The effective dimensions of the device were approximately 7.2 cm in length, 6 cm in width and 150 μm in thickness.

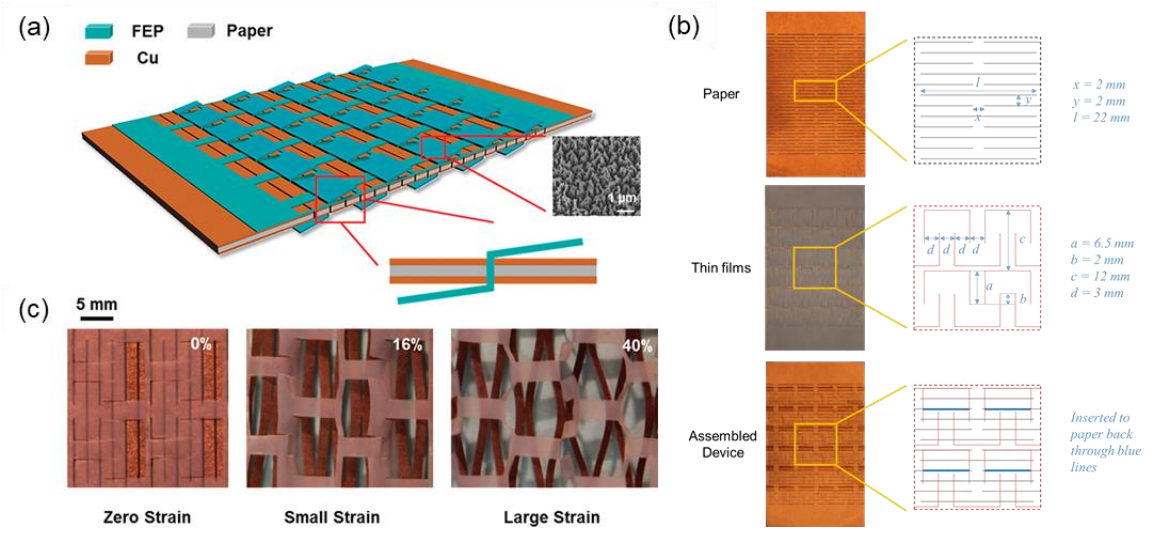


**Figure 15. Design and photographs of KTENG.** (a) Schematic structure of paper-based KTENG. Top insert: SEM image of the FEP film; bottom insert: cross-section view of the interlocking structure. (b) Design parameters of the kirigami patterns. (c) Photographs of the assembled device under different tensile strains. Reproduced with permission.[40] Copyright 2016, American Chemical Society.

The KTENG operates on the basis of the single-electrode mode[7, 27] and its working principles under stretching operations are illustrated in Figure 16. At the initial state, the Cu electrode and FEP film are in contact and there is no electrical output. Due to different surface electron affinities, however, the electrons will be transferred from the Cu electrode surface to the FEP surface, leaving net positive charges on the electrode surface and net negative charges on the FEP surface. When a tensile force is applied on the KTENG, the paper and FEP film undergo deformation of different amplitudes due to different kirigami patterns. The rectangular cuts of the FEP film will deflect more from the horizontal surface, and thus the distance between the Cu electrode and FEP will increase. As a result, the

charge separation will induce potential difference between the electrode and the ground in the open-circuit condition, and electrons will be driven from the ground to the electrode in the short-circuit condition. As the tensile strain increases and the angular deflection of the rectangular cuts of FEP film reaches approximately $90^{o}$, the largest distance between the triboelectric layers as well as the maximum open-circuit potential difference will be achieved, which is defined as the fully stretched state. As the tensile strain continues to increase, the KTENG will transit to over-stretched state. The distance between the triboelectric layers and the open-circuit potential difference will start to decrease, and the electrons will flow from the electrode to the ground in the short-circuit condition until the stretching stops. When the tensile force is released and the device recovers to its original state, the distance between the triboelectric layers will increase first until back to the fully stretched state and decrease afterwards until back to the initial state, so is the open-circuit potential difference between the electrode and the ground. In the short-circuit condition, the electrons will first flow from the ground to the electrode before reverting back to the fully stretched state and vice versa afterwards. Therefore, a cyclic AC output can be generated across the load between the electrode and the ground when a periodic tensile force is applied on the KTENG. In case the maximum strain is not large enough, the entire power generation cycle may be partially fulfilled, as illustrated by the dark blue and purple dash lines in Figure 16. The rationally designed interlocking kirigami structure poses restraints on the deformation of FEP film and ensures that the device can recover to its original state when the tensile force is released, which greatly enhances the robustness and reliability of the device. Furthermore, unlike conventional TENGs which require additional spacers for the charge separation process, the KTENG relies on the deformation of different

kirigami structures to induce charge separation. Therefore, the most important innovation of the KTENG is the structure with interlocking linear and rectangular kirigami patterns, which not only provides the stretchability and robustness of the device, but also helps to facilitate the charge separation process.

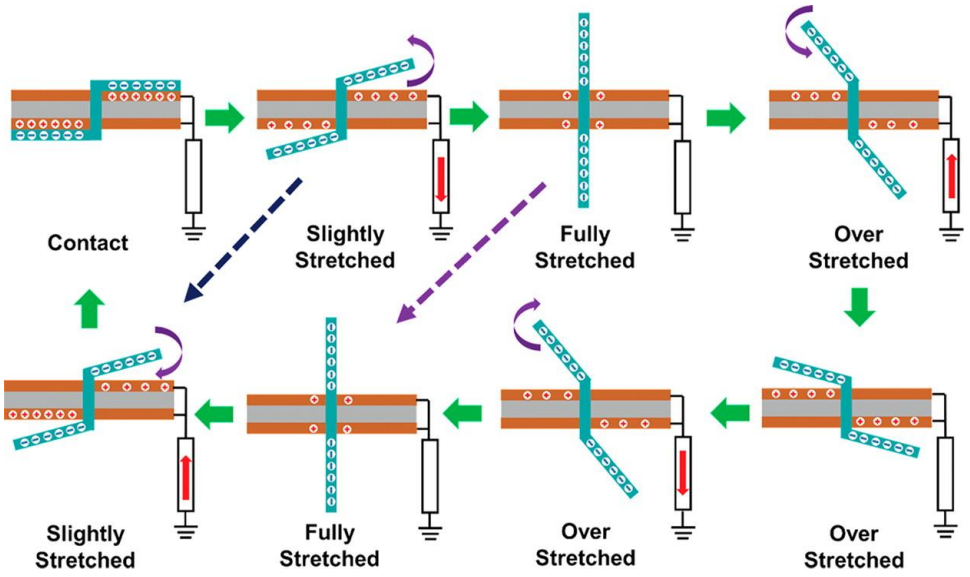


**Figure 16. Working mechanism of the KTENG.** Reproduced with permission.[40] Copyright 2016, American Chemical Society.

### *2.3.2 Performance of KTENG*

The typical electrical output of the KTENG under cyclic stretching up to specific tensile strains of 16%, 28% and 40% are plotted in Figure 17. Figure 17(a-c) presents the open-circuit voltage ($V_{oc}$), the short-circuit current ($I_{sc}$) and the transferred charge quantity ($Q_{tr}$) respectively. The top inserts show the cross-section photographs of the KTENG at these strains, indicating their differences in deflection magnitude. It can be observed that at the strain of 16%, 28% and 40%, the device reaches approximately the slightly stretched, fully stretched and over stretched state respectively. Therefore, the plotted results can be

regarded as the representative data of the output performance when the KTENG is stretched to these states. In the case that the device at the maximum applied strain is at the slightly or fully stretched state, the $V_{oc}$ and $Q_{tr}$ increase monotonically with the applied strain, while the $I_{sc}$ only changes sign at the maximum applied strain and the zero strain. In the case that the device at the maximum applied strain is at the over stretched state, the $V_{oc}$ and $Q_{tr}$ increase first with the applied strain until the strain of the fully stretched state is reached, after which both start to decrease until the maximum applied strain. In the process of recovering to the original zero-strain state, the $V_{oc}$ and $Q_{tr}$ increase again as the device approaches the fully stretched state and start to decrease thereafter. The behavior is clearly reflected by the concave top of the $V_{oc}$ and $Q_{tr}$ plots. Correspondingly, the $I_{sc}$ changes sign not only at the maximum applied strain and the zero strain but also at the strain of the fully stretched state, which results in the small humps at the middle of the $I_{sc}$ plot. The different behaviors of the electrical output when the KTENG is stretched to different states can be well explained by the working principles proposed in Figure 16. In the first two cases of slightly and fully stretched states, the charge separation distance increases monotonically with the applied strain, and thus the $V_{oc}$ and $Q_{tr}$ changes monotonically as well. In the case of over stretched state, the charge separation distance first increases with the applied strain but starts to decrease after the device reaches the fully stretched state, which results in a local maximum of the $V_{oc}$ at the strain of the fully stretched state and an additional position for the sign change of the $I_{sc}$ besides the maximum applied strain and the zero strain. Therefore, the $V_{oc}$ and $Q_{tr}$ will go through the trend of up-down-up-down in one stretch-release cycle as illustrated in Figure 17. It can also be observed that at the strain of the fully

stretched state, 28% for the fabricated device, the maximum values of obtained $V_{oc}$, $I_{sc}$ and $Q_{tr}$ are approximately 7.32 V, 2.64 nC and 10.58 nA.

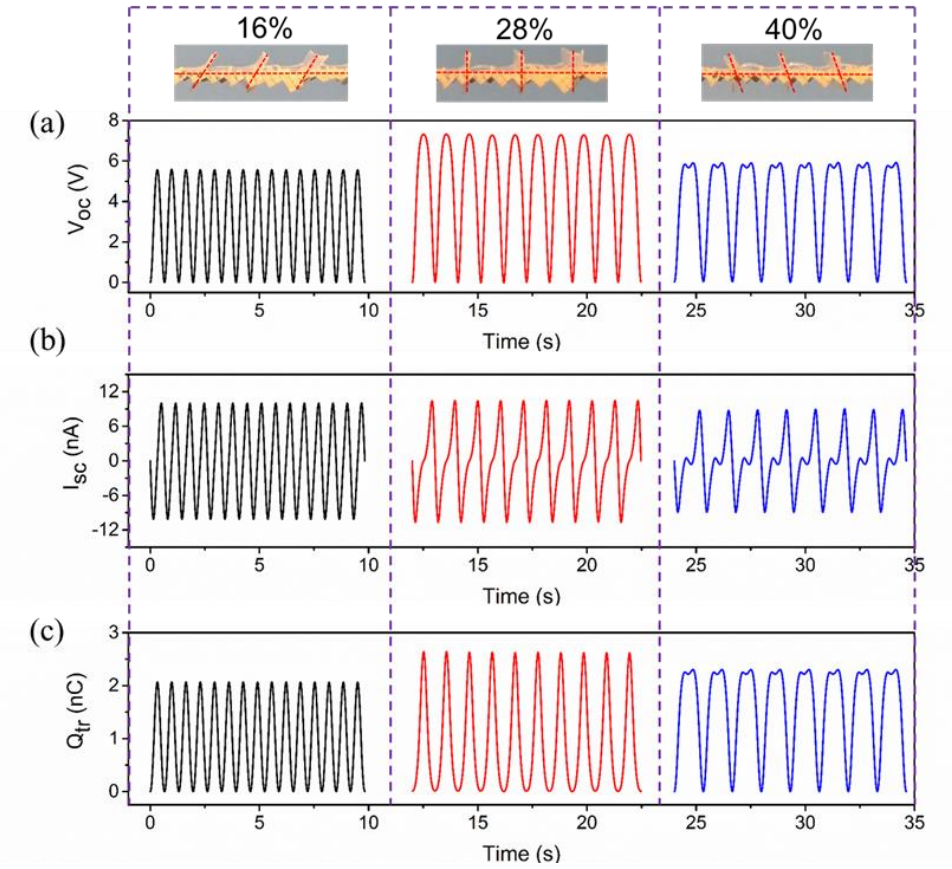


**Figure 17. Typical electrical outputs of the paper-based KTENG at specific stretched strains of 16%, 28% and 40%.** (a) The open-circuit voltage ($V_{oc}$), (b) the short-circuit current ($I_{sc}$), and (c) the transferred charge quantity ($Q_{tr}$). The top inserts are the cross-section images of the KTENG under these strains. Reproduced with permission.[40] Copyright 2016, American Chemical Society.

To further evaluate the output performance of the KTENG consisted of Cu-coated paper and FEP film, its $V_{oc}$ when stretched up to different strains is measured and plotted using black lines in Figure 18. The $V_{oc}$ reaches its maximum when the maximum strain applied is 28%, at which the device is approximately at the fully stretched state. To demonstrate the versatility of the proposed interlocking kirigami structure for fabricating

stretchable TENG, other materials commonly used as triboelectric layers such as PTFE, PET and Kapton were explored as well. Their thin films were laser cut with the same rectangular kirigami pattern as on the FEP film, and then assembled with the same Cu-coated paper with the linear kirigami pattern. All of these materials are considered as non-stretchable but the assembled KTENGs can be stretched at least up to a 60% strain. As expected, the material with the best ability to attract electrons, FEP, gives the highest $V_{oc}$, followed by PTFE and PET. The Kapton KTENG has the lowest output even though it is supposed to have higher ability to attract electrons than PET, according to the summarized triboelectric series. The contradictory experimental result over theoretical expectation can be explained by the high stiffness of Kapton, which makes the Kapton film not able to form intimate contact with the Cu-coated paper after interlocking assembly. Without intimate contact between the triboelectric layers, the transferred charge quantity will be limited, so is the generated $V_{oc}$. The maximum tensile strain the devices can withstand is highly dependent on the design parameters of the interlocking kirigami patterns, and their detailed relationship will be the subject of future work.

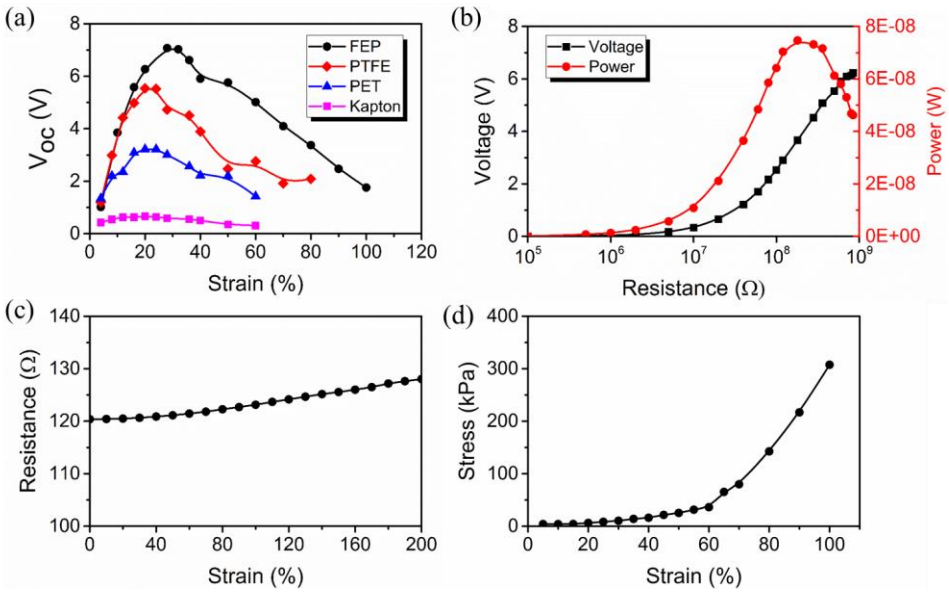


**Figure 18. Characteristics of the paper-based FEP KTENG *vs* stretched strain.** (a) The summarized relationship between the $V_{oc}$ and the stretched strain of different materials. (b) Relationship between instantaneous power density and the resistance of external load under 28% strain. (c) Relationship between the resistance of Cu-coated kirigami paper and stretched strain. (d) The stress-strain response of the paper-based KTENG. Reproduced with permission.[40] Copyright 2016, American Chemical Society.

To evaluate the effective output power of the FEP KTENG, the output voltage was recorded with various resistances applied as the external load. Then the effective output power of the KTENG was calculated as $P = V^2/R$, where $V$ is the output voltage across the applied load and $R$ is the applied load resistance, and the relationship between the output voltage/power and the resistance was plotted in Figure 18b. As expected, the output voltage of the KTENG was close to zero at the low-resistance region (when load resistance was smaller than 1 MΩ) but increased dramatically as the load resistance kept increasing. The output power initially increased with the load resistance but started to decrease after the resistance reached a certain value. Here the maximum output power of 74.66 nW was achieved at a load resistance of 180 MΩ.

One critical challenge of fabricating stretchable TENG is to make stretchable electrodes. To validate the functionality of the stretchable Cu-paper with the linear kirigami pattern, its resistance was recorded at different tensile strains. As seen from Figure 4c, the resistance of the Cu-paper only increased from 120.39 Ω to 128.03 Ω when the applied strain reached 200%, which is equivalent to a negligible change of 6.34%. This result proves that the linear kirigami pattern is capable of accommodating the applied strain with minimal sacrifice of the conductivity of the stretchable electrode. To characterize the mechanical property of the KTENG, the stresses required for stretching the device to certain strains was measured. It is clear that the KTENG has a two-stage strain-stress response and its tensile modulus of the KTENG experiences a dramatic change from 59.6 kPa to 668.4 kPa when the strain reaches 60%. This phenomenon can be explained by the difference between the structural deformation and material intrinsic deformation. In the first stage, the kirigami patterns render the device stretchable and thus the stress required for stretching is mainly attributed to deforming the interlocking kirigami structure; while in the second stage, the FEP film with the rectangular kirigami pattern has reached its limit of structural stretchability and the FEP material itself undergoes plastic deformation. This is further verified by the stretching limit of a 60% strain for the PET and Kapton KTENG, as shown in Figure 18a. These two materials are stiffer than FEP/PTFE and cannot withstand large tensile strains, which makes the devices consisted of them break once their structural stretching limit from the rectangular kirigami pattern is reached.

### *2.3.3 Application of KTENG*

As discussed earlier in the working principles of the KTENG under stretching, electrical energy is generated through the distance change between the two triboelectric

materials. Any mechanical stimulus that brings about relative motion between the FEP film and the Cu-paper can be converted into electricity. Therefore, the KTENG can be operated under three different modes (stretching, pressing and twisting), and is capable of harvesting energy from various mechanical stimuli, such as pulling, tapping, wind blowing, *etc*. Figure 19 presents the schematics of the KTENG under different operating modes and their typical electrical outputs. The electrical outputs for the stretching mode were recorded when the device was stretched cyclically up to 28%, which yielded a maximum $V_{oc}$ of 7.32 V and a maximum $Q_{tr}$ of 2.64 nC. The pressing mode was demonstrated by hand clapping onto the device, and a maximum $V_{oc}$ of 115.49 V and a maximum $Q_{tr}$ of 39.87 nC were achieved. The twisting mode was realized when the device was hold in hands on both ends and twisted repeatedly, with a maximum $V_{oc}$ of 6.55 V and a maximum $Q_{tr}$ of 4.76 nC generated. The stretching and twisting modes had similar maximum output values but the uniformity of their output profiles as a function of time varied. The stretching outputs were nearly identical for different cycles while the twisting outputs varied from a cycle to another. As observed from experiments, the KTENG could easily recover back to original interlocking state when the stretching was released while it was not the case for twisting. The integrity of the rationally designed interlocking structure was prone to damaging when the device was twisted and the FEP rectangles tended to pop out from the linear notches on the Cu-paper. The original interlocking state could not be recovered automatically when the twisting force was released, and the resulted interlocking structure was random and usually uneven without perfect position match of the kirigami patterns, which made the outputs non-uniform from cycle to cycle. Fortunately, twisting would not break the materials themselves which were highly flexible owing to the kirigami patterns and their

thin-film characteristics, and the rational interlocking design could be easily restored manually. Meanwhile, the outputs of the pressing mode were 1 order of magnitude larger than those of the other two modes, which was attributed to the contact and separation between the hand and the device as well as the more intimate contact between the FEP and the Cu-paper induced when the clapping force was directly applied onto the surface of the device.

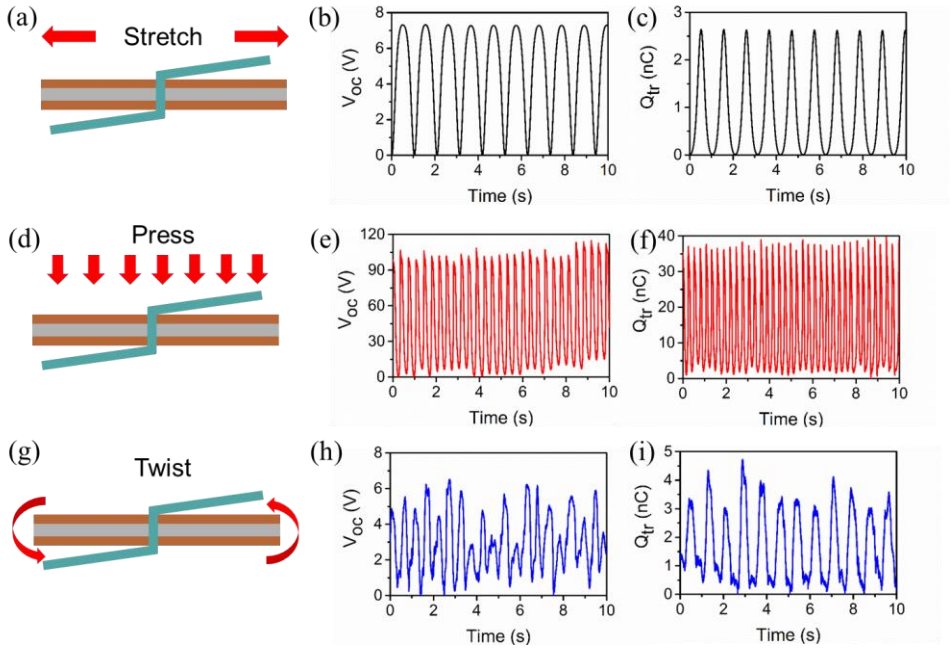


**Figure 19. Different operating modes of the paper-based K-TENG.** (a-c) KTENG under stretching mode with a 28% strain and its $V_{oc}$ and $Q_{tr}$. (d-f) KTENG under pressing mode and its $V_{oc}$ and $Q_{tr}$. (g-i) K-TENG under pressing mode and its $V_{oc}$ and $Q_{tr}$. Reproduced with permission.[40] Copyright 2016, American Chemical Society.

The multiple operating modes of the KTENG endow its potential in a broad range of applications. It can be used to power a small LCD screen, light LED arrays, and detect the book opening and closing with no need of external power sources. In this work, it has also been demonstrated to work as a self-powered acceleration sensor. Figure 20a plots its typical outputs at different acceleration/deceleration rates ranging from 10 m/s$^2$ to 40 m/s$^2$,

and Figure 20b shows the image of the FEP KTENG-based sensor. The two ends of the KTENG was fixed on two beams vertically and the motion direction is perpendicular to the device plane. The relationship between the maximum $V_{oc}$ and the acceleration rates is summarized in Figure 20c, which clearly suggests a linear dependence with sensitivity of 0.080 $V \cdot s^2/m$ and good sensing performance with a detection range from 10 $m/s^2$ to 40 $m/s^2$.

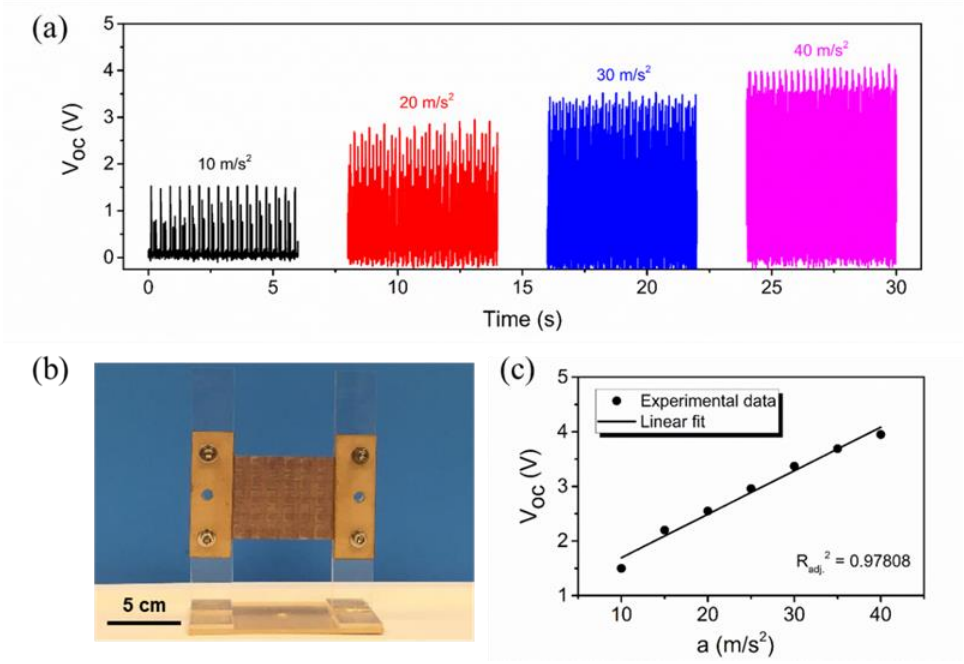


**Figure 20. The application of the paper-based KTENG as a self-powered acceleration sensor.** (a) The measured $V_{oc}$ at several specific acceleration rates. (b) Photograph of the acceleration sensor based on the paper-based KTENG. (c) The summarized relationship between the $V_{oc}$ and the acceleration rates. Reproduced with permission.[40] Copyright 2016, American Chemical Society.

In summary, we demonstrated a versatile approach for fabricating highly stretchable, environmentally friendly paper-based TENG with rationally designed interlocking kirigami structures. The KTENG made of intrinsically inelastic materials could sustain an ultrahigh tensile strain up to 100% and generate maximum outputs of 7.32

V for $V_{oc}$ and 2.64 nC for $Q_{tr}$ with the introduction of kirigami patterns. The interlocking kirigami design not only greatly enhances the rigidity and reliability of the device, but also eliminates the need of additional spacers for the charge separation process as required in conventional TENGs. Owing to its shape-adaptive thin-film design, the KTENG was enabled to harvest energy from various types of motions (stretching, pressing and twisting). The pressing mode can be easily realized by hand clapping and generate a maximum $V_{oc}$ of 115.49 V and a maximum $Q_{tr}$ of 39.87 nC. Furthermore, the KTENG has been demonstrated for a broad range of applications, such as powering a LCD screen, lighting LED arrays, self-powered acceleration sensor and self-powered sensing of book opening and closing. This KTENG work introduces traditional kirigami into the development of stretchable TENG for the first time and verifies its promising applications in both power generation and self-powered sensing.

### *2.3.4 Experimental Methods*

#### 2.3.4.1 Fabrication of KTENG

Ordinary printer paper with a thickness of 100 μm was used as the substrate for the electrode due to its low cost, flexibility and environmental friendliness. The linear kirigami pattern was created using a laser cutter (PLS6.75, Universal Laser Systems) to ensure clean, identical notches. Then Cu was deposited onto the kirigami paper on both sides by magnetron sputtering (PVD75, Kurt J). Thin films of FEP (America Durafilm), PTFE, PET, and Kapton were selected for making the rectangular kirigami structure and all had a thickness of 50 μm. They were laser-cut with the rectangular kirigami pattern and then cleaned with isopropyl alcohol and deionized water, followed by blown dry with nitrogen

gas. Finally the Cu-paper and thin films were assembled together by manually inserting every other row of small rectangles into the linear notches to obtain the KTENG. Extra space was spared on the two ends to adhere the paper and thin films together using double-sided tapes for easy manipulation.

#### 2.3.4.2 Fabrication of Self-Powered Acceleration Sensor

The self-powered acceleration sensor consisted of the KTENG and a vertical holder. The holder was made of 1/8 inch-thick acrylic sheets shaped via laser cutting. The whole device was secured onto a commercial linear mechanical motor, whose motion was controlled to simulate the acceleration and deceleration processes.

#### 2.3.4.3 Characterization

For the measurement of the electric outputs of the KTENG under stretching, one end of the device was fixed on a stationary XYZ linear translation stage (462-XYZ-M, Newport Inc.), and the other end was bonded to a linear motor which provides cyclic tensile strains. $V_{oc}$, $Q_{tr}$ and $I_{sc}$ were measured by a Keithley 6514 system electrometer. The resistance of the as-fabricated Cu-paper was measured by an Amprobe 15XP-B digital multimeter. For the measurement of the stress-strain response of the KTENG, one end was fixed on the stationary stage and the other end was secured on a force senor (DFS-BTA, Vernier Software & Technology, LLC) attached to the linear motor. The forces required for different strains controlled by the linear motor were recorded and then divided by the cross-section area of the device to obtain corresponding stresses.

## 2.4 Sunlight-Triggerable Transient TENG

Transient electronics is an emerging class of electronic devices with temporal functional profiles whose degradation can be triggered on demand.[110-113] Such devices can disappear by vaporization, liquefaction, or dissolution in solvents and thus eliminate the need of retrieval after a period of stable operation.[114] They have found potential applications as medical diagnostic and therapeutic devices that can resorb into the body, environmental sensors that do not require recovery after data collection, and consumer devices that can be easily disposed without hazards.[115] The potential feature of disappearance with minimal or non-traceable remains also enables transient electronics to find opportunities in privacy or security applications where stealth is required or reverse engineering needs to be avoided.

Pioneering efforts on transient electronics focused on solution dissolution of polymer matrix. Bioresorbable polymers such as silk, polycaprolactone, poly(glycolic acid) and poly(L-lactide-co-glycolide), were used as substrates,[116-118] and biocompatible, implantable devices such as transistor,[110] ring oscillators[119] and energy harvesters,[120] have been demonstrated. The lifetime of such devices is controlled by the dissolution rate of the materials in the surrounding aqueous solution, making them unsuitable for non-biological applications. To achieve better control of the device lifetime and expand the utility of transient electronics in non-biological scenarios, the use of metastable polymers whose depolymerization can be triggered rapidly by specific stimuli, such as humidity, heat, light and mechanical stress, has been proposed as an alternative approach for achieving device transience.[114, 121] They have been used for the development of transient resistors, diode/transistor arrays, and organic LEDs.[114, 121, 122] Transient power sources, however, are indispensable for a fully transient electronic system. To our best knowledge, only transient

energy harvesters whose degradation requires aqueous solution have been demonstrated.[113, 120, 123, 124]

In this work, a TENG whose degradation can be triggered simply and rapidly by sunlight is reported. Its substrate was made of a metastable polymer cyclic poly(phthalaldehyde) (PPHA) and a photosensitive package consisting of a photoacid generator (PAG) called Rhodorsil Faba and a photosensitizer (PS) called anthracene. PS was used to absorb and transfer the energy of ultraviolet (UV) light (365 nm – 400 nm) to PAG via photo-induced electron transfer, while the latter generated protons to trigger the depolymerization of PPHA. The concept of transient electronics in the field is illustrated in Figure 21. The proposed devices can be easily disposed in ambient environment by transforming from solid state into "vanishable" liquid form upon applying an environmental trigger. As evidenced by the degradation photographs of a transient TENG device based on cyclic PPHA, it could be absorbed by soil and leave minimal traces within ten minutes under winter sunlight, whose UV component functioned as the degradation trigger.

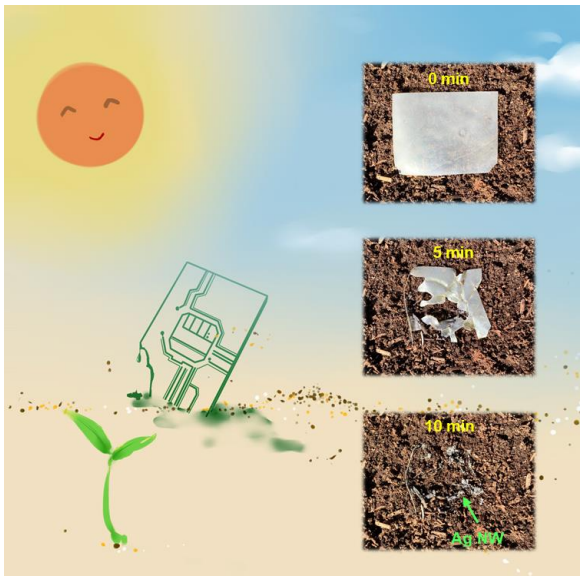


**Figure 21. Schematic of transient electronics in the field and photographs of a transient TENG device under winter sunlight as a proof of concept.**

### *2.4.1 Transient Polymer PPHA*

Low ceiling temperature, cyclic PPHA was cationically polymerized in dichloromethane (DCM) at -80 °C using boron trifluoride etherate ($BF_3OEt_2$) as the catalyst. The reaction scheme is shown in Figure 22a. The continuous insertion mechanism of monomer, ortho-phthalaldehyde (oPA), into the cyclic structured PPHA, as described in Schwartz *et al.*,[125] ensured the formation of high molecular PPHA until the reaction equilibrium was achieved. The acetal linkage on the PPHA backbone is highly susceptible to strong acid attack to result in ring-opening of cyclic structure.[126] Upon ring-opening of cyclic PPHA, the end-group unprotected PPHA would rapidly depolymerize back to oPA due to its low ceiling temperature nature. In this study, a superacid (i.e., $pK_a$ less than that of 100% pure sulfuric acid) was in-situ produced upon exposure to UV/visible light using photo-induced electron transfer (PiET) reaction mechanism between anthracene and Rhodorsil FABA.[127] Figure 22b explains the reaction mechanism of PiET reaction.

Anthracene acted as a photosensitizer (PS) to absorb the energy in the UV spectrum (365 nm – 400 nm) while Rhodorsil FABA functioned as a PAG to produce the superacid with proper energy input. The excited PS upon light exposure played the role as an electron donor that can transfer electrons onto a lower energy molecular orbital of PAG due to thermodynamic favorability.[127, 128] This redox reaction resulted in the homolytic cleavage of PAG and formation of strong superacid that can rapidly depolymerize the film. All films were casted with addition of an ionic liquid (IL) plasticizer, 1-methylpyrrolidinium bis(trifluoromethylsulfonyl)imide (BMP TFSI). It has been previously reported that pyrrolidinium-based IL can be used to effectively plasticize PPHA film to make it more fracture resistant and flexible.[129] Moreover, IL enhances the transient property, due to its good solubility of oPA monomers, resulting in formation of liquid byproducts that can be absorbed into the surrounding environment.

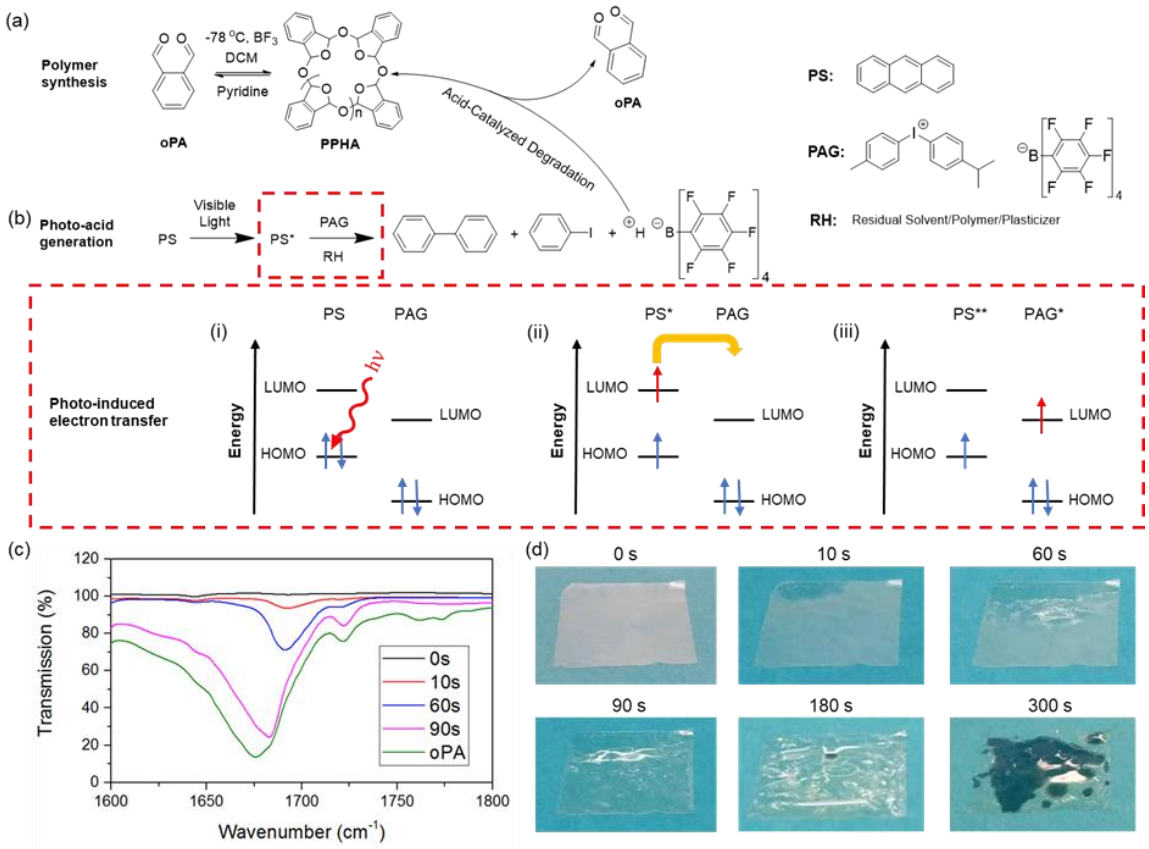


**Figure 22. Synthesis and degradation of transient polymer PPHA.** (a) Cationic polymerization of cyclic PPHA. (b) Degradation mechanism of PPHA caused by photo-induced electron transfer reaction. (c) In-situ ATR-IR characterization of photo-induced degradation of PPHA. (d) Photographs of degradation of PPHA after irradiation under 365 nm UV for various periods of time.

Attenuated total reflectance infrared spectroscopy (ATR-IR) was used to monitor the degradation process of cyclic PPHA film exposed for different length of time, shown in Figure 22c. The neat oPA monomer was investigated as well to find the expected spectrum of depolymerized product. The formation of carbonyl stretching from aromatic aldehyde is expected to be observed around 1670 $cm^{-1}$. The small peak at around 1720 $cm^{-1}$ corresponded to the carbonyl stretching from carboxylate group from phthalic acid. The formation of phthalic acid was due to the oxidation of oPA after exposing to the humid air. Samples were exposed to an exposure source with an intensity of 4 $mW/cm^2$. At the

beginning of exposure, no peaks were observed in between 1650 $cm^{-1}$ - 1720 $cm^{-1}$. With the increase of exposure time, carbonyl stretching from both aromatic aldehyde and carboxylate group became predominant. Exposure for 90 s resulted in complete degradation of cyclic PPHA with a nearly overlapped spectrum with neat oPA monomer. Figure 22d shows the photographs of the degradation process of PPHA. The film started to degrade after 10 s exposure with liquid byproducts started forming on the surface. More liquid appeared on the film surface with the extent of exposure. Upon exposure for 90 s, the surface of the film completely degraded. Further exposure till 300 s resulted in the complete degradation of the film and form liquid byproducts that can be absorbed into the paper background. It is noteworthy that the degradation rate can be further tuned via changing ratio of PAG.

### *2.4.2 Triboelectric Property of PPHA*

TENG has been proven to be an effective tool in characterizing the triboelectric performance, or the ability of capturing surface charges during triboelectrification, of materials.[12] To figure out the position of our PPHA film in the triboelectric series, six contact-separation-mode TENGs[2, 17] made of PPHA and different commonly used triboelectric materials, including polyurethane (PU), nylon, polyethylene (PE), PET, Kapton and Teflon® FEP, were fabricated and their electrical outputs are summarized in Figure 23. It is noteworthy that the relative position of two materials in the triboelectric series only dictates the direction (signal sign), not the amount, of charge transfer during contact electrification, since the absolute value of TENG output is highly dependent on other factors such as film thickness and material composition as well.[69, 71] As in Figure 23(a-c), the PU-PPHA TENG generated opposite electrical signals compared to others,

which suggests that PU has opposite charge affinity compared to other reference materials when in contact with PPHA. Therefore, a new triboelectric series with PPHA locating between PU and nylon can be obtained, as shown in Figure 23d. The power output of the Kapton-PPHA TENG was measured at various load resistance and it delivered a maximum output power of 28.4 μW $cm^{-2}$ with a matched resistance of 88 MΩ.

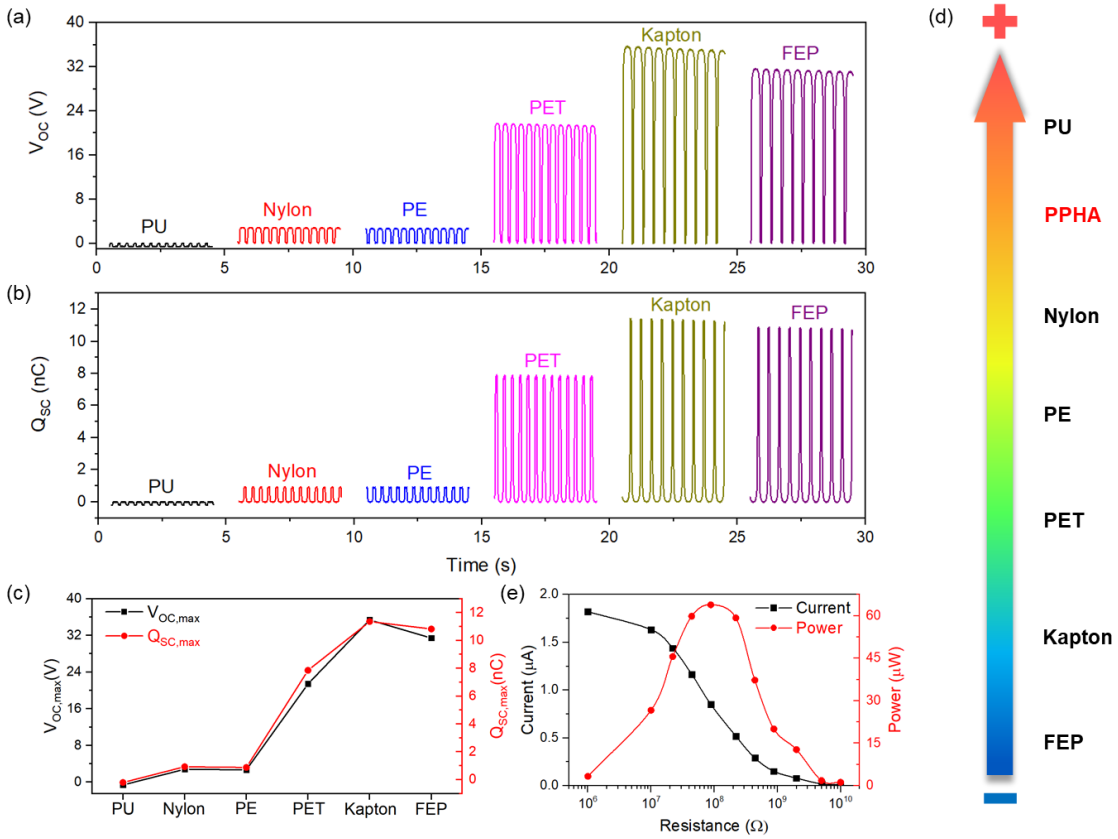


**Figure 23. Triboelectric performance of PPHA.** (a) Open-circuit voltage output $V_{OC}$ and (b) short-circuit charge transfer $Q_{sc}$ with respect to different materials. (c) Summary of $V_{oc}$ and $Q_{sc}$ data. (d) Plot of triboelectric series including PPHA. (e) Current and power outputs from a PPHA-Kapton TENG device at various load resistance.

### *2.4.3 Performance of PPHA-Based Transient TENG*

To achieve a fully degradable transient TENG, silver (Ag) NWs, rather than conventional metallic films, were used as the electrode on the PPHA film. The schematic

in Figure 24a illustrates the fabrication process of the transient TENG, starting with the deposition of Ag NWs on a glass substrate, followed by the deposition of PPHA solution, and ending with the peel-off of the PPHA film coated with Ag NWs. The as-fabricated PPHA-Ag thin film can work as a single-electrode TENG[27, 40, 130] for energy harvesting or sensing upon contact with other materials. To characterize its continuous performance under the 365 nm UV irradiation with an intensity of 4 mW/cm$^2$, the temporal profile of $V_{OC}$ of the PPHA-Ag thin film in contact and separation with a Cu-coated Kapton film was recorded. The voltage drop from 30 V to 0 V in Figure 24b indicates that its function of electricity generation was attenuated rapidly starting from 30 s UV irradiation and fully disappeared after 90 s. This temporal profile matches well with the observation of the PPHA-Ag film during UV-triggered degradation, as shown in Figure 24c. After 30 s irradiation, the surface of the film started to liquify as evidenced by the change of reflectance when compared to the original film. At 90 s, the whole surface had liquified and the film shape was maintained due to the Ag NWs backbone, which justifies the loss of electrical output as in Figure 24b when solid contact is required for energy conversion. Subsequently, the liquid byproducts were absorbed by the drying agents at the bottom and the solid residue of Ag NWs was mixed with the small balls after stir.

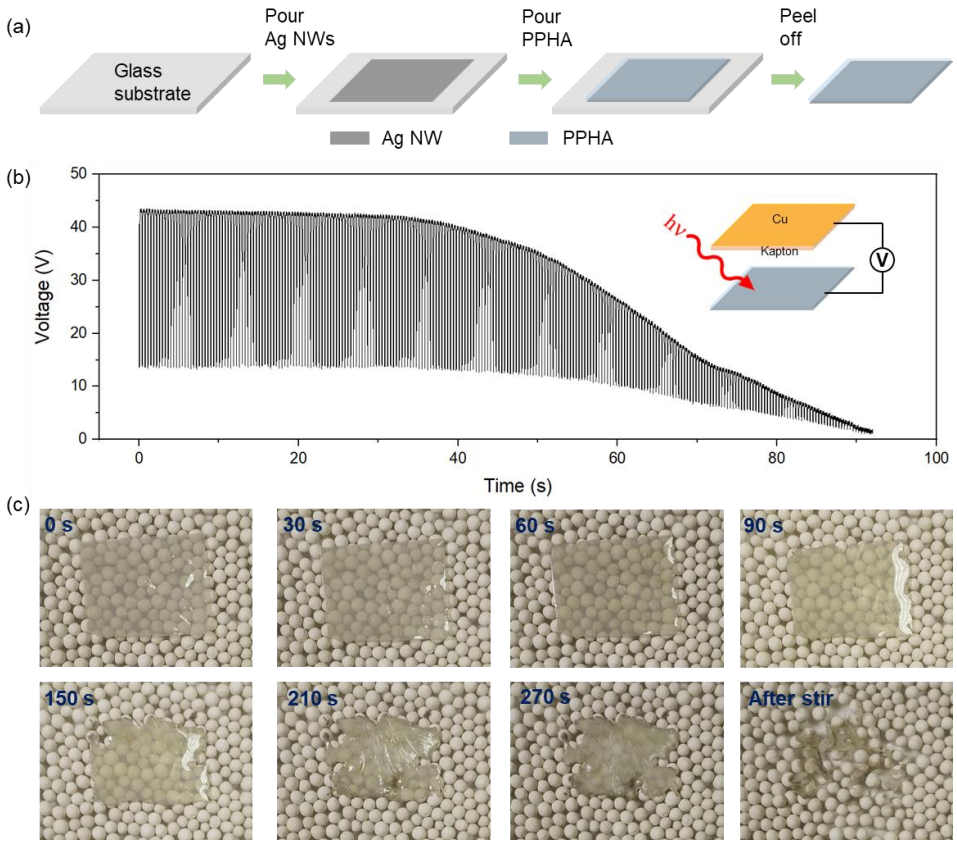


**Figure 24. Transient TENG using PPHA and Ag NWs.** (a) The fabrication process of Ag-NWs coated PPHA thin film. (b) The voltage output of the PPHA-Ag thin film in contact and separation with a Cu-coated Kapton film under 365 nm UV irradiation. (c) Photographs of degradation of PPHA-Ag thin film after irradiation under 365 nm UV for various periods of time.

Furthermore, the coating of Ag NWs enhanced the mechanical strength of the PPHA film, with an increase in yield stress from 3.09 MPa to 6.75 MPa and an increase in modulus of resilience from 0.01 J/m$^3$ to 0.05 J/m$^3$, while maintaining similar Young's Modulus at around 460 MPa, as in Figure 25a. Thermogravimatric analysis (TGA) was also conducted on our PPHA-Ag film to investigate its thermal stability and the result in Figure 25b shows that the film remained stable up to at 113 °C, well beyond normal ambient temperature.

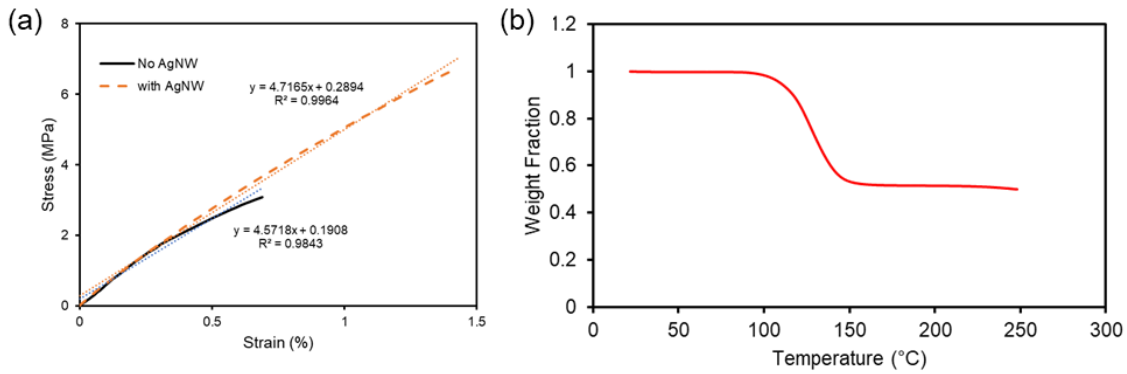


**Figure 25. Characterization of PPHA-Ag film.** (a) Tensile stress-strain response. (b) TGA result.

### *2.4.4 Demonstrations using PPHA-Based Transient TENG*

To demonstrate the electricity generation capability of our transient TENG, it was operated in the single-electrode mode by hand tapping and used to power six LEDs connected in series. The LEDs were lit up successfully initially, but after 365 nm UV radiation for 2 minutes, the transient TENG lost the power function due to the liquefaction, as evidenced by the liquid droplets on the PTFE film in Figure 26a. Besides energy harvesting, the transient single-electrode TENG can be used for touch sensing as well. As in Figure 26b, a transient TENG was used as a touch sensor to trigger an alarm bell through a customized control circuit. The bell could be activated by the transient TENG sensor before UV radiation but not after. In Figure 26c, a transient triboelectric acoustic sensor was fabricated by coupling the PPHA-Ag film with a paper sheet covered by Cu and Kapton. It was demonstrated as a microphone to record music played by a speaker, with the output electric signals plotted in Figure 26c. As expected, UV exposure of the device liquified the film and disabled the sound recording function. These demonstrations show that the transient TENG can be "deactivated" via UV/sunlight radiation after their designed

use and the resulted liquefaction enables the degradation residue to be easily disposed. Besides, these devices may also be used for secret monitoring in special circumstances.

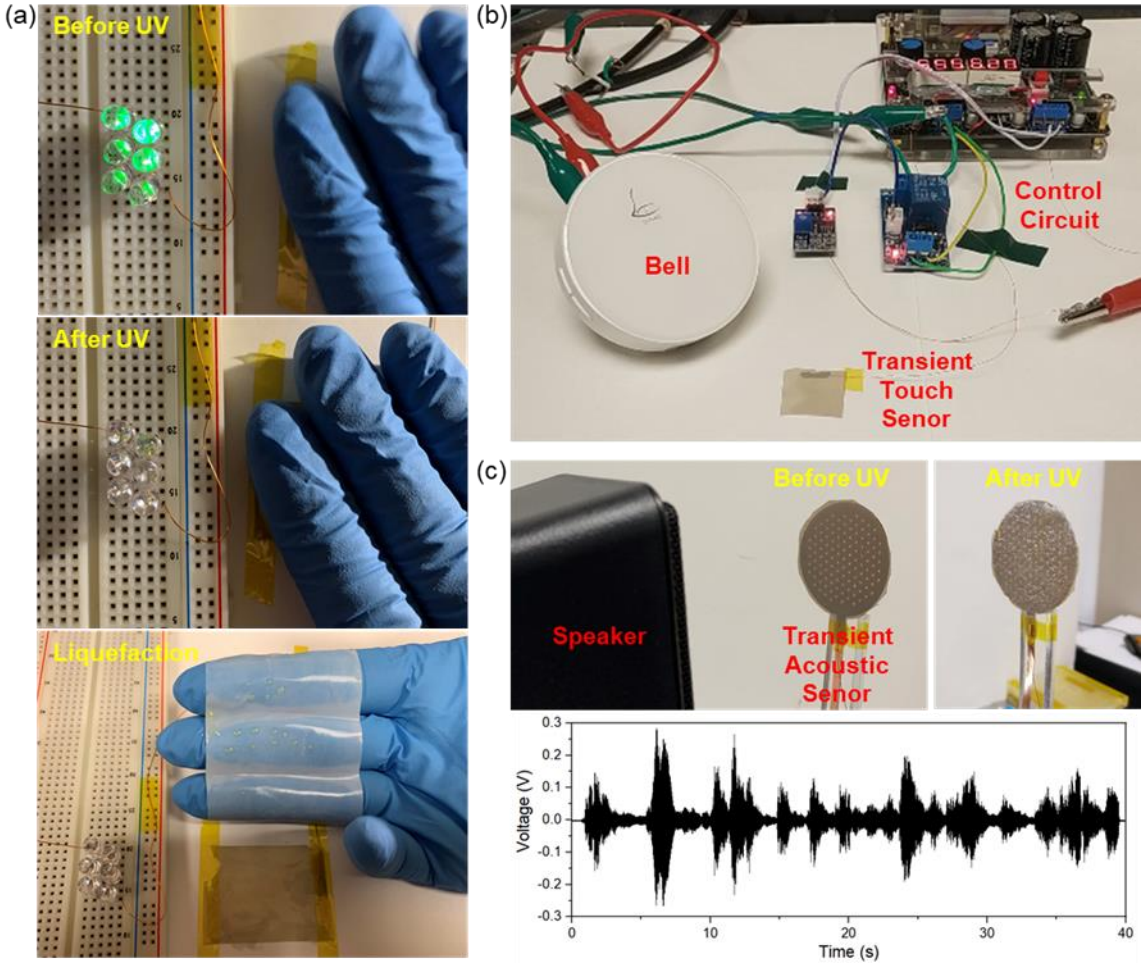


**Figure 26. Demonstrations using our transient TENG.** (a) Electricity generation for lighting up LEDs before UV radiation and the loss of energy harvesting function after UV radiation due to liquefaction. (b) Transient touch sensor for alarm triggering. (c) A transient triboelectric acoustic sensor and its electrical outputs from music playing.

This work presents a sunlight-triggerable, PPHA-based transient TENG which can be used for both mechanical energy harvesting and active sensing applications. Its degradation is not restricted to aqueous environment and can be achieved within several minutes even under winter sunlight. The degradation rate can be further tuned via the

composition of photosensitive agents. The liquid byproducts after degradation can be easily absorbed by soil or paper with minimal residue remaining, which shows its great potential in field application where disposability or stealth is desired. The adjustment of triboelectric property of PPHA film can be explored in future work by surface modification to achieve higher energy conversion efficiency. This work not only broadens the applicability of TENG as transient power sources and sensors, but also expands the use of transient functional polymers towards advanced energy and sensing applications.

### *2.4.5 Experimental Methods*

#### 2.4.5.1 Materials

Tetrakis(pentafluorophenyl)borate-4-methylphenyl[4-(1-methylethyl)phenyl]iodonium (PAG) were purchased from TCI Chemicals. Anthracene was purchased from Alfa Aesar. 1-Butyl-1-methylpyrrolidinium bis(trifluoromethylsulfonyl)imide (BMP TFSI) was purchased from Iolitec. Tetrahydrofuran (THF) was purchased from BDH. All chemicals were used as received. Cyclic PPHA was cationically polymerized using boron trifluoride diethyl etherate ($BF_3OEt_2$) as the catalyst at -80 °C following the procedure of Schwartz et al.[125] The number-average molecular weight ($M_n$), weight-average molecular weight ($M_w$), and polydispersity index ($Đ = M_w/M_n$) of dried cyclic PPHA was determined by GPC (Shimadzu) equipped with an LC-20 CE HPLC pump and a refractive index detector (RID-20 A, 120 V), using THF as the solvent. The measured $M_n$ is 355 kg/mol and Đ is 1.26. Nylon (50 μm), PE (100 μm), PET (50 μm) and Kapton (25 μm) films were purchased from McMaster-Carr. Teflon® FEP film (25 μm) was purchased from American Durafilm.

These films were used as received. Waterborne PU dispersion (Bondthane$^{TM}$ UD-615) was obtained by the courtesy of Bond Polymers International. PU film (50 μm) was made by spin-coating the dispersion onto the substrate. Ag NWs dispersion (Agnw-L70) was purchased from ACS Material. Isopropyl alcohol (IPA) 99% was purchased from VWR.

#### 2.4.5.2 Fabrication of PPHA films

PPHA films were formulated in a clean scintillation vial by dissolving all solid contents (i.e., PPHA, PAG, anthracene) and liquid contents (BMP TFSI) in THF. Weight ratio of 12:1 for THF and PPHA were used for all formulations in order to obtain the viscosity to spread and cover the PTFE petri dishes for drying. All polymer formulation was prepared containing 10 part per hundred resin (pphr) PAG, 2.1 pphr anthracene, and 100 pphr BMP TFSI, with all weight fraction referenced to the weight of PPHA added into the formulation. The sample was dried in a nitrogen-rich, pressurized chamber at 15 psig for 18 hours, followed by slow bleeding of THF out of chamber to relieve head pressure for 3 hrs. Samples were then taken out of the pressurized chamber and peeled off the substrate. All samples were then flattened and allowed further drying for 3 days before taken to test. All dried samples have an average thickness of 100 μm.

#### 2.4.5.3 In-Situ ATR-IR Characterization of PPHA Films

The degradation of 100 μm thick PPHA films was characterized by a Nicolet iS50 FT-IR instrument. Attenuated total reflectance (ATR) mode was used and total scans of 32 were performed for each sample. Samples were exposed using a portable B-100 series UV lamp with an intensity of 4 mW/cm$^2$ at 365 nm. Data were collected after samples were

exposed for 0 s, 10 s, 60 s, and 90 s. The formation of carbonyl peak at 1680 $cm^{-1}$ were compared to the monomer oPA for indication of the extent of polymer degradation.

#### 2.4.5.4 Fabrication and Measurement of TENGs for Triboelectric Series

Six TENGs having PPHA and six different reference materials (PU, nylon, PE, PET, Kapton and FEP) in contact and separation were fabricated to locate the relative position of PPHA in the triboelectric series. Acrylic plates (15 mm wide × 15 mm long × 1/8 inch thick) were used as substrates. For the side with PPHA, the acrylic plates were covered with foam tape, Cu tape and PPHA sequentially. For the side with reference materials, the acrylic plates were covered with Cu tape and reference materials sequentially. The contact-separation motion between the PPHA and reference materials were driven by a linear motor with a maximum gap distance of 20 mm. The electrical outputs were measured using a Keithley 6514 electrometer.

#### 2.4.5.5 Fabrication of PPHA-Ag films

Ag NWs dispersion was firstly diluted using IPA with a volume ratio of 1:5, and then coated onto clean glass substrates using pipettes. The glass substrates were placed on an optical table overnight to ensure uniform coating of Ag NWs and the complete dry of IPA. Nylon strips were used as fences to create enclosed area on glass substrates to control the surface area and thickness (100 μm) of the casted PPHA layers. PPHA was formulated as described above and uniformly poured into the prepared glass substrates. All films were allowed to dry following the same procedure as described above. The pressure-dried films were allowed for further drying for 24 hours in a dark ambient environment. A razor blade was then used to lift off a corner of the PPHA-Ag film from the glass substrate. Films were

then submerged into a room-temperature water bath for 15 mins, followed by peeling off the entire film from each glass substrate.

#### 2.4.5.6 Mechanical Testing of PPHA and PPHA-Ag Films

Mechanical properties of PPHA and PPHA-Ag films were characterized using TA Instrument Q800 Dynamic Mechanical Analyzer. Samples had dimension of 11 mm × 7 mm × 0.1 mm (length × width × thickness). Stress-strain curves of samples were measured at 23 °C with a preload force of 0.015 N and were elongated with a constant force ramp rate of 1 N/min until sample-failure occurred, as shown in Figure S1. Young's modulus [MPa], strain to break value [%], and yield stress [MPa] were obtained from the stress-strain curve. The ability of a material to absorb energy without fracturing is represented by modulus of resilience [$J/m^3$], which was calculated as

$$Modulus\ of\ \ Resilience = \frac{Yield\ \ Stress^2}{2 \cdot \left( Young's\ Modulus \right)} \tag{19}$$

#### 2.4.5.7 Thermal Stability Measurement of PPHA-Ag Film

Thermogravimatric analysis (TGA) was performed using a TA Instrument Q50 under inert nitrogen condition with a constant flow rate of 40 ml/min. Weight of 6.112 mg PPHA-Ag film was loaded into the TGA furnace and investigated for its thermal stability. Furnace temperature was ramped at 5 °C/min to 250 °C. Figure S2 shows the weight fraction change of the loaded film with the ramping of temperature. The onset decomposition of the film happened at 113 °C. About 50% residual weight was leftover, due to the residual Ag NWs and non-volatile BMP TFSI.

#### 2.4.5.8 Measurement of Temporal Voltage Profile of PPHA-Ag Film

A PPHA-Ag film with an area of 15 mm × 15 mm was attached to an acrylic plate with foam cushion and under 365 nm UV irradiation (4 mW/cm$^2$) continuously during the measurement. A Kapton film with Cu electrode on an acrylic plate as above was driven by a linear motor to have periodic contact and separation with the PPHA-Ag film, with a maximum gap distance of 20 mm. The $V_{oc}$ was measured using a Keithley 6514 electrometer.

#### 2.4.5.9 Fabrication of Transient Acoustic Sensor

A PPHA-Ag film was coupled with a paper sheet covered by Cu and Kapton to form a double-electrode triboelectric acoustic sensor (diameter: 4cm). Cu was coated onto the paper via evaporation and Kapton film with single-sided adhesive was pasted onto the Cu side of the paper. Uniform holes (diameter: 1mm; distance: 3mm) were generated on the paper sheet to reduce air damping during acoustic sensing.[48]

# CHAPTER 3. APPLICATION OF TENG FOR SELF-POWERED SYSTEMS

## 3.1 Recent Progress of TENG as Micro/Nano Power Sources

TENG has found vast applications as micro/nano power sources for self-powered systems by harvesting biomechanical or ambient energy, such as human walking, heartbeats, machine vibration, and wind energy. Recent critical progress in this field can be categorized into two groups based on the design methodology; one is a shape-adaptive TENG for conformal power sources and the other is a fiber-based TENG for wearable power sources. It should be emphasized that these two methodologies are intertwined rather than mutually exclusive.

Shape-adaptive devices adopt elastic and deformable materials so that they can be applied on a human body in a more natural and efficient way. For example, a tube-like, silicone-based TENG that can be installed under the shoe or on clothing (Figure 27a) was developed to harvest electrical energy from human walking for powering wearable electronics such as watches and fitness trackers.[70] Subsequently Yi *et al.* reported a highly stretchable TENG consisting of conductive liquid and soft rubber.[131] This stretchable TENG could easily conform to uneven surfaces and was demonstrated as a shoe pad and wearable bracelet for harvesting energy from human walking and hand tapping (Figure 27b). The stretchability of TENG was further improved to a uniaxial strain of 1160% by Pu et al. using ionic conductors as the electrode.[132] The ultra-stretchable, skin-like TENG (STENG) had a sandwich-like architecture with a layer of ionic hydrogel encapsulated

between two elastomer films (Figure 27c). A maximum power density of 35 mW/m$^2$ was achieved by using Nylon to make contact-separation with the PDMS-based STENG. Aside from *in vitro* energy harvesting, a flexible and biodegradable TENG (BD-TENG) was reported by Zheng et al. for short-term *in vivo* biomechanical energy conversion.[113] The BD-TENG had a multilayer structure made of biodegradable polymers (BDPs) and resorbable metals (Figure 27d). It operated through the contact separation between two selected BDP layers with nanopatterned surface structures. The BD-TENG was proposed to harvest energy from heartbeats, respiratory motion, and blood pressure for transient, implantable, self-powered therapeutic or diagnostic medical devices, with electric-field-assisted neuron cell orientation successfully demonstrated as an application.

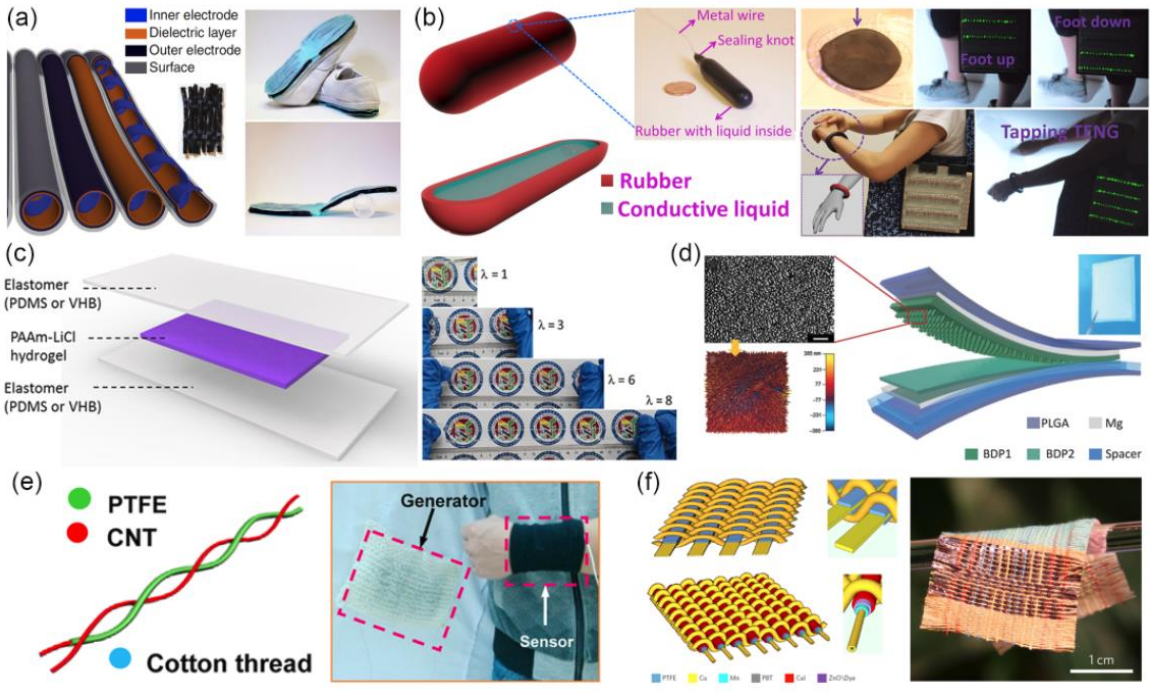


**Figure 27. TENG as micro/nano energy sources.** (a) A tube-like, silicone-based TENG for harvesting biomechanical energy. (b) A highly stretchable TENG consisting of conductive liquid and soft rubber. Reproduced under the terms of the CC-BY-NC 4.0 license.[131] Copyright 2016, The American Association for the Advancement of Science. (c) A skin-like TENG consisting of ionic hydrogel and elastomer films. Reproduced under

the terms of the CC-BY-NC 4.0 license.[132] Copyright 2017, The American Association for the Advancement of Science. (d) An implantable, biodegradable TENG for in vivo biomechanical energy harvesting and electrical stimulation. Reproduced under the terms of the CC-BY-NC 4.0 license.[113] Copyright 2016, The American Association for the Advancement of Science. (e) The first fiber-based TENG and the demonstration of a power shirt. Reproduced with permission.[133] Copyright 2014, American Chemical Society. (f) A hybrid power textile for harvesting solar and mechanical energy simultaneously. Reproduced with permission.[134] Copyright 2016, Springer Nature.

Fiber-based power sources, such as batteries, supercapacitors and nanogenerators, have attracted great interest in the past decade due to the emergence of wearable electronics. The first fiber-based TENG that could be woven into fabric (Figure 27e) was proposed by Zhong *et al.* in 2014.[133] The fabricated device consisted of two kinds of core-shell structured fibers, with one being carbon-nanotube (CNT) coated cotton threads and the other having an additional coating of PTFE on top of the CNT layer. The power generation mechanism was based on the contact separation between PTFE on one fiber and CNT on the other one, which was induced by the change in the interfiber gap when the woven cloth underwent mechanical deformation. A "power shirt" made from a lab coat using the fiber-based TENG was demonstrated to charge a commercial capacitor and trigger a wireless body temperature monitoring system. Subsequently 3D woven structures were introduced to the fiber-based TENG design to improve its output performance.[135] The increased number of dielectric layers in 3D woven TENG successfully improved the power outputs when compared to single-layer woven TENG. Fiber-based TENG can also be integrated with other energy harvesting technologies to achieve higher output power and harvest various kinds of energy simultaneously. Chen et al. reported a hybrid power textile consisting of a fabric TENG and photovoltaic (PV) textile (Figure 27f), which could harvest mechanical energy and solar energy simultaneously and achieve higher electrical outputs.[134] The hybrid textile was successfully demonstrated to charge a phone and an

electronic watch in a wearable manner. A hybridized self-charging power textile was also demonstrated by integrating fiber-shaped TENG, solar cells and supercapacitors together.[136]

## 3.2 Self-Powered Iontophoretic Transdermal Drug Delivery System Driven and Regulated by Biomechanical Motions

Transdermal drug delivery (TDD), which refers to the transport of pharmacological agents through the skin, has become a common medical practice with over twenty commercially available transdermal drugs approved by the Food and Drug Administration (FDA).[137-139] Compared to other alternatives like oral delivery and hypodermic injection, TDD has many advantages such as non-invasive, painless, convenient, inexpensive and self-administered. It avoids the risk of disease transmission by needle re-use and the first-pass hepatic metabolism of drugs. It enables on-demand administration of drugs at targeted skin sites, making it attractive for long-term treatment without the risk of high-level spikes of therapeutics in the systemic circulation.[140] The availability of drugs that can be delivered via TDD systems have been extended by various methods of enhancing skin permeability, including the use of chemical molecules, biomolecules and physical tools.[138]

Iontophoresis has proven to be an effective physical permeation enhancement approach for TDD to deliver hydrophilic and/or charged molecules across the skin.[141-143] An electric current (typically < 0.5 $mA/cm^2$) is applied to the skin to drive the flow of charged molecules, while the resulted electroosmotic flow of biofluids transports the charge-neutral molecules.[138] Although iontophoretic TDD systems has been commercialized for local dermal analgesia, the application of such electrically controlled

patches is hindered by the need of external power sources that are cumbersome and hazardous, as well as the complicated electrical components required for feedback control. Previously Ogawa et al. reported a completely organic iontophoresis patch with a built-in biofuel cell as a lightweight and safe power source, but it did not offer feedback control since the current could not be adjusted once the patch was mounted on the skin.[144] To address these issues, a self-powered wearable iontophoretic TDD system based on biomechanical motion sensing and energy harvesting is proposed in this work for closed-loop motion detection and therapy.

### *3.2.1 Proposed Self-Powered Iontophoretic TDD System*

To realize a wearable iontophoretic TDD system that offers on-demand therapeutic delivery without external power sources, our proposed system consists of a wearable TENG as the power source and a hydrogel-based soft patch as the drug carrier (Figure 28). TENG, which can convert mechanical energy into electricity through the coupled effects of triboelectrification and electrostatic induction, has emerged as a promising power source for the era of IoT owing to its merits of low cost, broad material availability, light weight and high efficiency at low operation frequencies.[17] It has found vast applications as micro power sources for self-powered wearable or implantable systems.[113, 145-148] Recently, TENG was proposed as a voltage source for electroporation drug delivery but it requires invasive penetration of a metallic electrode under the skin for TDD.[149] In this work, a wearable TENG is proposed as a current source to control the iontophoretic TDD in a non-invasive manner (Figure 28b). The TENG can be designed in various form factors and mounted onto different parts of body to scavenge electric energy from biomechanical motions. The rationally designed drug patch is made of soft materials and can be

conformally attached onto the targeted spots on human skin (Figure 28c). The drug patch is electrically connected to the TENG, and thus the TENG output, which is stimulated by body motions, can be used to accelerate the transdermal drug release rate via iontophoresis without external power sources. Since the body motions for TENG operation can be either involutory (breathing, tremor) or intentional (arm bending, walking), this self-powered TDD system offers both sustained drug release and intentional release with feedback control. For example, the involuntary motions of a patient with tremor will trigger the TENG operation and facilitates the on-demand drug release, while patients with ankle injury can receive extra dosing of analgesic automatically during walking when the TENG is mounted under the foot.

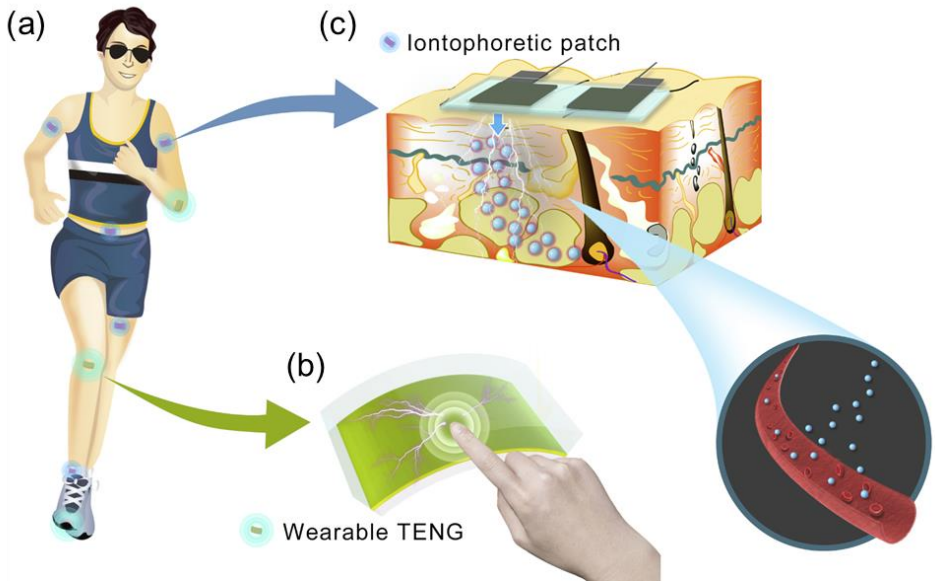


**Figure 28. Schematic of self-powered iontophoretic TDD system.** (a) Man in motion wearing the TDD devices. (b) Illustration of wearable TENG for motion detection and biomechanical energy harvesting. (c) Illustration of drug patch that delivers drug through skin via iontophoresis.

### *3.2.2 Electrophoretic Flow Driven by TENG*

The feasibility of using TENG to power iontophoretic TDD was firstly investigated via the study of the electrophoretic flow driven by TENG (Figure 29). A customized diffusion cell consisting of 4 unit cells separated by 3 cellulose membranes, was fabricated as the experimental apparatus (Figure 29a). The two inner cells, i.e. the donor cell and the acceptor cell, were separated by a cellulose membrane with a pore size of 3 μm, while the two outer cells were separated from the inner cells by cellulose membranes with a pore size of 0.45 μm and worked as buffer layers to minimize the electrolysis of test molecules at the electrodes. At the beginning of tests, all four cells were filled with the same amount of liquid (1 mL), with only the donor cell having the PBS solution containing test molecules and the other three having the plain PBS solution. A contact-separation-mode TENG [71, 150, 151], where PTFE was used as one triboelectric material and Al as the other triboelectric material and electrodes, was used in the tests and operated by an electrodynamic shaker. It was connected to the two carbon-cloth electrodes of the customized diffusion cell through a rectifier, which converted the alternating current output of TENG into direct-current electricity.

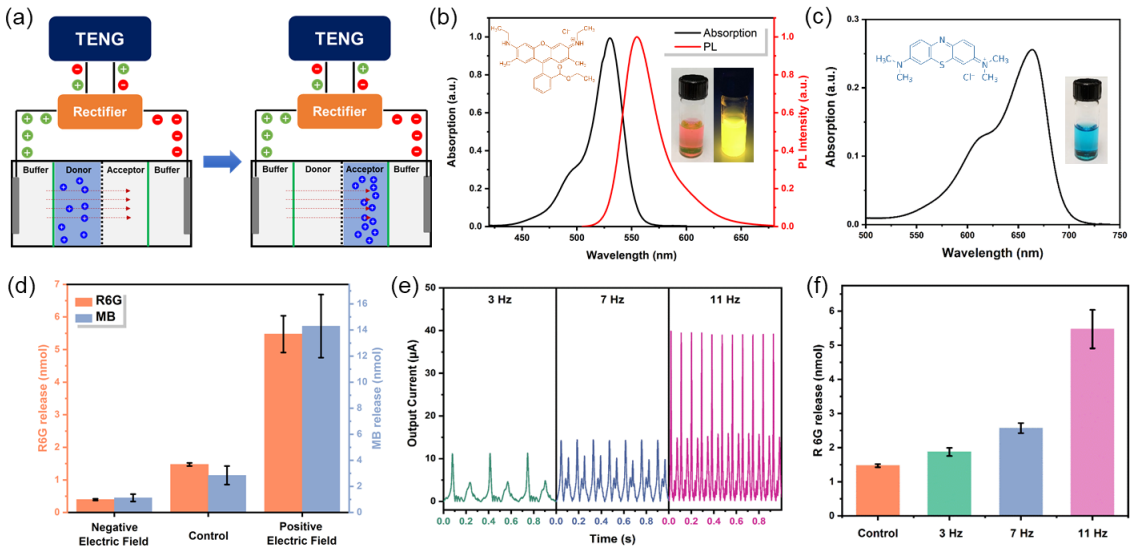


**Figure 29. Study of electrophoretic flow driven by TENG.** (a) Schematic of experimental setup using a diffusion cell. (b) Absorption and photoluminescence spectra, structural formula (inset, left), bright-field and fluorescence photographs (inset, right) of R6G. (c) Absorption spectrum, structural formula (inset, left), bright-field photographs (inset, right) of MB. (d) Effects of electric field direction on diffusion of small molecules. (e) Output currents of TENG under different operation frequencies. (f) Effects of TENG operation frequency on diffusion of small molecules.

Rhodamine 6G (R6G), a cationic fluorescent organic dye with maximum absorption at 530 nm and emission at 556 nm (Figure 29b), and methylene blue (MB), a cationic medication and dye with maximum absorption at 665 nm (Figure 29c), were used as the test materials. In particular, MB can be used as an antimalarial agent or be used to treat methemoglobinemia and Alzheimer's disease.[152] The effects of electric field direction from TENG on the dye diffusion rate was firstly studied, with experimental results shown in Figure 29d. The concentration of R6G and MB in the acceptor cell was calculated from the calibration curves prepared with standard solutions. Under a positive electric field (from the donor cell to the acceptor cell), the transported amount of dye molecules in the accepted cell increased significantly after 30 minutes of TENG operation at a frequency of 11 Hz, while the amount decreased when the electric field was reversed. This relationship between

diffusion rate and electric field direction applied to both R6G and MB and fit well with our expectation. A positive current could accelerate the flow of positively charged dye molecules in the PBS solution from the donor cell to the acceptor cell. Meanwhile, an opposite current would hinder the diffusion of dye molecules driven by concentration difference, resulting in a smaller diffusion rate. The effects of TENG operation frequency on the diffusion rate were studied as well. Figure 29e shows the current flowing through the diffusion cell when the TENG operated at different frequencies. Higher operation frequency brought higher number and larger amplitude of current peaks, which would result in a larger driving force for the electrophoretic flow and thus a faster diffusion rate of the targeted molecules, as evidenced by the amount of transported R6G in Figure 29f after 30 minutes of TENG operation at different frequencies.

### *3.2.3 Hydrogel-Based Iontophoretic Drug Patch for TDD*

To realize the proposed self-powered iontophoretic TDD in a non-invasive manner, a hydrogel-based drug patch was rationally designed and fabricated (Figure 30a). The drug patch consists of two side-by-side hydrogel cells and two embedded carbon-cloth electrodes in a PDMS frame. Therapeutic agents are pre-loaded into one of the hydrogel cells during fabrication. Owing to its soft mechanical property and biocompatibility, hydrogel has been widely adopted as the delivery media for iontophoresis. Along with soft PDMS as the main substrate, the whole device could conformably attach to the skin and enable drug release imperceptibly with minimal discomfort.

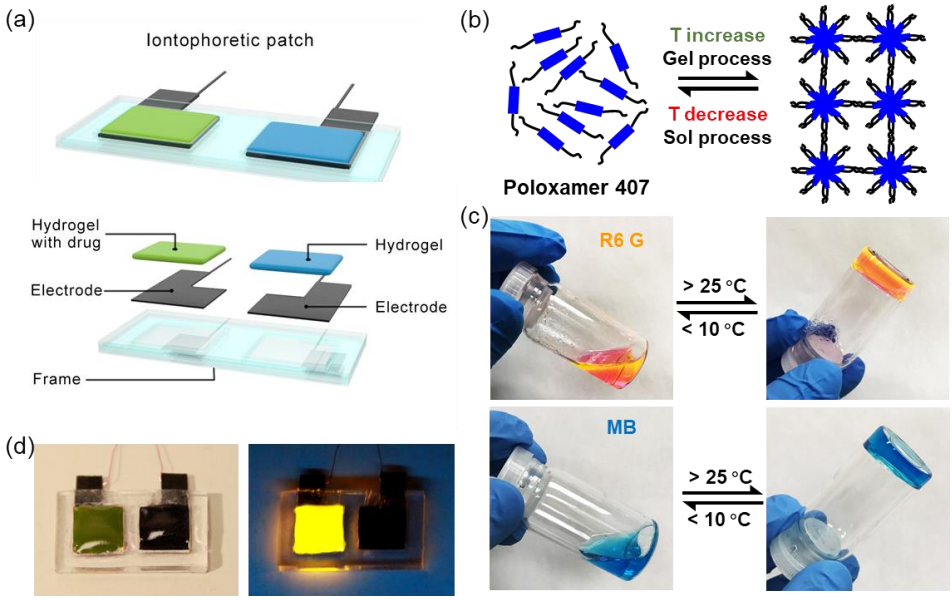


**Figure 30. Hydrogel-based soft patch for TDD.** (a) Schematic of the device structure. (b) Schematic of gelation and solution process of hydrogel. (c) Photographs of hydrogel loaded with different dyes. (d) Photographs of fabricated device with R6G as simulated drug under normal ambient light and UV light.

Poloxamer 407-based hydrogel, which is thermosensitive and has been approved by the FDA, was used in this study. Because of hydrophobic interactions between the copolymer chains, poloxamer 407 aqueous solutions (20-30 wt%) exhibit reversible thermogelation property, which can be characterized by the concentration-dependent sol-gel transition temperature ($T_{sol\text{-}gel}$).[153] The solutions switch between fluid and semi-solid states when the temperature changes near the $T_{sol\text{-}gel}$, as illustrated in Figure 30b. This reversible sol-gel property gives poloxamer 407 hydrogel many advantages in transdermal drug delivery applications, such as easy drug loading, good contact with skin, easy removal from the skin, and good electrical conductivity. Figure 30c presents the images of poloxamer 407 solutions loaded with R6G (60 μmol·$L^{-1}$) and MB (60 μmol·$L^{-1}$), which clearly show their transition between fluid and semi-solid states as the temperature changes. The dye-loading and plain poloxamer 407 solutions were dispensed into the two

cells of the PDMS frame on top of the carbon-cloth electrodes at a low temperature, followed by thermogelation at 37 °C. The optical and fluorescent images of the fabricated iontophoretic drug patch with R6G as the simulated drug are presented in Figure 30d. Both the dark green (product of black from electrode and orange from R6G) color region in the optical image and the bright yellow region in the fluorescent image under an UV (365 nm) lamp clearly indicate the uniform existence of R6G in the left hydrogel cell.

### *3.2.4 Wearable Insole TENG for TDD*

Wearable TENG, which can take various forms including textile,[134, 154, 155] insole,[70, 156, 157] wristband,[145] e-skin[132] etc. (Figure 31a), offers a promising solution for self-powered wearable systems by converting biomechanical energy into electrical energy. In this work, a wearable insole TENG was fabricated for the proof-of-concept demonstration. As illustrated in Figure 31b, the insole TENG used PTFE as one triboelectric material, Al as the other triboelectric material and electrodes, PET as the substrate, and Kapton as the spacer. When the foot steps onto it, the PTFE and Al will come into contact and opposite charges will be induced on their surfaces. These induced charges will drive current to flow between the Al electrodes through external circuit when the gap distance between PTFE and Al changes. Multiple units can be integrated together as in Figure 31b to enhance the electrical outputs, and a device with 3 units was used for our experiments.

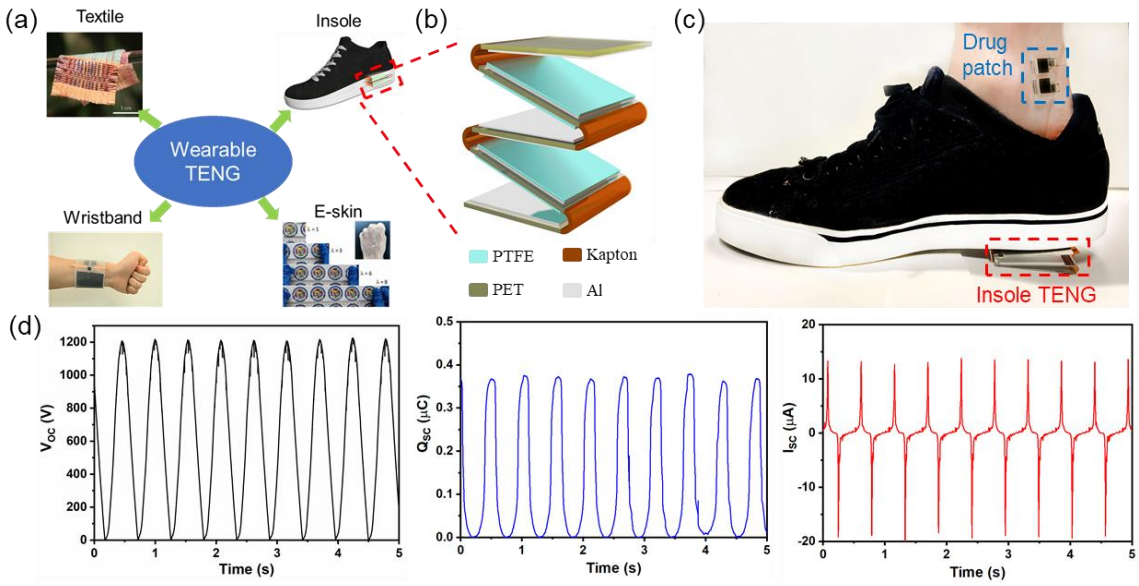


**Figure 31. Wearable TENG for harvesting biomechanical energy to drive electrically-assisted TDD.** (a) Examples of wearable TENG. Reproduced with permission [134]. Copyright 2016, Springer Nature. Reproduced with permission [145]. Copyright 2018, Elsevier. Reproduced under the terms of the CC-BY-NC 4.0 license [132]. Copyright 2017, The American Association for the Advancement of Science. (b) Schematic of the insole TENG used in this study. (c) Photograph of a wearable TDD system on human ankle consisting of the insole TENG and designed drug patch. (d) Electrical outputs of the insole TENG under open-circuit and short-circuit conditions.

Along with the wearable hydrogel-based drug patch, such a TENG device can be readily deployed onto human body to make a self-powered electrically-assisted TDD system. The electrode on the drug-containing hydrogel is connected to the positive terminal of a rectifier that converts the AC output of TENG into direct current (DC) current, while the other electrode is connected to the negative terminal to form a complete circuit. As a result, the TENG output, which is stimulated by body motions, can be used to accelerate the transdermal drug release rate via iontophoresis without external power sources. Figure 31c demonstrates the concept of a pain-relief TDD system for ankle injury, with the drug patch on the ankle and an insole TENG under the shoe. The drug can be administered on-demand when the patient walks on his foot and generates electricity at the same time. The

typical electrical outputs of the insole TENG consisting of 3 units connected in parallel under open-circuit and short-circuit conditions were plotted in Figure 31d. Its open-circuit voltage reached about 1200 V, short-circuit charge transfer was about 370 nC per cycle, and maximum short-circuit current was nearly 20 μA at an operation frequency of 2 Hz.

### *3.2.5 Performance of TENG-driven Iontophoretic TDD System*

To better evaluate the performance of the TENG-driven iontophoretic TDD system, it was applied to a pigskin with R6G as the simulated drug loaded in one hydrogel cell (Figure 32a). The drug patch was connected to the TENG via a rectifier, with the electrode on the dye-loading cell wired to the positive terminal and the other electrode to the negative terminal. The insole TENG was operated using a linear motor at a frequency of 2 Hz to mimic human walking behavior, and the drug patch was placed in a 37 °C oven during the drug delivery experiment. The electrical outputs of the TENG under such a load condition (drug patch and pigskin) were measured, with its *V*-*Q* plot shown in Figure 32b. About 320 nC amount of charge was transferred per operation cycle and an AC output voltage with an amplitude of 4 V was achieved. After the rectifier, a DC current with a maximum of around 12 μA was delivered to the designed hydrogel device (Figure 32c).

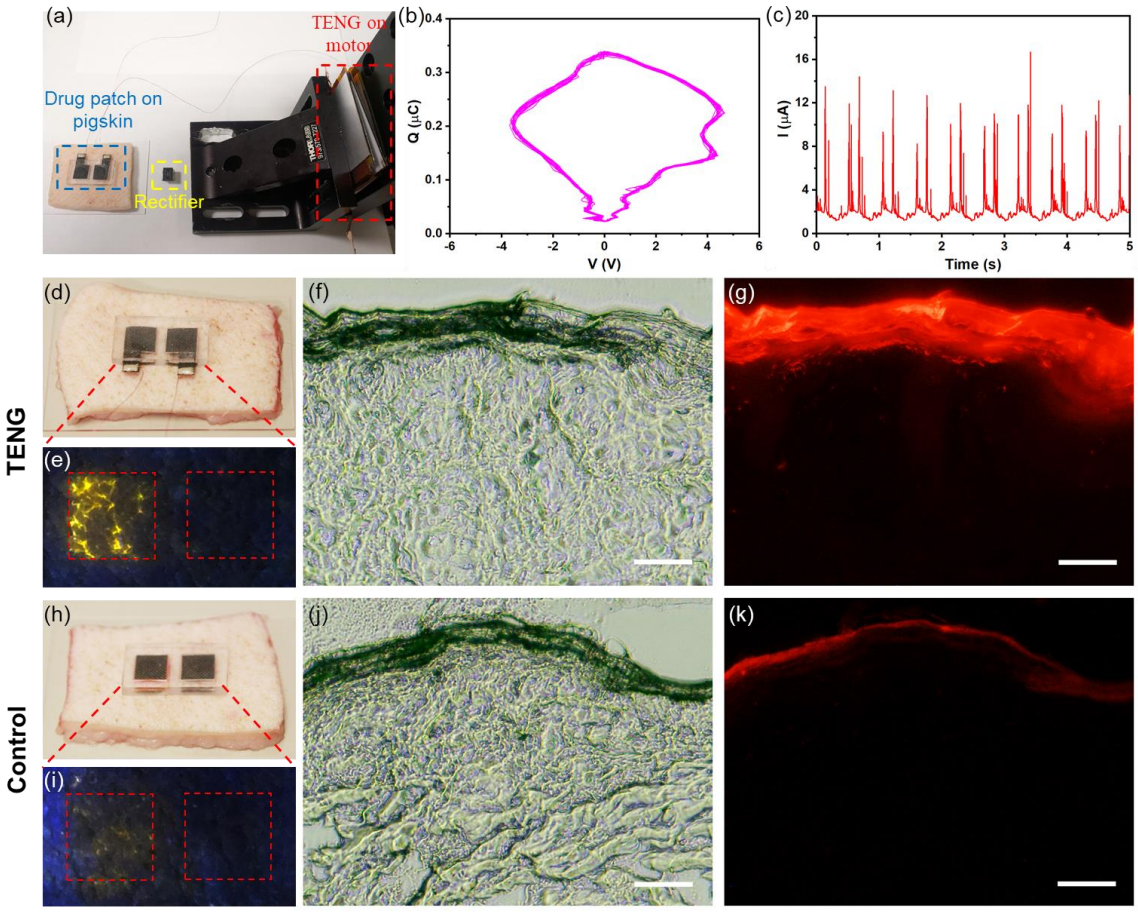


**Figure 32. Proof-of-concept demonstration of self-powered TDD system on pigskin.** (a) Photograph of experimental setup with motion simulated by a linear motor. (b) *V*-*Q* plot of the corresponding TENG output. (c) Rectified current that passed through the designed hydrogel device and pigskin. (d, h) Photograph of the R6G-containing hydrogel drug patch on a pigskin with (d) and without (h) TENG connection. (e, i) Fluorescent images, (f, j) the bright field cross-section images and (g, k) fluorescent cross-sections images of the pigskin after 6 hours patch with (e-g) and without (i-k) TENG connection. Scale bar, 100 μm.

The drug patch stayed on the pigskin with the TENG in continuous operation for 6 hours before examination (Figure 32d), and control experiment was performed under identical conditions except that the TENG was not connected. The fluorescent images under the 365 nm UV lamp (Figure 32e and Figure 32i) showed that the fluorescence of the pigskin from the TENG-driven experiment was much stronger, and the emission of fluorescence from the inside, rather than the surface, of the pigskin suggested that the R6G dye was

successfully delivered to the inner tissue with the assist of TENG. Cross-sectional images were then taken to further compare the results. The distinct contrast between the fluorescent cross-sectional images (Figure 32g and Figure 32k) presented strong evidence that more R6G was released into the pigskin from the TENG-driven experiment and the R6G was delivered to the deeper tissue with TENG. Therefore, the results here successfully proved the feasibility of the proposed self-powered iontophoretic TDD system driven by biomechanical motions, through the integration of a wearable TENG and an electrically-assisted drug patch. It is worth mentioning that this system can achieve TDD in a non-invasive manner, as opposed to the systems previously reported.

In summary, a self-powered, non-invasive TDD system consisting of a wearable TENG and an iontophoretic patch has been proposed. The emerging TENG technology offers a facile and cost-effective solution for wearable energy harvesters that can detect body motions and convert associated biomechanical energy into electricity simultaneously, while the rationally designed hydrogel-based drug patch enables TDD in a non-invasive and imperceptible manner. The feasibility of the proposed system was successfully demonstrated on pigskins using dyes as the simulated drugs, with both bright-field and fluorescent images indicating that the TENG outputs assisted the drug release process. Depending on the application scenario where the triggering motion of TENG is either involutory or intentional, furthermore, both sustained drug release and intentional release with feedback control can be achieved. This work provides a promising solution for non-invasive, electrically-assisted TDD with closed-loop sensation and therapy, and promotes TENG-based self-powered systems towards advanced biomedical treatment in the era of IoT.

### *3.2.6 Experimental Methods*

#### 3.2.6.1 Fabrication of TENG

Two different TENGs were fabricated in this work. 1) A spring-based contact-separation TENG for the study of electrophoretic flow in Figure 29. Two acrylic plates (15 cm wide × 15 cm long × 1/8 inch thick) were used as the substrates. A PTFE film (10 cm wide × 10 cm long × 50 μm thick) and an Al film (10 cm wide × 10 cm long × 100 μm thick) were pasted on one acrylic plate, and an Al film (10 cm wide × 10 cm long × 100 μm thick) on the other plate. Four springs were fixed at the four corners of the acrylic plates using epoxy glue to work as the spacer. The TENG was operated using an electrodynamic shaker at different frequencies. 2) A wearable insole TENG for TDD experiments. It used PTFE as one triboelectric material, Al as the other triboelectric material and electrodes, PET as the substrate, and Kapton as the spacer. 3 units was integrated together like the schematic in Figure 31 (where 4 units are illustrated) and electrically connected in parallel. The TENG was operated using a linear motor.

#### 3.2.6.2 Electrical Measurements

Electrical measurements were conducted using the Keithley 6514 Electrometer. The electrical circuit model for measuring the *V*-*Q* plot and rectified current in Figure 32 is drawn in Figure 33.

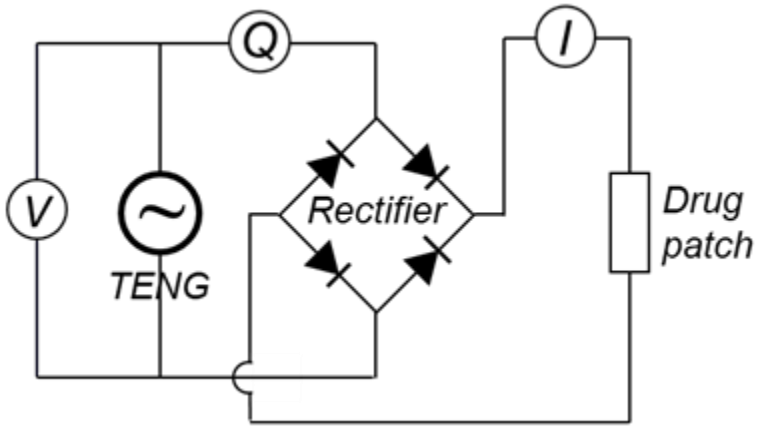


**Figure 33. The electrical circuit model for measuring the *V*-*Q* plot of TENG output and rectified current (*I*) delivered to the drug patch in the pigskin experiment.**

3.2.6.3 Preparation of Hydrogel Solutions

Briefly, a certain amount of poloxamer 407 powder was added to deionized water in an ice bath with the final poloxamer 407 concentration at 25 wt% under continuous magnetic stirring. The solution was then refrigerated until poloxamer 407 was completely dissolved and a clear solution was obtained. For dye-loading solutions, the R6G (or MB) aqueous solution was added to the poloxamer 407 solution with the final R6G (or MB) concentration at 60 $\mu mol \cdot L^{-1}$

3.2.6.4 Fabrication of Hydrogel-Based Iontophoretic Drug Patch

The detailed fabrication process is illustrated in Figure 34. An acrylic mold was firstly fabricated. Sylgard 184, with a weight ratio of 10:1 for Part A and Part B, was casted into the acrylic mold and cured at 50 °C for 24 hours to produce the PDMS frame. The PDMS frame had two side-by-side cells with the dimension of 10 mm wide × 10 mm long × 1.5 mm deep. The dye-loading poloxamer 407 solution was poured into one cell and

plain poloxamer 407 solution into the other. Finally, the patch was placed in a 37 °C oven for the thermal gelation.

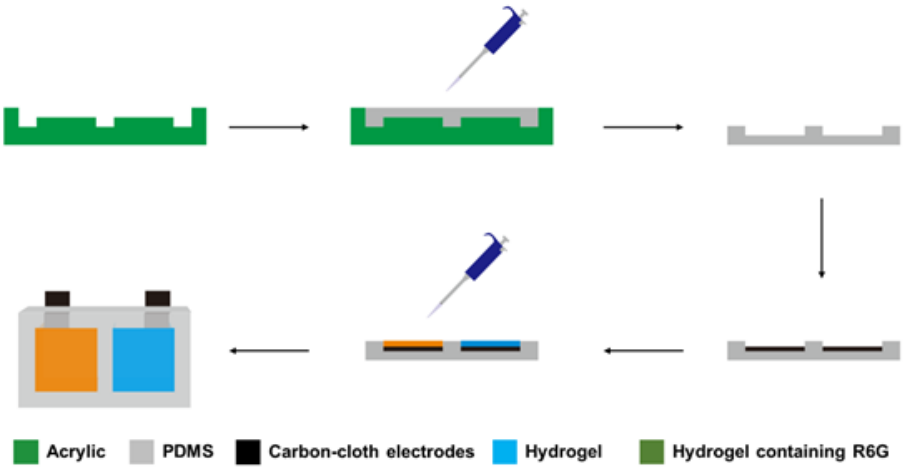


**Figure 34. Fabrication process of the hydrogel-based iontophoretic drug patch.**

3.2.6.5 Performance Evaluation of TENG-Driven Drug Patch on Pigskin

The drug patch fabricated above was placed on the pigskin with the TENG in continuous operation for 6 hours, and control experiment was performed under identical conditions except that the TENG was not connected. The skins were then embedded in optimal-cutting-temperature compound (OCT), frozen in -80 °C for 15 minutes and sliced into 10 μm sections. Slides were then visualized and photographed using a standard fluorescence microscopy (Olympus IX70).

## 3.3 Wearable Self-Charging Power Unit by Integrating MXene Electrochemical Microsupercapacitor with TENG

The development of miniaturized, wearable, and implantable electronics has increased the demand for small stand-alone power modules that have steady output and

long life-time. Given the limited capacity of energy storage devices, one promising solution is to integrate energy harvesting and storage materials to efficiently convert ambient mechanical energy to electricity for direct use or to store the harvested energy by electrochemical means. Different methods to integrate TENG with supercapacitors have been proposed, however, most of these methods suffer from drawbacks.[156, 158, 159] For example, TENG working in contact-separation mode usually need a spacer, which makes it difficult to fabricate integrated and compact devices. One the other hand, the liquid electrolyte in conventional supercapacitors will evaporate if exposed to air, thus proper encapsulation of the supercapacitor is required, which makes the TENG-supercapacitor device bulky. Furthermore, the TENG and supercapacitors are usually made as two separate parts, so external wiring for electrical connection is needed, which adds extra volume to the system.

Here, we propose a simple technique to fabricate a flexible self-charging power unit, which integrates a single-electrode-mode TENG device with 2D MXene-based solid-state microsupercapacitor (MSC) into a single monolithic device with silicone rubber as encapsulation material. Our device could simultaneously and effectively convert and store mechanical energy of human biomechanical motions into electrochemical energy. In addition, our device can have a long lifetime for continuous energy harvesting and storage, which can be useful for powering electronics without additional power sources.

### *3.3.1 Design of Wearable Self-Charging Power Unit*

Figure 35a displays the schematic illustration of the detailed device structure. Three main components (current collector for TENG, rectifier and microsupercapacitor) were

sealed compactly by silicone rubber, while silicone rubber itself serves as both the encapsulating material and stretchable dielectric. Our energy storage device is completely sealed inside the silicone, such that no leakage or evaporation of the electrolyte takes place, thus extending life time for the MSC. As shown in Figure 35b, the capacitor can be charged by the regulated current from TENG, which produces electricity when the human skin makes contact with the device. Also, since silicone is a very common material for prosthetic skin, it is biocompatible and provides a comfortable feeling when worn on hand (Figure 35c). Moreover, the mechanical property of the silicone enables the high flexibility of the device as it can undergo different deformations such as fold, twist and stretch (Figure 35(d-f)). Even the silicone rubber tears, solid nature of the electrolytes are not expected to harmfully affect the human body.

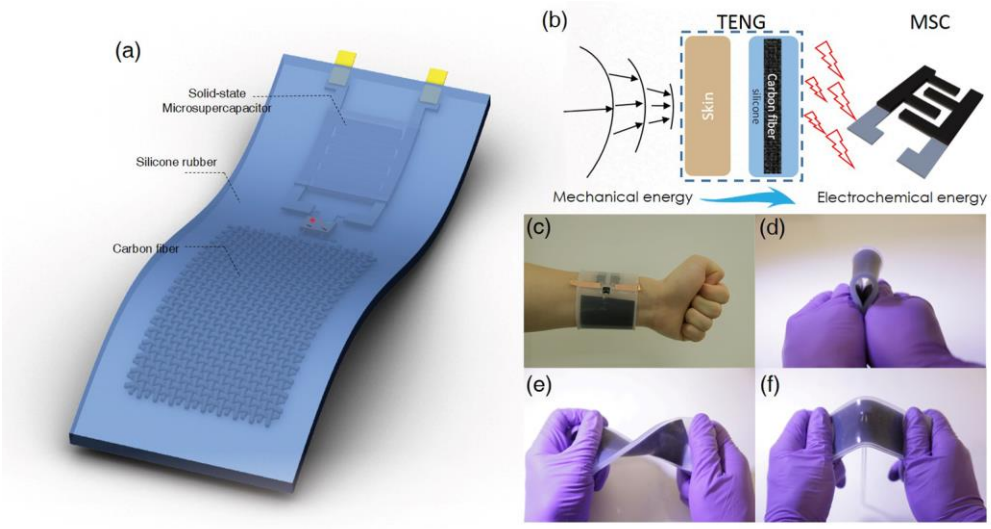


**Figure 35. Wearable self-charging power unit.** (a) Schematic diagram of the whole device. (b) Schematic illustration of mechanism for generating electricity to power the supercapacitor. (c) Photograph demonstrating that the integrated system worn on the forearm. Photographs of as-prepared device with demonstrations of being different mechanical deformations including fold(d), twist(e) and stretch (f). Reproduced with permission.[145] Copyright 2018, Elsevier.

### *3.3.2 MXene Based Electrochemical Microsupercapacitor*

Recently, MXene-based MSCs fabricated by employing a Meyer coating and spray-coating methods followed by a direct laser cutting process were reported.[160, 161] However, MXene tends to be easily oxidized at high temperatures, and laser engraving was shown to easily oxidize the edge of the interdigitated MXene fingers. To solve this problem, we have proposed a simple one-step method to make the MSC by pre-patterning the substrate. The schematic in Figure 36a shows the details of this process. We first used a $CO_2$ laser to smoothly cut the PET substrate into the desired pattern, then used direct spray-coating of MXene on the pattern to form the active material pattern; which was followed by painting of the cross-linked gel electrolyte over the entire device to complete the solid-state MSC fabrication. Raman spectroscopy and XRD were used to characterize the active MXene material $Ti_3C_2T_x$. As shown in Figure 36b, The Raman spectrum of $Ti_3C_2T_x$ exhibits strong peaks at 200 and 722 $cm^{-1}$, which can be assigned to the A1g modes of $Ti_3C_2O_2$; the additional peaks at 286, and 630 $cm^{-1}$ can be assigned to the following vibrational modes: $E_g$ of $Ti_3C_2(OH)_2$, and $E_g$ of $Ti_3C_2F_2$, respectively.[162] These peaks reveal the presence of -OH, -O and -F functional groups on $Ti_3C_2T_x$ MXene surface. As compared with PET substrate, $Ti_3C_2T_x$ on PET shows strong (002) XRD peak located at $2\theta = 7.2°$ with FWHM = 0.55°, with corresponding to a d-spacing of 1.2 nm (Figure 36c). The SEM image in Figure 36d shows that $Ti_3C_2T_x$ electrodes have been uniformly coated on the substrate, which is confirmed in the cross-section SEM image (Figure 36e).

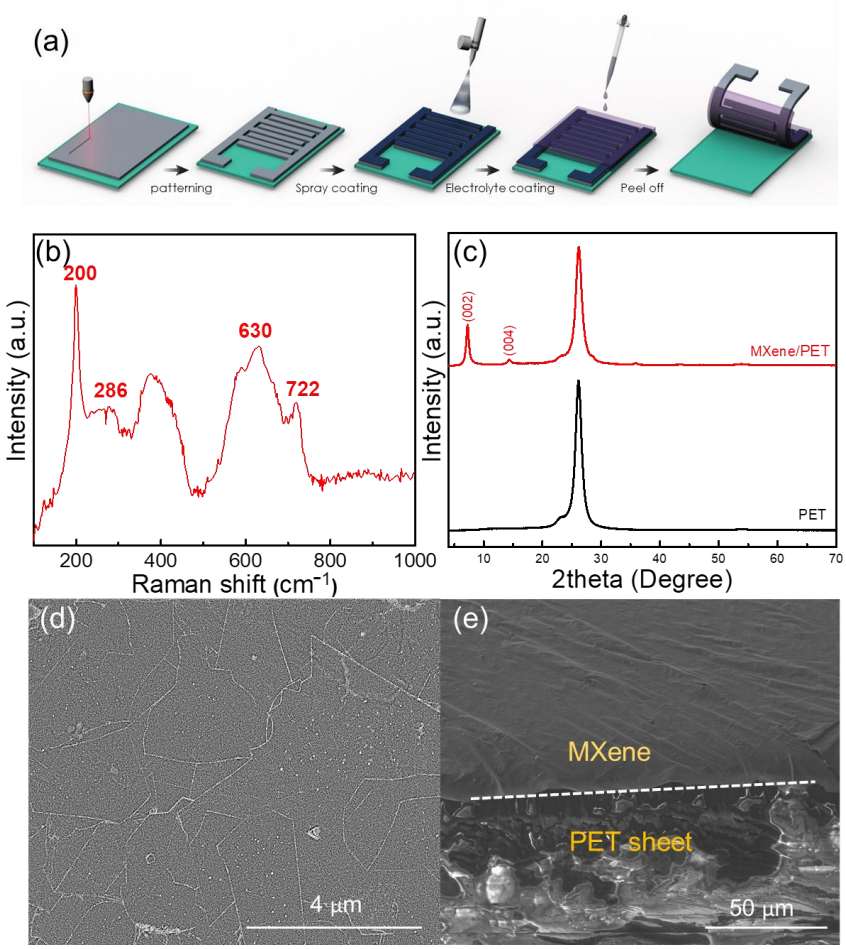


**Figure 36. Fabrication and characterization of MXene based MSC.** (a) Schematic illustrating fabrication protocols of $Ti_3C_2T_x$ microsupercapacitors. (b) Typical Raman spectra of $Ti_3C_2T_x$ on PET. (c) XRD patterns of $Ti_3C_2T_x$. Field emission scanning electron microscopy (FESEM) images of plane view (d) and cross-section (e) of $Ti_3C_2T_x$. Reproduced with permission.[145] Copyright 2018, Elsevier.

Electrochemical performance of $Ti_3C_2T_x$ MXene-based MSC devices was studied by employing polyvinyl alcohol (PVA)/$H_3PO_4$ gel electrolyte in the two-electrode configuration. The hydrogel electrolyte was produced by incorporating glutaraldehyde (GA) as a crosslinking reagent to form a three dimensional network connections with multiple junction zones. The chemically cross-linked polyvinyl alcohol PVA/$H_3PO_4$ hydrogel not only serves as the solid-state electrolyte, but also guarantees the structural integrity and mechanical strength of the assembled device.[163] The chemically cross-linked

hydrogel shows excellent elasticity and high ionic conductivity due to a larger water content absorbed in the polymer matrix that helps in fine-tuning ionic conductivity. In addition, it slows down self-discharge of the microsupercapacitors. The cyclic voltammetry (CV) of our MSC devices are shown in Figure 37a, where symmetric and rectangular curves are observed in the potential window of 0.6V, indicating good capacitive performance. As shown in Figure 37b, the galvanostatic charge-discharge (CD) profiles obtained at different current densities (0.3-1 $mA/cm^2$) are quite linear in the potential window of 0-0.6 V. Moreover, the IR-drop of the devices was found to be only 0.07 V at a current density of 1 $mA/cm^2$. Since no current collectors were used in making these devices, these results show that the MXene electrodes have low intrinsic resistance (5000 S/cm by four point probe). The calculated areal capacitance based on the discharge curve is shown in Figure 37c. Our devices show an energy density of 2.8 $mWh/cm^3$ at a power density of 225 $mW/cm^3$, and an energy density of 2.3 $mWh/cm^3$ at a power density of 744 $mW/cm^3$, which is superior to other state-of-the-art microsupercapacitors (Figure 37d).[164-167] This solid-state MSC exhibits good cycling stability with a capacitance retention up to 76% and coulombic efficiency of 95% over 10k cycles as shown in Figure 37e. The self-discharge behavior of the supercapacitor is an important parameter for practical applications, especially when charging at low current. We investigated the self-discharge behavior of our devices via measuring the open circuit potential of the device after thoroughly charging it, and a slow self-discharge rate of 0.1 V/h was observed for the device, which is shown in Figure 37f. Since the device was fabricated on flexible substrates, it can be repeatedly bent at various angles and frequencies (Figure 37g) without compromising performance. For real applications, energy storage units are usually

packaged in series to supply sufficient voltage. Thus, tandem devices connected in series were examined. The voltage window increases to 2.4 V at the expense of the decreased capacitance. As shown in Figure 37h, the CV curves exhibit rectangular shapes even when the voltage window is extended, which is consistent with the nearly ideal triangular CD curves shown in Figure 37i.

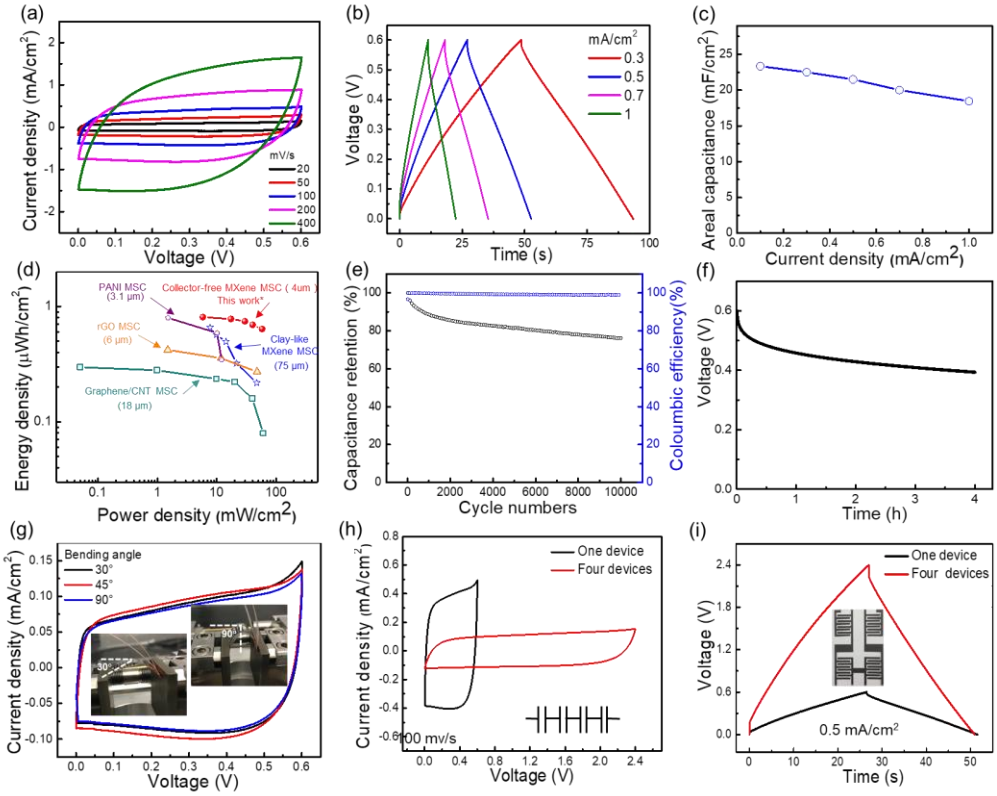


**Figure 37. Electrochemical performance of $Ti_3C_2T_x$ MSC with PVA/$H_2SO_4$ gel electrolyte.** (a) CV curves at different scan rates. (b) CD profiles at different current densities. (c) Areal capacitances at different current densities. (d) Ragone plot showing showing gravimetric energy and power densities. (e) Cycling stability and Coulombic efficiency of $Ti_3C_2T_x$ MSC over 10k cycles at a current density of 1 mA/cm$^2$. (g) Self-discharge measurement. (g) CV curves for the bent MXene MSC employing gel electrolyte at a scan rate of 50 mV/s, inset shows the digital photographs for the bent configuration of MSC. (h) CV curves at scan rate of 100 mV/s and (i) CD curves at current of 0.4 mA for the integrated tandem supercapacitors. Reproduced with permission.[145] Copyright 2018, Elsevier.

### *3.3.3 Wearable TENG Based on Carbon-Fiber-Embedded Silicone*

A single-electrode-mode TENG based on carbon-fiber-embedded silicone was designed for integration with the silicone-encapsulated MXene-based MSC. The use of carbon fiber electrode is more cost-effective than previously reported devices based on Ag NWs;[147, 168] in addition, carbon fiber retains the advantages of flexibility, ease of fabrication and durability. The adoption of the single-electrode mode eliminates the need of spacer in the contact-separation mode and greatly facilitates the integration of the TENG and MSC in a sealed thin-film manner. The detailed working principle of the TENG device is illustrated in Figure 38(a-d). Firstly, positive and negative charges are induced on the surfaces of human skin and silicone respectively when they are in contact. Once the positively charged skin leaves the TENG device, the potential of the carbon fiber embedded beneath the negatively charged silicone will decrease in reference to the ground potential, and thus a potential difference will be generated across the two inputs of the bridge rectifier and electrons will flow out from the carbon fiber to charge the supercapacitor. The process continues until the skin reaches the maximum separation distance. In contrast, as the skin re-approaches the TENG, the potential on the carbon fiber will increase and the electrons will flow back to the carbon fiber, which will also charge the supercapacitor through the bridge rectifier. The entire process reverts to the initial state once the skin touches the TENG again. The performance of the TENG was fully characterized under different load conditions and the results are plotted in Figure 38(e-g). Under the short-circuit condition, the maximum charge transferred per cycle reached about 4.2 $nC/cm^2$, and the peak current was about 0.13 $\mu A/cm^2$ at the working frequency of 1.3 Hz. Meanwhile, the open-circuit voltage was nearly 50 V for a device with an active area of 4 $cm^2$. The output power of the

TENG connected with various external load resistance was measured and plotted in Figure 38h, with the maximum output power of 7.8 μW/cm$^2$ at a load resistance of 400 MΩ.

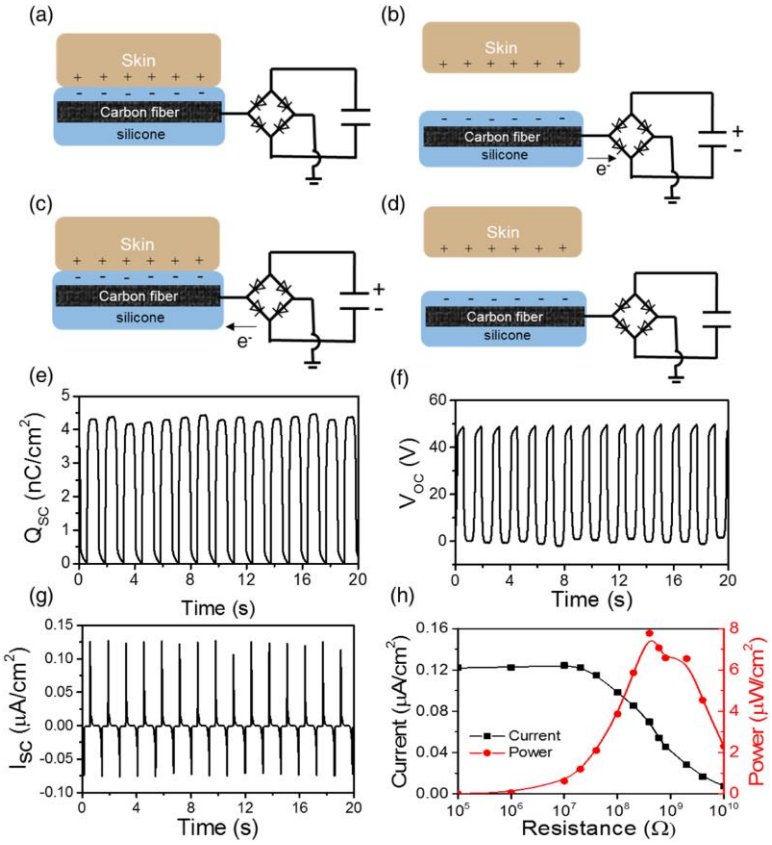


**Figure 38. Wearable TENG based on carbon-fiber-embedded Silicone.** (a-d) Working mechanism of the TENG. (e) $Q_{SC}$, (f) $V_{OC}$, and (g) $J_{SC}$ of the triboelectric nanogenerator. (h) Relationship between instantaneous power density and resistance of the external load. Reproduced with permission.[145] Copyright 2018, Elsevier.

### *3.3.4 Demonstrations using Self-Charging Power Band*

Several demonstrations of the self-charging power band were conducted to show its possible application scenarios, with the generic equivalent electrical circuit drawn in Figure 39a. The power band consists of a TENG as an AC power source, a bridge rectifier as an AC-to-DC converter, and a supercapacitor as an energy storage device. The external load can be connected in parallel to the supercapacitor via a switch. Figure 39b illustrates

the self-charging capability of the power band (one capacitor connected) under hand clapping (the clapping frequency is estimated to be 5Hz) when no external load was connected. The overall charging curve can be divided into 5 regions: a-b, clapping; b-c: resting; c-d: clapping; d-e: resting; e-f: clapping. It takes roughly 30 mins to fully charge the supercapacitor when continuously clapping without large current leakage. Corresponding current response of the MSC charged at 5 Hz is shown in Figure 39d where stable current with small fluctuations can be observed at the charging regions. Other body movement such as walking or hand shaking may also be used to charge the nanogenerator. In applications such as wearable sensors where only few readings per day are needed for a few seconds, this energy harvesting rate may be sufficient. The flexible power band can be used as an ideal watch strap which powers the watch (four fully charged MSCs connected in series) at the same time, as shown in Figure 39e. It can also power up a thermos-humidity meter as in Figure 39f, which makes it suitable for both indoor and outdoor activities.

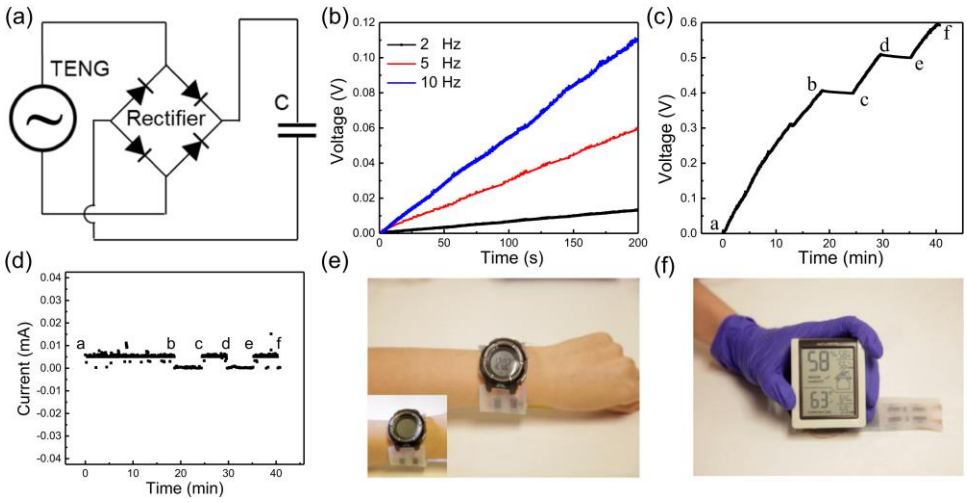


**Figure 39. Demonstration using self-charging power band.** (a) Circuit diagram of the energy supply mode. (b) Charging Curve of the microsupercapacitor charged by TENG at various frequencies. (c) Charging curve showing the voltage increase of a single capacitor powered by TENG, corresponding current response is shown in (d). Digital photos showing

MSC to drive (e) A electronic watch and (f) commercial temperature-humidity meter. Reproduced with permission.[145] Copyright 2018, Elsevier.

In summary, we have developed a self-charging power unit by integrating, for the first time, MXene-based MSCs with a soft and flexible triboelectric nanogenerator, using skin as contact. The power system can be continuously charged by regular human motion (~5 Hz) without significant current leakage. We have also shown the functionality of the system by powering various electronic devices and sensors. Our strategy shows that TENG is versatile and can be integrated with energy storage devices, which opens new possibilities in wearable/implantable sensor networks.

### *3.3.5 Experimental Methods*

#### 3.3.5.1 Synthesis of Delaminated $Ti_3C_2T_x$ MXene

All chemicals were used as received without further purification. Layered ternary carbide $Ti_3AlC_2$ (MAX phase) powder were commercially procured (Carbon-Ukraine ltd. particle size < 40 μm). $Ti_3C_2T_x$ MXene was synthesized following minimal intensive layer delamination MILD method by selective etching of Al from $Ti_3AlC_2$ using *in situ* HF-forming etchant as previously as reported in very detail elsewhere.[169] The etching solution was prepared by adding 1 g lithium fluoride (LiF, Alfa Aesar, 98+ %) to 20 ml 9 M hydrochloric acid (HCl, Fisher, technical grade, 35-38%), followed by stirring for 5 min. 1 g of $Ti_3AlC_2$ powder was slowly added to the MILD etchant at 35 °C and stirred for 24 h. The acidic suspension was washed with deionized (DI) water until pH ≥ 6 via centrifugation at 3500 revolutions per minute (RPM) (5 min per cycle) and decanting the supernatant after each cycle. Around pH ⩾6, stable dark green supernatant of $Ti_3C_2T_x$ was

observed and then collected after 30 min centrifugation at 3500 RPM. The concentration of $Ti_3C_2T_x$ solution was measured by filtering specific amounts of colloidal solution through a polypropylene filter (3501 Coated PP, Celgard LLC, Charlotte, NC), followed by drying under vacuum at 70 °C overnight.

#### 3.3.5.2 Preparation of MXene Microsupercapacitor

PET sheets were cleaned with a soap solution to remove surface contamination followed by ultrasonication in isopropanol and DI water sequentially for 5 min each and then dried by blowing nitrogen ($N_2$) gas. PET patterns were produced by utilizing direct laser machining using a $CO_2$ Universal Laser cutter System (model: Professional laser system PLS 6.75, wavelength of 10.6 µm). The laser power and speed were set to 5% and 30%, respectively. The z-distance between the laser and the sample was 2 cm. AutoCAD technical drawing software was used to design the interdigital finger electrodes at each length of 8 mm, width of 1 mm, and spacing of 1 mm. The laser beam size was 100 µm. All of the laser experiments were performed under ambient conditions. MXene symmetric MSCs were fabricated by one-step spray-coating of a 4 µm $Ti_3C_2T_x$ film directly onto the PET patterns as the active material. This spray-coated MXene electrode pattern was directly used for fabrication of collector-free microsupercapacitor device by casting the gel electrolyte.

#### 3.3.5.3 Preparation of Gel Electrolyte

The PVA/$H_3PO_4$ gel electrolyte was prepared as follows: 1 g of PVA ($M_w$ = 89000-98000, Sigma-Aldrich) was weighed and added into an RB flask containing 10 ml deionised water. The mixture was subsequently heated at 80 °C with constant stirring until

a clear solution was obtained. The solution was then cooled to room temperature and then 0.8 g phosphoric acid ($H_3PO_4$) was added. It was then stirred for 2h. After that, the gel was kept in vacuum oven at room temperature for 2 hours to remove the extra bubbles in the solution. Before using, the cross-linked gel was made by mixing the as-prepared gel with diluted glutaraldehyde (mass ratio of PVA and glutaraldehyde is 100:1), the whole mixture should be used immediately before it was fully cured.

#### 3.3.5.4 Integrating TENG with Microsupercapacitor

Acrylic mold was pre-cleaned with ethanol and water, followed by a thin layer of handsoap. Super-soft silicone rubber (Smooth-On, Ecoflex 00-10) was prepared by mixing the two components in a 1:1 volumn ratio. The silicone rubber mixture was then casted onto the the acrylic plate to form the first layer of silicone. Microupercapacitor device, rectifier (DF02M, digi-key electronics) and carbon cloth ($4 \times 6\ cm^2 \times 350\ \mu m$, conductivity 0.1 $m\Omega cm^2$, Fuel Cell store) were placed and aligned on top of the silicone after the bottom silicone had lost its fluidity. Then, another layer of liquid silicone was poured onto the top of them to enclose the whole device.

#### 3.3.5.5 Electrochemical Measurements

The electrochemical tests (CV, CD, electrochemical cycling stability) were conducted at room temperature using a VMP3 electrochemical workstation (Bio-Logic, France). The electrochemical impedance spectroscopy (EIS) was measured using a Modulab (Solartron Analytical) electrochemical workstation in the frequency range from 100 kHz to 0.01 mHz at open circuit potential by applying a small sinusoidal potential of 10 mV signal. All measurements were done at room temperature.

3.3.5.6 Material Characterization

X-ray diffraction (XRD) patterns were collected by a Bruker diffractometer (D8 Advance) with Cu K$\alpha$ radiation, $\lambda$ = 1.5406 Å. The morphology and microstructure of the samples were characterized by a scanning electron microscope (SEM) (Nova Nano 630, FEI) Raman measurements were carried out on the samples using a micro-Raman spectrometer (LabRAM ARAMIS, Horibat-Jobin Yvon) with notch filters cutting at 100 $cm^{-1}$ using a Cobalt laser (633 nm, 5 mW at source). D2 filter (correpsonding laser power, 10%) was used to prevent laser induced oxidation during the measurements.

# CHAPTER 4. APPLICATION OF TENG FOR ACTIVE SENSING

## 4.1 Recent Progress of TENG as Active Sensors

Owing to its ability of transforming mechanical stimuli to electrical signals directly without additional transducers, TENG has great potential in the field of active sensing and self-powered sensors. Successful demonstrations include tactile touch sensors,[33-35] acoustic sensors,[31, 32, 36, 37] motion and acceleration sensors,[38-40] and chemical sensors.[41-44] Meanwhile, TENG also offers power-efficient and cost-effective solutions for advanced HMI in the era of IoT.[47, 48]

A representative TENG-based touch sensor is shown in Figure 40a.[35] The thin-film-based triboelectric sensor (TES) had a multi-layered sandwich structure, with nylon as the bottom substrate, indium tin oxide (ITO) as electrodes, PET as the dielectric between two electrodes, and FEP as the electrification layer that generates triboelectric charges upon contact with a foreign object. As the foreign object separated with the TES, a voltage signal would be generated across the two electrodes due to the change in electric potential, without the need of an external power supply. By integrating the TES with a signal-processing circuit, the signals generated from finger touching or foot pressing could be used to trigger functional electronics such as a light or a wireless alarm. The first TENG-based chemical sensor was developed by Lin et al. for mercury ion detection (Figure 40b).[41] The self-powered sensor was made of a contact-separation TENG, which used 3-mercaptopropionic-acid modified Au nanoparticles as the electrical performance enhancer and recognition element. The electrical output of triboelectric chemical sensor is highly sensitive and selective to mercury ions, and owing to the power generation capability of

the TENG, a commercial LED lamp rather than expensive electrometers can be used as an indicator.

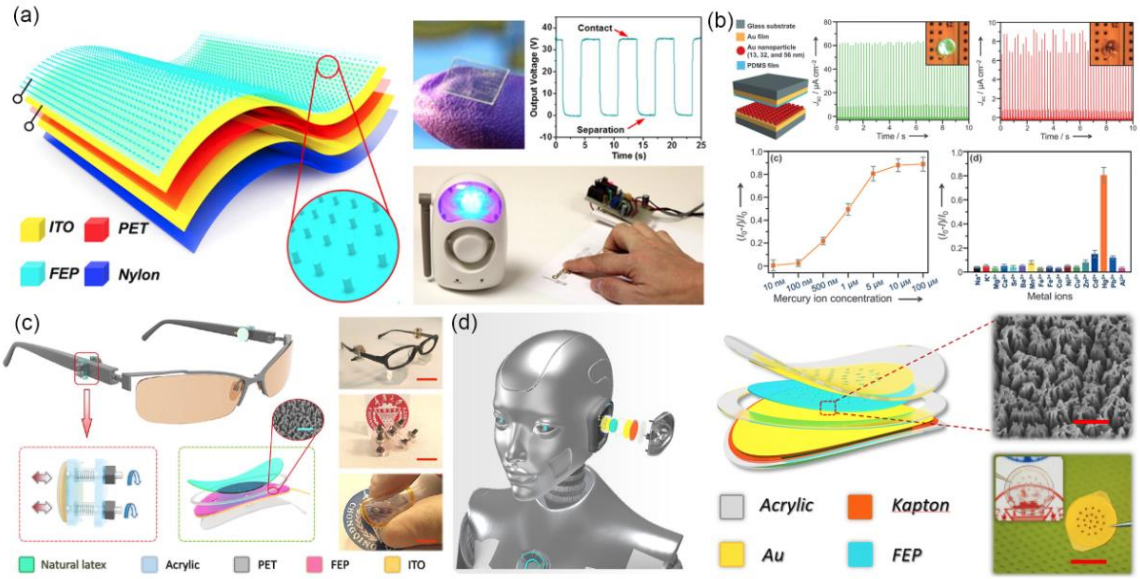


**Figure 40. Application of TENG as active sensors.** (a) Flexible tactile sensor based on contact electrification. Reproduced with permission.[35] Copyright 2014, American Chemical Society. (b) Self-powered triboelectric nanosensor for mercury ion detection. Reproduced with permission. Copyright 2013, Wiley-VCH. (c) Eye motion triggered mechanosensational communication system based on TENG. Reproduced under the terms of the CC-BY-NC 4.0 license.[47] Copyright 2017, The American Association for the Advancement of Science. (d) A triboelectric auditory sensor for social robots and hearing aids. Reproduced with permission.[48] Copyright 2018, The American Association for the Advancement of Science.

TENG-based active sensors can also be used in novel HMI and transform the way people interact with machines. One example is a hands-free HMI that translates real-time micromotions of eye blinking into control commands.[47] The structures and images of the proposed mechanosensational TENG (msTENG) are presented in Figure 40c. The single-electrode-mode msTENG had a multifilm structure, which used a tadpole-like PET film as the substrate, a FEP film and a natural latex film as the triboelectric materials, an acrylic annulus as the spacer, and ITO coated on the backside of FEP as the single electrode. It

could be flexibly mounted and hidden behind an eyeglass temple via an adjustable fixator made of acrylic sheets, screws and springs, with the natural latex touching the facial skin around the eye. During operation, the eye blinking process induces the movement of the muscle around the eye, which changes the distance between the natural latex and FEP and results in a change in the electric potential of the single electrode. By integrating the msTENG with a signal processing circuit, eye blinking could work like a remote prosthetic hand and control the on/off status of electrical appliances such as a table lamp, fan and doorbell. The msTENG-based system could also be used to build a hands-free typing system. The user could type different letters by voluntarily blinking the eye according to the preset instructions. This noninvasive, highly sensitive TENG-based sensor enables people to control and communicate in a unique hands-free way with unprecedented convenience and intelligence.

An acoustic HMI for translating sound into electrical signals is another hands-free solution that plays an important role in information security and intelligent robotics. The first TENG-based acoustic device that could function as a sustainable energy harvester and an active sensor simultaneously was developed by Yang et al. in 2014.[31] The concept of a paper-based TENG with the same capabilities was proposed subsequently, introducing additional advantages such as ultra-thinness and rollability.[32] Such devices have been demonstrated for use as an acoustic source locator and a self-powered microphone.[36, 37] Recently, a self-powered triboelectric auditory sensor (TAS) was proposed for social robotics and hearing aids.[48] The multilayer TAS consisted of an Au-coated FEP film attached on an acrylic substrate, a spacer and an Au-coated Kapton membrane (Figure 40d). The FEP-covered acrylic substrate had hole channels to reduce air damping and the Kapton

membrane was fixed on the outer rim by an annular acrylic sheet. Membrane deformation caused by acoustic waves triggered the contact and separation between FEP and the membrane electrode, and thus generated electrical outputs. The fabricated TAS device achieved an ultrahigh sensitivity of 112.4 mV/dB, with applications such as a sound-controllable switch and an antitheft system demonstrated. More importantly, the frequency response of the TAS could be tuned and optimized by the introduction of annular or sectional inner boundary architectures, which enables it to have applications in an electronic auditory system with high quality and fidelity in sound recording as well as security systems using voice recognition. The TAS with tunable frequency response also has huge potential in hearing aids since the signals of the impaired frequency region can be naturally enhanced through device design. Such a TAS-based system greatly reduces the complexity and cost of signal processing circuits in conventional hearing aids.

## 4.2 Keystroke Dynamics Enabled Authentication and Identification using TENG Array

Keystroke dynamics, first proposed by Spillane in 1975,[170] is a behavioral biometric based on people's typing attributes. Its ballistic nature[171] and non-invasive monitoring characteristics[172, 173] have fostered its applications in multi-factor authentication[174] for enhanced cyber security, especially after the establishment of its singularity to the typist by both the National Science Foundation and National Institute of Standards and Technology in the 1980s[175]. However, most academic and industrial efforts[171] utilize only the features of keystroke latency and key hold time, without taking into account the typing force, typing speed and/or finger size of individuals.[176-179] Here we developed a two-factor authentication and identification system composed of a triboelectric keystroke device that

can continuously collect a user's intrinsic behavior reflected in keystroke dynamics, a customized signal processing scheme for feature extraction, and a support vector machine (SVM) algorithm based platform for user classification. The triboelectric keystroke device can transduce the typing motion including the effects of typing force and contact area into the electrical signals, and its touch-proof feature offers an improved signal-to-interference-plus-noise ratio (SINR) compared to previous active sensing devices based on triboelectrification.[33, 35, 180] The SVM-based platform,[181] with a rationally designed training stage and the capability of handling nonlinear features in keystrokes, is much more advanced than previously used statistical-based approach.[180] This one-stop, hardware-plus-software security system is capable of authenticating and even precisely identifying users through their unique typing behaviors at the terminals, with an accuracy up to 98.7%. The promising application of this novel system in the financial and computing industry can push cyber security to a new level, where leaked passwords would possibly be of no concern.

### *4.2.1 Triboelectric Keystroke Device*

The proposed system consists of two processes, the training process and the authentication/identification process (Figure 41a). During the training process, users will input a string of characters through the keystroke device, followed by the acquisition of the induced electrical signals. Pre-defined features will then be extracted from the acquired signals and used to construct a profile database. During the authentication/identification process, a test profile will be built following the same procedures and cross-referenced with the existing profile database to either determine if the test subject is an authorized user (authentication) or identify who the test subject is (identification). The design of our

triboelectric key is depicted in Figure 41b. Its structure was made of silicone, and it had three electrodes - a shield electrode, a top electrode and a bottom electrode. As a proof-of-concept demonstration, a numeric keypad consisting of 16 triboelectric keys similar to those commonly seen in financial institutions, was fabricated in this work. It is stretchable and conforms to rounded surfaces (Figure 41c), making it more adaptable for today's highly mobile society. From the perspective of working mechanism, the triboelectric key consists of a shield electrode and a contact-separation-mode triboelectric nanogenerator (CS-TENG).[2, 10, 18] The enclosed CS-TENG is responsible for transducing the typing behavior into analog electrical signal for data acquisition,[182] while the shield electrode is to minimize undesirable components in output signals originating from inadvertent touch or variations in working conditions, such as wet or dirty fingers.

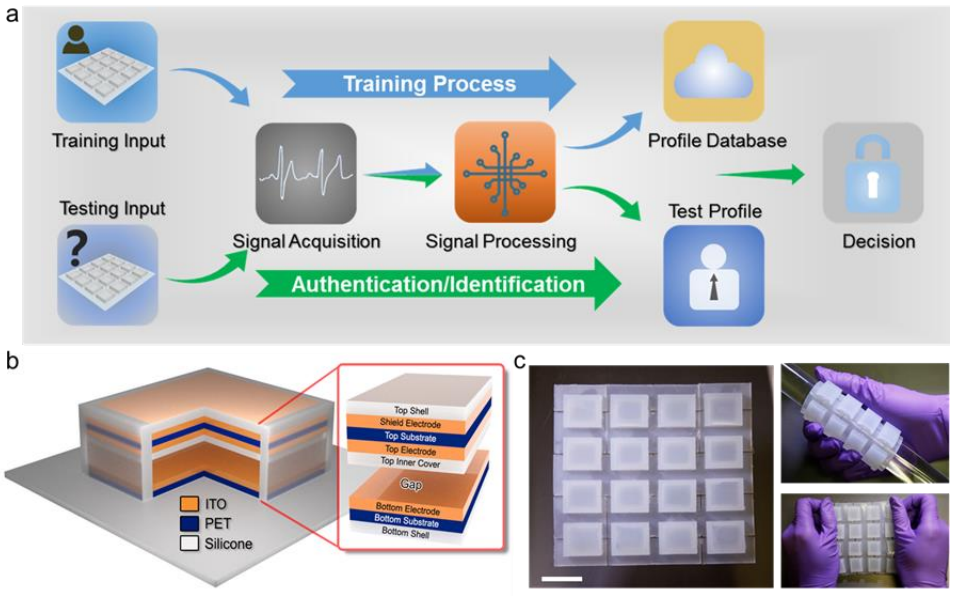


**Figure 41. The two-factor authentication and identification system.** (a) The system outline consisting of the training process and the authentication/identification process. (b) Schematic and exploded view of a single triboelectric key. The shield electrode and the top electrode were embedded into the top silicone shell of the key, while the bottom electrode was attached on the bottom silicone layer and exposed to the inner gap of the key. PET

films were used as the supporting substrates for all electrodes. (c) Photographs of the proof-of-concept triboelectric numeric keypad consisting of 16 keys at different mechanical states (Scale bar: 2 cm). Reproduced with permission.[151] Copyright 2018, Elsevier.

To reveal the practical shielding effect, the electrical outputs from our triboelectric key and a reference key without shield electrode as a human finger slowly approaches, presses, releases and leaves the keys, were tested, with the results plotted in Figure 42a. For our triboelectric key, the undesired voltage components induced from touch, denoted by T1 and T2, were greatly reduced and hence the SINR was improved from around 2 dB to nearly 10 dB, where SINR is defined as $10\log_{10}(V_{press}/(V_{touch}+ V_{noise}))$.[183] Therefore, the rationally designed triboelectric key can hugely diminish the effects of inadvertent touch from the fundamental physical level. Furthermore, the pressure-sensitive signal from the fabricated triboelectric key device makes it possible to introduce factors such as typing force and finger size into keystroke dynamics without the necessity of conventional pressure sensors. Figure 42b presents the maximum output voltage of the device under various typing forces with a contact area of 1 $cm^2$. Three different response regions were observed and can be attributed to the different contact statuses between the top and bottom parts. The first transition occurs when the typing force enables the contact between the two parts, while the second one is due to the saturation of the contact area. The increase in contact area can induce a more significant increase in output voltage than the decrease in gap distance, which explains why the closed-gap region has a steeper slope (17.63 *V/N*) than that of the first open-gap region (1.72 *V/N*). The durability of the key device was also tested and proved to be fully functional even after eight thousand typing cycles under the same stimulated conditions. The surface of the device was chemically treated as well to

make it hydrophobic with a contact angle of 126° and more resistant to moisture and dirt, further improving device stability.

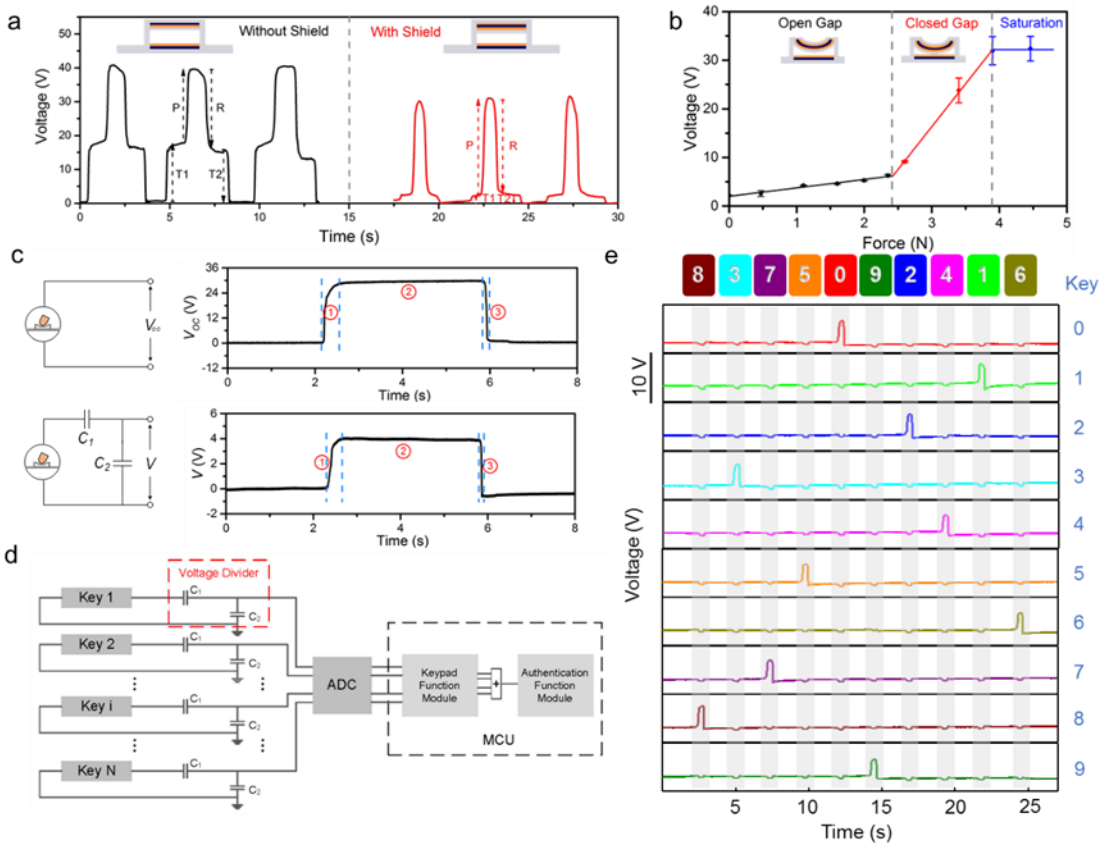


**Figure 42. The triboelectric-key-based numeric keypad.** (a) Comparison of electrical outputs from our triboelectric key and a reference key without shield electrode. Our key with shield electrode yields a one-magnitude-larger SINR. (b) The relationship between the maximum output voltage from our triboelectric key and the typing force. The responses can be categorized into three different regions, open-gap, closed-gap and saturation, depending on the different contact statuses between the top and bottom parts of the key. (c) The capacitor-based voltage-dividing scheme to transform the key output signals to be compatible with common ADCs. Three labelled stages correspond to the pressing, hold and releasing of the key during normal typing. (d) Equivalent electrical circuit for a keystroke device consisting of multiple triboelectric keys. (e) Electrical signals from the fabricated numeric keypad by sequentially inputting the digits "8-3-7-5-0-9-2-4-1-6". Reproduced with permission.[151] Copyright 2018, Elsevier.

The detection of keystrokes on a keypad/keyboard is realized through multichannel measurement, which is typically handled by a multichannel analog-to-digital converter

(ADC) with a limited range of operation voltage - for instance, within ± 10 V for most National Instrument DAQ devices. However, active open-circuit-voltage ($V_{OC}$) signals from CS-TENG tend to be tens to hundreds of volts,[10] as further evidenced by the top plot in Figure 42c for our key, and thus a voltage divider is required before connecting triboelectric devices to portable multichannel measurement systems. Considering that the functioning element in a triboelectric key, the CS-TENG, has an equivalent electrical circuit consisting of a voltage source and a serial variable capacitor, we proposed a capacitor-based voltage-dividing scheme, with its equivalent electrical circuits and typical voltage outputs from normal typing plotted in the bottom of Figure 42c. Two capacitors with rationally selected capacitance ($C_1$: 330 pF, $C_2$: 660 pF) are connected to the triboelectric key and only the voltage across $C_2$ is measured as the output signal, which can be represented by

$$V = \left( \frac{V_{OC}(t)}{1/C_{TENG}(t) + 1/C_1 + 1/C_2} \right) \Big/ C_2 \tag{20}$$

The divided voltage signal has been lowered to about 5 *V* while keeping the shape of the OCV as well as retaining all the keystroke information such as applied typing force and hold time. The consequent equivalent electrical circuit for a keystroke device consisting of multiple triboelectric keys is illustrated in Figure 42d. The analog voltage signals are measured by the ADC module and then sent to the Microprogrammed Control Unit (MCU) for subsequent processing and analysis, including the digital filtering, denoising, baseline elimination, feature extraction and so on. The electrical signals from the fabricated numeric keypad by sequentially inputting the digits “8-3-7-5-0-9-2-4-1-6” are plotted in Figure 42e. Each typed digit is clearly recorded by the voltage change in the

corresponding channel, while the induced noise in other channels are negligible, demonstrating the successful implementation of the triboelectric device as a numeric keypad.

### *4.2.2 SVM-Algorithm Based Software Platform*

A customized SVM-based software platform (Figure 43) was developed and integrated with the triboelectric numeric keypad to construct a two-factor authentication/identification system (Figure 44a). Analog voltage signals transduced from keystrokes is firstly converted to digital signals by the hardware circuits consisting of voltage dividers and an ADC. Subsequently, the keystroke features (defined as in Figure 44b), such as typing latencies (*L*), hold time (*H*) and signal magnitudes (*M*), are extracted using specific signal processing techniques, e.g., denoising, baseline elimination and peak detection. For an exemplary number sequence consisting of six digits, "8-0-7-3-4-5", a total of 17 features can be obtained accordingly and the radar plot of their normalized mean values shows distinctive typing behaviors among five different users (Figure 44c). In the training process, these normalized feature vectors are then used to build user profile models via supervised learning with the help of principle component analysis (PCA)[184] and SVM. For the implementation of the authentication and identification, a similar process is carried out and the test user profile is cross-referenced with the existing profile database for decision making through a pre-trained classifier. The classifier is built upon a customized classification algorithm modified from the LibSVM toolbox[185, 186], which achieves a satisfactory tradeoff between computational complexity and prediction accuracy, and fits the scenario of a large number of users well. Moreover, it can be analyzed theoretically with a precise probability model and avoid the over-fitting issue of the training sets. The

classical two-class (binary) SVM classifier is adequate for authentication while the multi-class SVM classifier[187] is adopted for identification, with the latter extended from the former through the one-against-all strategy.

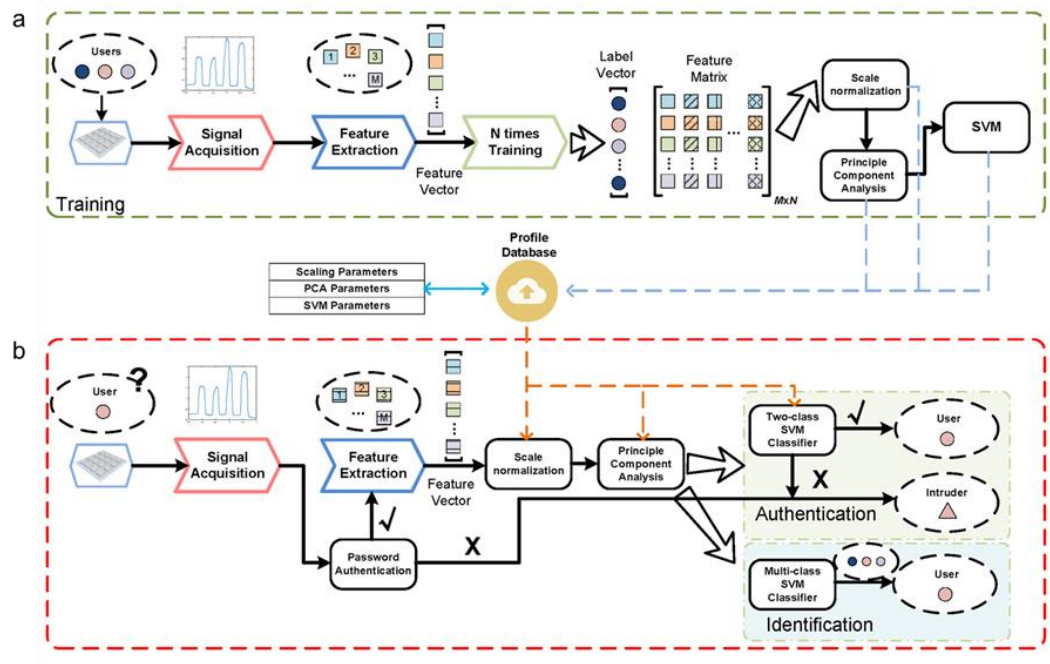


**Figure 43. The process flow of the proposed authentication and identification system combined with the classification algorithm.** (a) The training process. (b) The authentication and identification process. Reproduced with permission.[151] Copyright 2018, Elsevier.

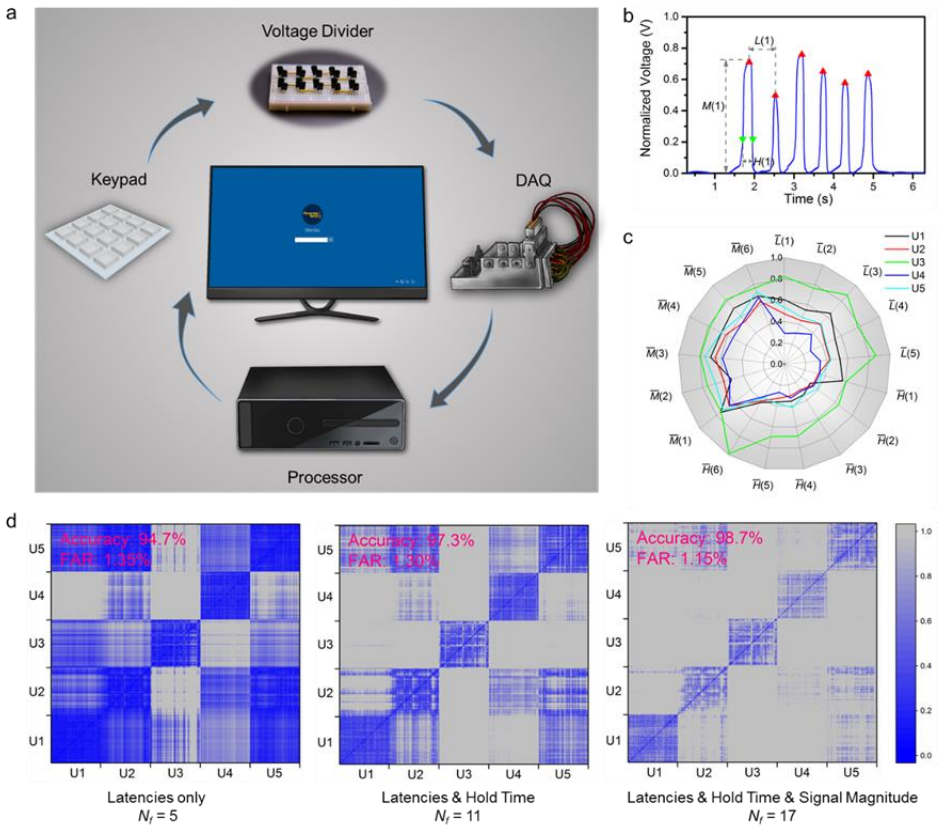


**Figure 44. The two-factor authentication and identification system built upon the triboelectric keystroke device.** (a) The hardware schematic of the experimental system. (b) The keystroke features defined to construct user profile models. Typing latency, hold time, and signal magnitude are denoted as *L*, *H*, and *M* respectively. (c) The radar plot of the normalized mean feature values of five users after they typed the number sequence "8-0-7-3-4-5" for 150 times each. A total of 17 features, 5 typing latencies, 6 hold time and 6 signal magnitudes, can be extracted from the 6-digits sequence. (d) The difference score matrices across user inputs with varying combinations of feature types. Reproduced with permission.[151] Copyright 2018, Elsevier.

### *4.2.3 Classification Results*

The 150 sets of data from each user were randomly split into two halves, one for training and the other for testing. The classifier performance was optimized by tuning the decision threshold value and comparing the resulting false rejection rate (FRR) and false acceptance rate (FAR). With the optimal decision threshold of 0.75, the tradeoff between a low FRR and a low FAR can be well satisfied so that an equal error rate (EER) as low as

1.15% can be achieved (Figure 45a). A standardized receiver operating characteristic (ROC) curve (Figure 45b), defined as the plot of the true positive rate (TPR) against the FAR at various threshold settings, is calculated and gives an enclosed area of 0.9967, indicating a very good classifier.

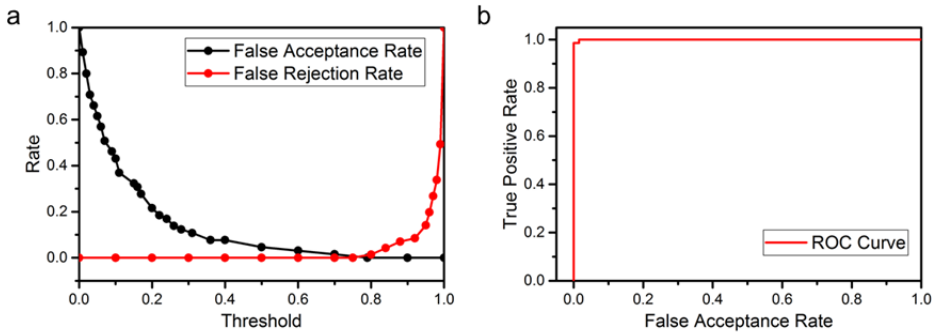


**Figure 45. Classifier performance.** (a) Plot of FAR and FRR with respect to different threshold values. (b) The ROC curve of the customized classifier. Reproduced with permission.[151] Copyright 2018, Elsevier.

To quantify the difference of users' typing patterns with varying combinations of feature types, a difference score between two typing inputs is introduced based on the normalized interval distance.[188, 189] It is defined as

$$S = \sum_{i=1}^{N_f} S_{f^1(i), f^2(i)} = \sum_{i=1}^{N_f} \left| \frac{f^1(i) - f^2(i)}{f^1(i)} \right| \tag{21}$$

where $f(i)$ is the value of feature $i$, $N_f$ is the total number of features, and $S_{f^1(i), f^2(i)}$ is the contribution to the difference score from the feature $i$. The difference score between inputs from the same user and different users is plotted in Figure 44d. Ideally the scores across the diagonal should be much lower (more blue) compared to the rest to indicate that the inputs from the same user differ significantly less than those across users. Clearly the

introduction of more features such as the hold time and signal magnitudes could produce more ideal score matrices, i.e., only inputs from the same user have the lower score (more blue), suggesting that the typing patterns between different users are more distinctive. The same conclusion can also be drawn from the perspective of system accuracy, i.e., by integrating the features of hold time and the features of signal magnitudes, the system accuracy can be improved and the FAR rate can be reduced compared to only adopting the features of typing latencies. By replacing standard input devices like commercial keyboards with the triboelectric keystroke system, an imposter knowing the correct password still could not log onto the computer system unless his/her typing dynamics matches the information stored in the system. By switching the customized classifier in the system from the binary mode to the multi-class mode, the system can serve for identification purposes and identify different users even if they typed the same codes.

The two-factor authentication and identification system built upon the triboelectric keystroke device and the SVM-based platform offers a facile and reliable solution for enhanced keystroke dynamics. It provides a higher level of cyber security by integrating the influence of typing force while excluding the effects from undesirable sources, such as inadvertent touch and changes on typing surfaces. Security concerns about password leaking can be greatly alleviated. The approach can be even more reliable than fingerprint based authentication that can be easily replicated. Meanwhile, the rationally designed, unconventional keystroke device is flexible, stretchable and water/dust proof, which makes it highly mobile and applicable to versatile working environments. Hence, its application as input devices in the financial and computing industry is promising and meaningful for user identification and information protection.

### *4.2.4 Experimental Methods*

#### 4.2.4.1 Fabrication of Triboelectric Keystroke Device

Pre-cured silicone rubber (Ecoflex 00-50, Smooth-On) was prepared by mixing the two components in a 1:1 volume ratio., and acrylic molds for top and bottom silicone shells are fabricated using a laser cutter (PLS6.75, Universal Laser Systems). The prepared silicone rubber was casted into the acrylic molds and cured at 50 °C for 6 hours. The top and bottom silicone shells of the triboelectric keystroke device were then peeled off from the molds. Thin films of PET were coated with ITO using magnetron sputtering (PVD75, Kurt J) and laser-cut into the size of a single key. Two-sided coated PET films were placed onto the top silicone shell and covered with another layer of silicone, i.e. the top inner cover; One-sided coated PET films were pasted onto the bottom silicone shell with the ITO layer facing up. Finally, the top and bottom parts of the triboelectric keystroke device were assembled together using the pre-cured silicone rubber as the glue. A superhydrophobic coating (Rust-Oleum® NeverWet®) was facilely sprayed onto the device to achieve a water and dust resistant surface and the contact angle was measured using a ramé-hart Model 250 Standard Goniometer.

#### 4.2.4.2 Electrical Output Measurements

The open-circuit voltage and short-circuit current from the triboelectric key were measured by a Keithley 6514 system electrometer. Reduced voltage outputs after the capacitor/resistor-based voltage division were measured by an ADC (NI 9220, 16-Channel Voltage Measurement Module, ± 10 V, National Instrument), which was also used for the multichannel measurement. For the voltage-force and durability testing the typing motion

was stimulated using a 1cm × 1cm acrylic covered by a nitrile glove and driven by a programmable linear motor. All other signals were from human typing.

#### 4.2.4.3 Signal Processing and Software Interface

The signal acquisition, timing synchronization, and the graphical user interface were implemented using LabVIEW 2016. The signal processing including denoising, feature extraction and classification, was implemented with MATLAB® 2016b. Some core algorithms are accelerated with C++.

## 4.3 Self-Powered Wireless Optical Transmission of Mechanical Agitation Signals

With the popularity of IoT, the ubiquitous existence of sensors has brought great convenience to daily life, but it also raised serious challenges to the wireless communication access.[45, 46, 190] Current solutions for IoT communications are dominated by traditional radio frequency (RF) based techniques, e.g., the wireless local area networks (WLAN), Cellular, Bluetooth, Zigbee, and Radio-frequency identification (RFID) and etc.[191-194] However, the RF band of the electromagnetic spectrum is fundamentally limited in capacity and costly since most sub-bands are exclusively licensed, resulting in spectrum crisis especially in the scenarios with dense sensors.[195, 196] In this context, the optical wireless communications (OWC) which utilizes the huge and unlicensed optic bandwidth for data transmission, provides a promising alternative to alleviate the spectrum crisis.[197-199] Besides, the OWC technology has many other attractive features such as worldwide availability, radiation-free, and high-capacity, and thus is regarded as an appealing complementary communication solution for IoT applications.[200]

According to the different optical carriers used by transmitters, OWC can be categorized into three main types, i.e., visible, infrared (IR) and UV light communications.[201, 202] The OWC can also be classified based on the receiver types, including the photo detector and camera based methods.[203, 204] Nevertheless, existing OWC transmitters usually rely on DC power supply, which induces high maintenance cost and limits its applications where only the event trigger is needed to monitor. To the best knowledge of the authors, there is no appealing scheme to address this problem. Meanwhile, a small TENG device (size of 1 in × 1 in) can easily light up tens of LEDs with a simple contact and separate operation,[61] and thus TENG may be employed as a competitive power supply for OWC to wirelessly monitor mechanical stimuli.

In this paper, we demonstrated a self-powered, TENG-driven OWC with the capability of wireless control, sensing and even authentication. The concept of self-powered OWC was firstly proposed, and by an integration with TENG-based sensing devices, a LED array can directly work as a wireless transmitter to convey the information associated with mechanical stimuli without additional electrical power supply. With different TENG devices and machine learning techniques, three systems with functions of remote control/event monitoring, pressure sensing, and security authentication, were then implemented and evaluated for practical feasibility in the laboratory environment. Other possible applications and potential improvements are discussed in this paper as well. The concept and results in this paper may greatly broaden the application of IoT through the integration of OWC and TENG.

### *4.3.1 Design of System Framework*

The systematic concept of the self-powered OWC system driven by TENG is illustrated in Figure 46. The whole system can be divided into two sections, i.e., the transmitter and the receiver. The transmitter is mainly consisted of the TENG device and the LED or LED array. Under mechanical stimuli, corresponding units of the TENG device would be triggered and produce a HV output, which can easily power one to several LEDs without any rectification or analog to digital conversion (ADC) modules. By associating the LEDs with corresponding TENG units, the status information (location, elapsed time, force, and *etc.*) of the external mechanical stimuli can be reflected by the "on-off" blinking of the corresponding LEDs. In other words, the TENG works as both the event trigger and the power source for the OWC transmitter. Compared to the traditional scheme, the one we proposed does not rely on additional electrical power sources and eliminates the need of complicated power management circuits. In practice, various types of mechanical events or triggers (for example, moving, pressing, vibrating, kicking or sliding) based on TENG can be designed and adopted [47, 132, 205] The LED size, power and type (optical carrier band) can also be optimized according to the requirements of the specific applications.

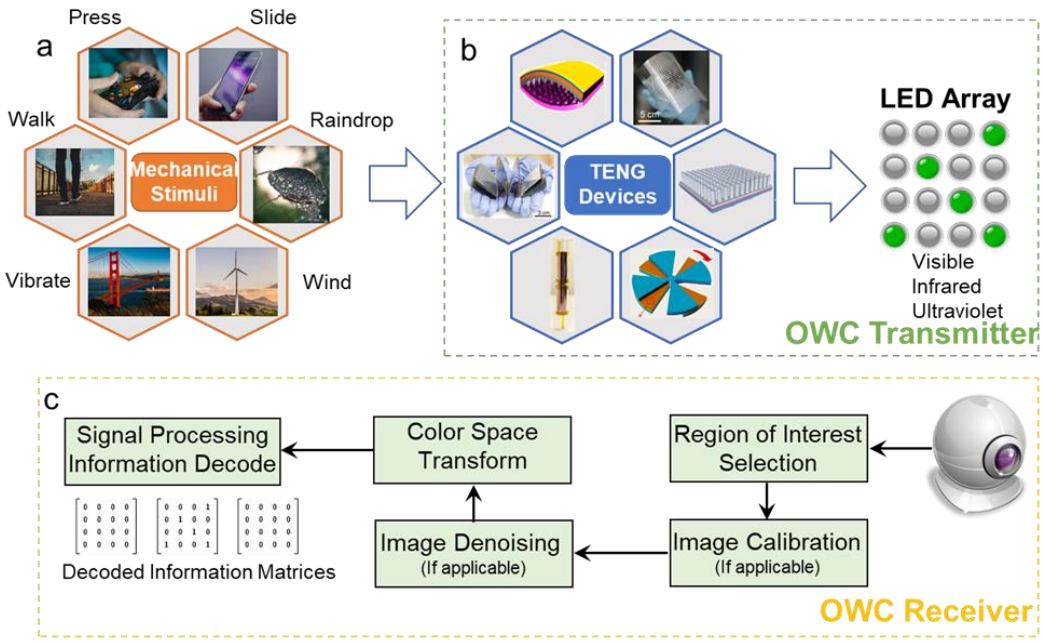


**Figure 46. Schematic illustration of self-powered OWC driven by TENG.** (a) The potential mechanical stimuli that can be monitored. (b) Use different TENG devices to be triggered by the mechanical motions and form the OWC transmitter with the LED array. (c) The OWC receiver to detect the information conveyed by the light. Reproduced with permission.[130] Copyright 2018, Elsevier.

As for the receiver, either photo detector or camera can be deployed to receive the optical information according to the requirements in specific applications. Here, the camera based detection scheme is adopted for a simple and low-cost implementation. The camera captures the video of the LED array at a configured frame rate (denoted as $f_p$ which is typically 30 frames per second). According to the Nyquist-Sampling theorem, the desired information signal conveyed by the LED blinking can be guaranteed for perfect recovery with appropriate signal processing as long as the desired signal frequency $f_i$ is less than half of the sampling rate, i.e., $f_i < f_p$.[206] The subsequent information detection process in our OWC system includes the region of interest selection (extract the desired image region from the original picture to reduce the processing time of following steps), image calibration (make proper corrections to the image rotation caused by the receiver position),

color space transformation (transform the image to other color space and enhance the desired information component), image processing (apply advanced techniques for further processing), and the final information decoding (obtain the desired information). To better illustrate the concept of the self-powered OWC driven by TENG, we implemented three demonstrations for different applications in this work.

### *4.3.2 Self-Powered Wireless Remote Control*

In this application, we utilized the self-powered OWC to realize the wireless remote control. A double-electrode contact-separation (CS) mode TENG (size of 1 in × 1 in) was fabricated as shown in Figure 47a. The CS-TENG uses the Cu foil and PTFE film as the positive and negative triboelectric surfaces, respectively. When a "press and release" mechanical force is applied to the TENG device, a pulsed voltage can be delivered, as illustrated in Figure 47b. Then by wiring TENG to a LED, such voltage output will drive the LED to have a "on-off" behavior, which can be captured by the video camera (LifeCam Studio, Microsoft) at the receiver. It should be noted here that different modes or structures of TENG can be deployed separately or together, if various kinds of mechanical motions, for example, sliding, vibration and etc., need to be detected.

By analyzing the "on-off" status of the LED from the image captured in each frame, the mechanical motion can be detected and the remote control will be realized. Typical "on" and "off" LED images together with their intensity histogram of the red-green-blue (RGB) color space are shown in Figure 47d and Figure 47e. Distinctive difference in the intensity distribution of the "on" and "off" images, especially in the green component intensity, can be observed. Additionally, we fabricated four such TENG units to form a

simplest direction keyboard and successfully played the Tetris game using it, as demonstrated in Figure 47f.

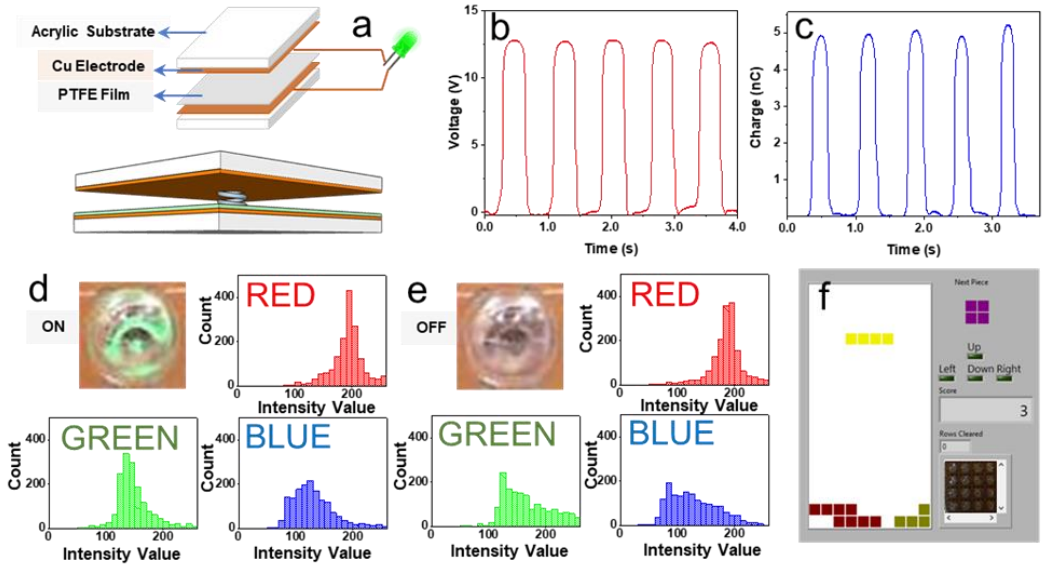


**Figure 47. Self-Powered wireless remote control.** (a) The schematic diagram showing the TENG device structure and the circuit connection of the TENG device with the LED lamp. (b) The open-circuit voltage output of the TENG device triggered by hand. (c) The transferred charge amount of the TENG device triggered by hand. (d) The intensity histogram of the RGB color space of a typical "on" LED image. (e) The intensity histogram of the RGB color space of a typical "off" LED image. (f) The Tetris game interface played with the proposed system (programmed via Labview 2016). Reproduced with permission.[130] Copyright 2018, Elsevier.

### *4.3.3 Self-Powered Wireless Tactile Array for Pressure Detection*

In this application, the self-powered OWC was utilized to realize wireless pressure detection. As a proof-of-concept demonstration, a TENG tactile array (touch panel) with 4x4 taxels was fabricated, and its structure is illustrated in Figure 48. Each taxel has a square size of 1 cm × 1 cm. The touch panel uses ITO as the electrode, a PDMS film as the triboelectric layer and a PET film as the substrate, which guarantees the transparency and flexibility. As shown in Figure 48a, it is transparent and flexible, which is suitable for the

electronic trends nowadays. The working mechanism of this tactile array is based on the single-electrode contact-separation mode of TENG. In this case, the pressing object acts as the other triboelectric layer while a reference grounded electrode is taken as the other electrode.

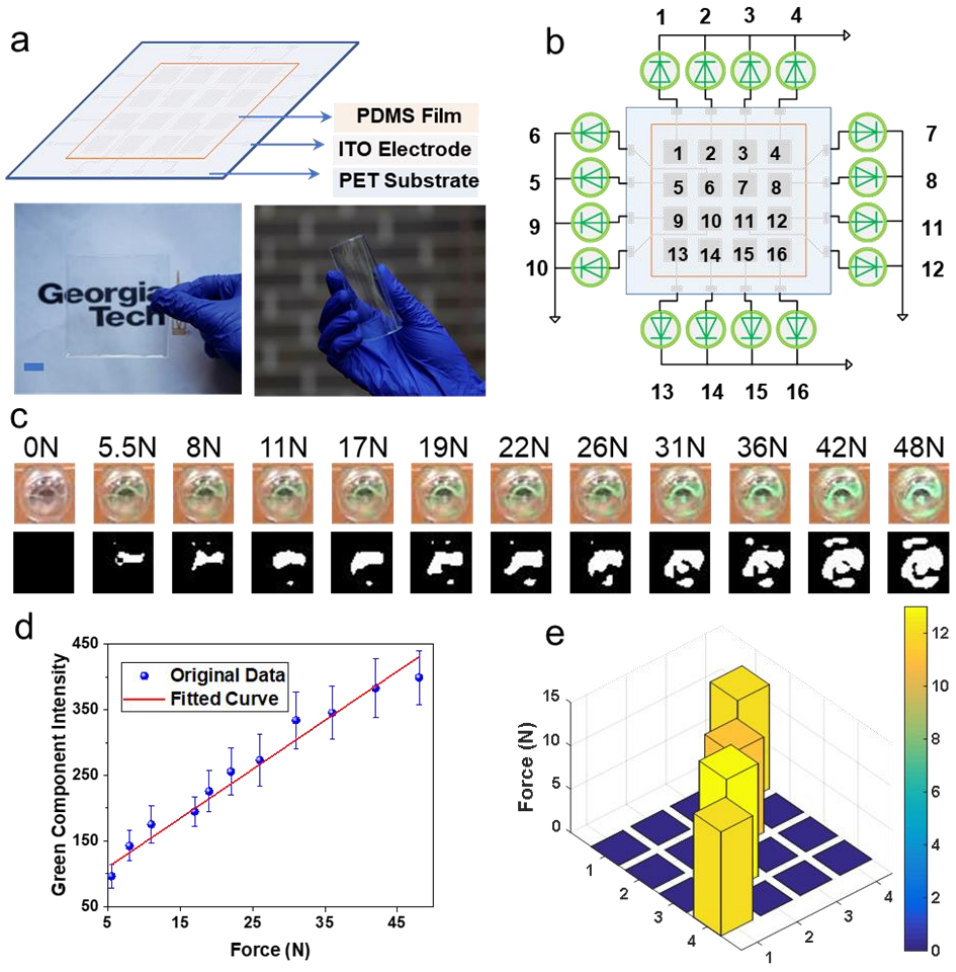


**Figure 48. Self-powered wireless tactile panel for pressure detection.** (a) The schematic diagram (up) and photographs (bottom) of the TENG device (a 4x4 tactile array), which is transparent (bottom left) and flexible (bottom right). Scale bar: 1cm. (b) The circuit connection of the TENG device with the LED array (a 4x4 LED array). (c) The typical LED images and the corresponding green component intensity images after processing at different forces applied to the tactile pixel. (d) The relationship between the green component intensity detected from the captured LED image and the force applied to the corresponding taxel. The pressing was simulated by a 1 cm × 1 cm acrylic plate covered with nitrile glove and driven by a linear motor. (e) The detected force output when four

taxels on the diagonal were pressed simultaneously. Reproduced with permission.[130] Copyright 2018, Elsevier.

The circuit diagram is shown in Figure 48b, where each taxel is wired to a corresponding LED. The higher the driving voltage is, the brighter the LED will be. Since the green light LEDs were used in this study, the brighter light would contain stronger green component. Typical LED images and the corresponding green component intensity images after processing at different forces applied to the taxel are provided in Figure 48c. The white area in the intensity image is used to indicate the intensity of the green component: the larger, the higher. Additionally, experiments were conducted to quantify the relationship between the green component intensity in the captured LED image and the applied force, which gives a great linearity as in Figure 48d. As a tactile array, the system can detect the magnitudes of forces applied to different taxels simultaneously. When four taxels on one diagonal of the tactile array were pressed with four fingers, the detected intensity can clearly reflect the force distribution, as shown in Figure 48e.

### *4.3.4 Self-Powered Wireless Touch Panel for User Authentication/Identification*

In this application, we utilized the self-powered OWC to realize user authentication/identification. Specifically, the tactile array fabricated above can also be used to sense the sliding motion on it and power the LED array. The voltage generation mechanism here is based on the single-electrode sliding mode of TENG[23]. The users' sliding biometrics, including the touching force and the sliding speed, can be captured by this OWC system. Therefore, the device can work as an intelligent interface for authentication or identification to distinguish the users even with the same sliding password.

In this work, five people were invited repeatedly to slide a z-type password on the touch panel (Figure 49a left) for 50 times each. The LED array were lighted accordingly, as illustrated in Figure 49a right. Figure 49b show the detected intensity-time plots of one user. Two factors of user biometrics can be extracted from these plots, e.g., the signal magnitude (denoted as *A*, reflecting the touching force) and the sliding latency (denoted as *T*, reflecting the sliding speed). For the z-type sliding across the "1-2-3-4-7-10-13-14-15-16" taxels, a total of 19 features can be obtained accordingly, *i.e.* 10 signal magnitudes and 9 sliding latencies. The radar plot of the normalized mean feature values of five users is shown in Figure 49c, which shows the distinctive "slide to unlock" behaviors. To improve the accuracy and robustness of the authentication and identification, we adopted the supervised machine learning to build up the user profiles for classification.[185, 207] The working process is illustrated in Figure 49d. The 50 sets of data from each user were randomly split into two halves, one for training and the other for testing. The classifier performance was optimized by tuning the decision threshold value and an accuracy of 95.2% was achieved.

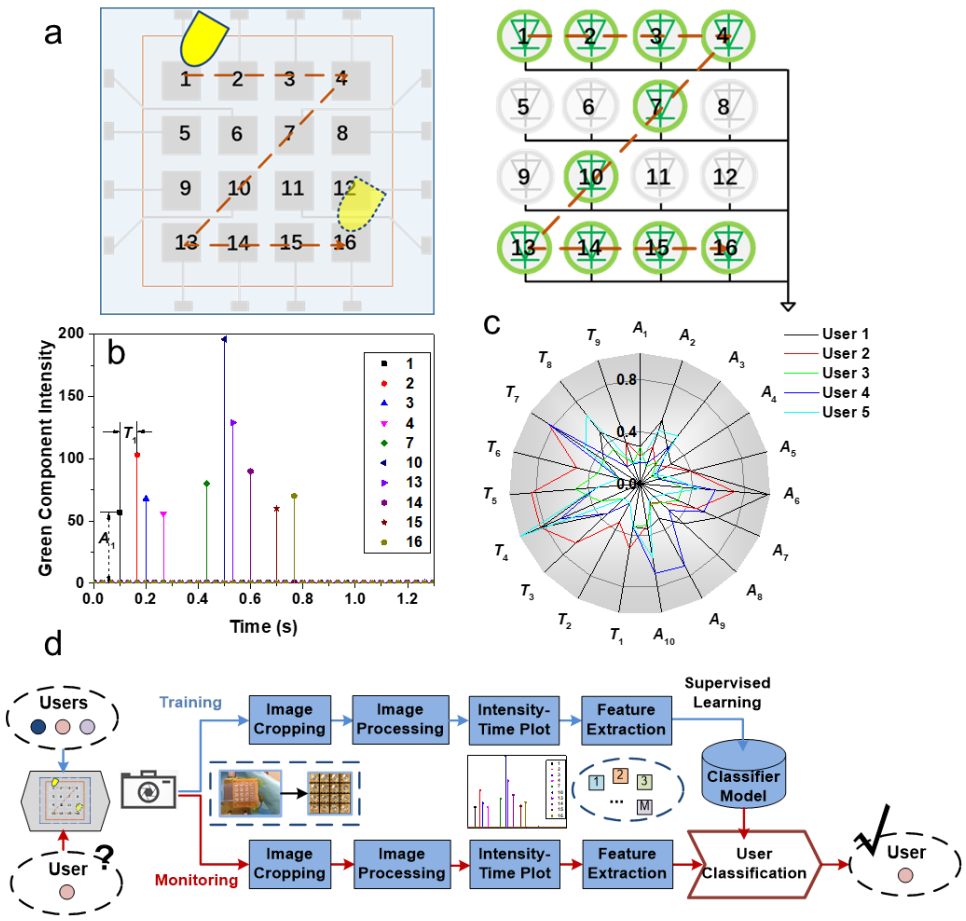


**Figure 49. Self-powered wireless touch panel for user authentication/identification.** (a) The schematic diagram of a z-type "slide to unlock" action on the TENG based touch panel (left) and the corresponding response of the connected LED array (right). (b) The intensity-time plot of User 1 and the sliding features defined to construct user profile models. Signal magnitude (LED intensity or touching force) and sliding latency are denoted as *A* and *T* respectively. (c) The radar plot of the normalized mean feature values of five users after they repeat the z-type "slide to unlock" action for 50 times each. A total of 19 features, 10 signal magnitudes and 9 sliding latencies, can be extracted from the z-type "slide to unlock" action going through 10 taxels. (d) The process flow of the proposed algorithm for user authentication/identification based on the supervised machine learning scheme. Reproduced with permission.[130] Copyright 2018, Elsevier.

In this work, the concept of the self-powered OWC driven by TENG is proposed. By powering the LED array with the TENG sensing device, the TENG can work as both the mechanical event trigger and the power source of the LED, and they can constitute a simplest OWC transmitter with no additional power supply or complicated circuits. With

the help of a video camera at the receiver and advanced image processing techniques, the information associated with the mechanical stimuli and conveyed by the LED light can be decoded appropriately. By considering the “on-off” feature, the “intensity” feature and the inherent biometrics feature step by step, three types of demonstrations with the capability of wireless control, pressure sensing and security authentication were implemented and evaluated for practical feasibility in the laboratory environment. For practical use, the specific devices, techniques and parameter configuration can be well designed and optimized according to the corresponding circumstances. Moreover, it can easily achieve multi-target monitoring if more than one such self-powered OWC transmitter is deployed and only one receiver is needed. The concept and results in this paper may greatly broaden the application of IoT through the integration of OWC and TENG.

### *4.3.5 Experimental Methods*

#### 4.3.5.1 Fabrication of TENG Controller Unit for Remote Control

Acrylic plates of 1 in × 1 in were laser cut (PLS6.75, Universal Laser Systems) and used as the substrates for TENG electrodes and triboelectric materials. Each TENG unit consisted of two acrylic plates, with one covered with Cu tape only and the other covered with Cu tape and then PTFE tape. A spring was used as the spacer and Kapton tape (Model S-7595, 3M) was applied to assemble all the parts.

#### 4.3.5.2 Fabrication of TENG Tactile Array

An electrode mask of 6 cm × 6 cm made of PVC film was firstly fabricated using laser cutting (PLS6.75, Universal Laser Systems). Then it was attached to a PET film (6

cm × 6 cm) and ITO electrode was deposited onto PET via sputter coating (PVD75, Kurt J). A PDMS film of the same size with the thickness of 500 μm was made through mold casting, and then attached to the ITO coated PET film.

#### 4.3.5.3 Electrical Output Measurements

The open-circuit voltage and transferred charge from the TENG device were measured by a Keithley 6514 system electrometer. For the intensity-force testing, the pressing motion was stimulated using a 1cm × 1cm acrylic covered by a nitrile glove and driven by a programmable linear motor. All other signals were from human pressing or sliding.

#### 4.3.5.4 Signal Processing and System Implementation

The video capturing was realized with the Microsoft Lifecam Studio webcam. The region of interest selection, image calibration, the graphical user interface and the Tetris game were implemented using LabVIEW 2016 powered with the Vision and Motion toolbox. The signal processing including denoising, color space transformation, green component intensity detection, feature extraction and classification, was implemented with MATLAB® 2016b.

# CHAPTER 5. APPLICATION OF TENG FOR HIGH VOLTAGE INSTRUMENTS

## 5.1 Recent Progress of TENG as Direct HV Power Sources

TENG has emerged as a novel alternative of conventional HV power sources with unprecedented portability and safety. Its intrinsic characteristic of HV eliminates the need of sophisticated power converters, and thus greatly reduces the system complexity and cost. The limited charge transfer per operation cycle of TENG offers an unprecedented way of accurately controlling HV-driven processes, and provides extra safety to personnel and instruments in the meantime.

One excellent example in this field is the use of TENG to generate nanoelectrospray ionization for highly sensitive nano-coulomb molecular mass spectrometry (MS),[208] which not only utilizes the HV output of TENG, but also transforms the limitation of charge transfer into an advantage of unprecedented control over ion generation. As shown in Figure 50a, a discrete amount of pulsed charges from the SF TENG were supplied to a nano electrospray ionization (nanoESI) emitter and triggered highly repeatable ionization pulses with minimum sample consumption. The duration, frequency and ion polarity were all tunable via TENG actuation on-demand, and the HV (5-9 kV) of the TENG provided nanoESI with enhanced sensitivity at low concentrations, as demonstrated by the signature fragment ion (*m*/*z* 182.118) only observable in the SF-TENG-driven nanoESI MS when analyzing a cocaine solution (10 pg/ml).

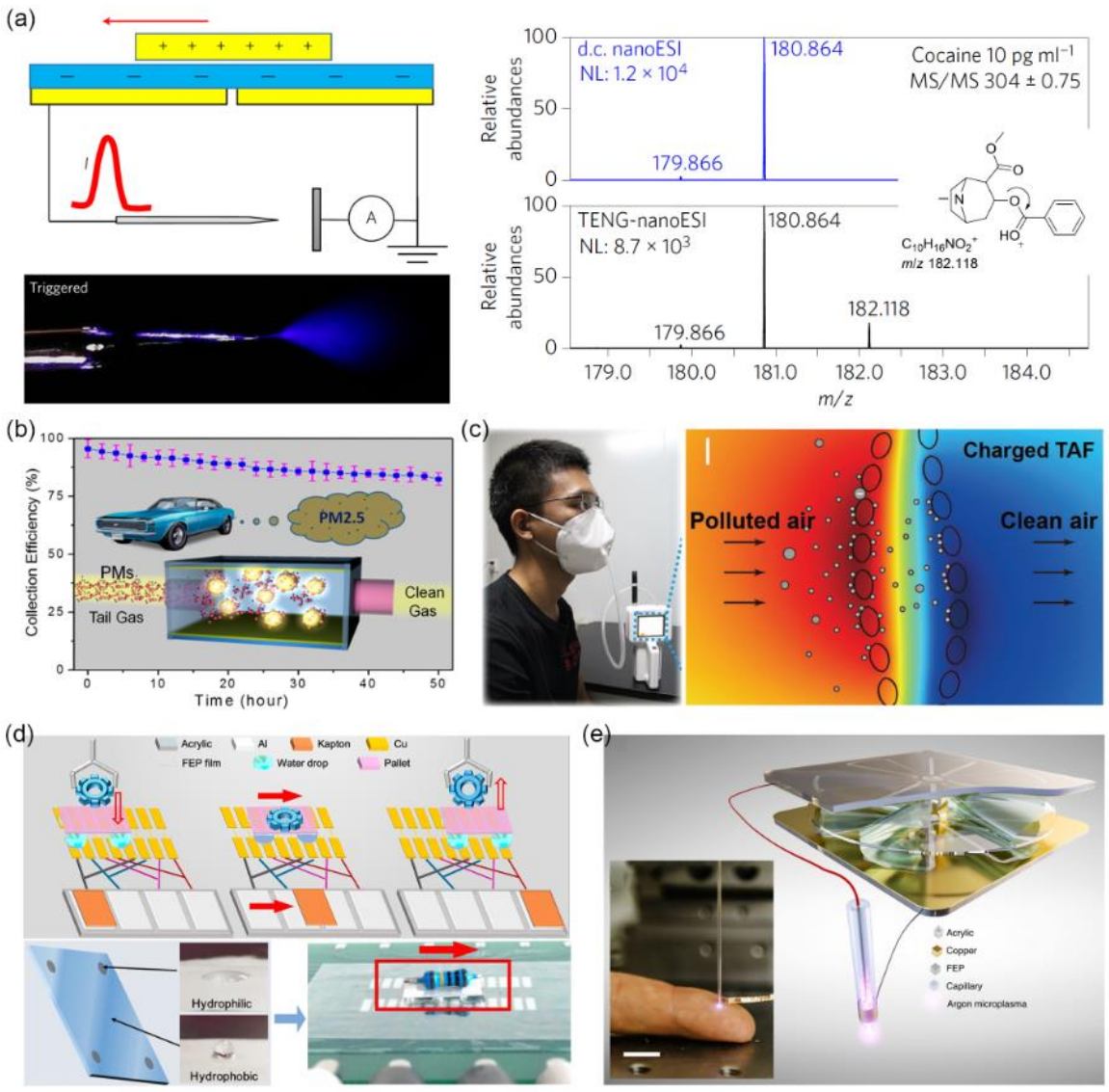


**Figure 50. Application of TENG as direct HV power sources.** (a) Sensitive nano-coulumb molecular mass spectrometry. Reproduced with permission.[208] Copyright 2017, Springer Nature. (b) PM removal from automobile exhaust fumes. Reproduced with permission.[209] Copyright 2015, American Chemical Society. (c) Washable air filter. Reproduced with permission.[68] Copyright 2018, Wiley-VCH. (d) Microfluidic transport system. Reproduced with permission.[210] Copyright 2018, American Chemical Society. (e) Triboelectric microplasma. Reproduced under the terms of the CC-BY 4.0 license.[211] Copyright 2018, Springer Nature. Reproduced with permission.[17] Copyright 2018, Wiley-VCH.

TENG-driven air cleaning, which was first proposed by Chen *et al.* in 2014,[67] is based on electrostatic precipitation and has huge potential in commercialization with the

growing severity of air pollution. Compared to conventional electrostatic precipitators, it can be self-powered and have no concern about ozone generation. The concept was first demonstrated using a wind-driven rotating TENG, whose rectified DC output was supplied to two parallel electrodes.[67] Charged particles were then collected by the electrodes due to Coulombic forces of attraction and repulsion. Subsequently, a self-powered triboelectric filter consisting of vibratory PTFE pellets and electrode plates was developed to remove the particulate matter (PM) in automobile exhaust fumes using the self-vibration of the tailpipe, achieving a mass collection efficiency of ~95.5% for $PM_{2.5}$ (Figure 50b).[209] Recently, a washable multiplayer triboelectric air filter (TAF) consisting of nylon fabrics and PTFE fabrics was developed.[68] Unlike commercial face masks, the removal efficiency was barely changed after the TAF was cleaned with commercial detergent, which makes it highly promising in fabricating a reusable and efficient face mask (Figure 50c).

The HV of TENG can also be used for electrostatic actuation. Chen *et al.* demonstrated a TENG-driven actuation system based on dielectric elastomer actuators, which could modulate the on/off status of an intelligent switch or the spacing of tunable optical gratings.[212, 213] With rationally designed electrodes on a chosen substrate, the voltage output of TENG provided the Coulomb force that modulated the motion of tiny objects such as water droplets and solid pellets.[214] As in Figure 50d, a self-powered microfluidic transport system driven by TENG was developed based on the working mechanism.[210] A mini vehicle consisting of four water droplets and an object-carrying pallet was placed on a hydrophobic surface, under which two lines of grating track Cu-electrodes were placed to guide the motion of the droplets. The track electrodes were connected periodically to the grid electrodes of a FS TENG, which consisted of a movable

Kapton film and four pieces of Al foil attached on an acrylic plate. As the Kapton moved, the output voltage of TENG generated Coulomb force to move the droplets and thus the mini vehicle.

With the integration of voltage boosting circuits, the voltage of a TENG can reach above 10 kV and can be used to drive many other HV processes such as electrospinning,[215] electron field emission,[216] and microplasma.[211] The concept of triboelectric microplasma was realized by Cheng *et al.* via the integration of TENG with a plasma source, and atmospheric-pressure plasma powered only by mechanical stimuli was achieved (Figure 50e). With the advantages of portability, controllability, safety and high efficiency, TENG-based power sources are believed to have wide applications in many fields, such as HV instruments, actuators, environmental protection, and human health.

## 5.2 Electrohydrodynamic Jet Printing Driven by TENG

Electrohydrodynamic jet (e-jet) printing is a high-resolution printed electronics technique that uses an electric field to generate droplets. The electric field is applied between the deposition nozzle and the substrate and induces mobile ions in the ink to accumulate at the liquid surface. The liquid meniscus is deformed into a conical shape, or the so-called Taylor cone,[217] due to the coulombic repulsion of ions, and a droplet is ejected towards the substrate once the stress from the charge repulsion at the cone apex exceeds the surface tension.[218] Therefore, e-jet printing is capable of producing ink droplets much smaller than the nozzle and has been regarded as a high-resolution printing technique. A sub-micrometer resolution (up to 700 nm) has been demonstrated using e-jet printing while the resolution limits of inkjet printing and aerosol jet printing are tens of micrometers.[219] It

also avoids the inherent clogging issue in inkjet printing and aerosol jet printing by achieving comparable resolution with a much larger nozzle.[220] E-jet printing has great potential in high-resolution electronics printing and has been successfully used to print various materials including conductive inks,[220, 221] DNA,[222] quantum dots,[223] and small organic molecules.[224] However, conventional HV power sources required for the process generally have high cost and pose major threats to substrates, surrounding instruments and operation personnel.

In this work, we managed to use TENG to drive the e-jet printing process. A rotary freestanding TENG (RF-TENG)[23, 94] connected with a simple boost circuit[211] could supply an open-circuit DC voltage above 1 kV, which was adequate to induce continuous droplet formation and ejection from the printing nozzle. The droplet jetting process was recorded using a high-speed camera with a variable frame rate up to 37350 fps, clearly showing the tunability of jetting frequency *via* the control of TENG operation frequency. Effects of nozzle moving speed and nozzle size on printed features at different TENG rotation speeds were studied as well. The TENG-driven e-jet printing setup was able to achieve feature sizes smaller than the nozzle diameters, with a minimum feature size of 135 μm using a nozzle diameter of 160 μm in our experiments without dedicated optimization of printing parameters. This performance is comparable to that using a commercial DC HV power source and the resolution is expected to be further improved by reducing the nozzle size and optimizing the nozzle-to-substrate distance. We also demonstrated its use for printing graphic arts, conductive interconnects and touch sensors. The TENG was simply operated using a rotary motor and the cost of the TENG device and boost circuit is less than 100 USD, while a commercial DC HV power source usually costs much more. With the merits

of controllability, high resolution, low cost and safety, we believe this TENG-driven e-jet printing process can be an excellent alternative of conventional DC HV driven process.

### *5.2.1 TENG-Driven E-Jet Printing Process*

A schematic of our proposed TENG-drive e-jet printing process is illustrated in Figure 51a. A RF-TENG is connected to the printing nozzle and the substrate through a voltage boost circuit. The movement of the printing nozzle is controlled *via* a robotic arm and ink inside the syringe is held steady *via* pneumatic control. The RF-TENG consists of two parts, one stator and one rotator. The stator is made of an acrylic sheet as the substrate, an Al-foil layer as the electrodes and an PTFE film as one triboelectric layer. In the Al-foil layer, two interdigitated radial arrays of electrodes, with each having 12 sectors connected at either the inner rim or the outer rim, are evenly distributed on the acrylic substrate and serve as the two electrodes of TENG. The rotator is made of an acrylic sheet with 12 evenly distributed nylon films hanging on it. The size of the nylon films is rationally chosen so that their free parts can cover about one electrode sector during rotation. The rotator is connected to the shaft of a rotating motor (Oriental Motor, BLFM230-A) through the center hole. The working mechanism of RF-TENG is presented in Figure 51b. The triboelectrification between the nylon film and the PTFE film induces positive charges on nylon and negative charges on PTFE. As the nylon sweeps across the PTFE film with the rotator, electrons will flow from one electrode to another due to electrostatic induction. The interdigitated electrode design ensures that continuous AC electricity can be generated as the rotator moves. A boost circuit consisting of variable boost units,[211] with its equivalent electrical circuit model shown in Figure 51c, is used to amplify the output voltage of the RF-TENG to achieve a steady, easily obtainable ink jetting process. Each boost unit

consists of four capacitors of 4.7 nF and four HV diodes as highlighted in Figure 51c. Such a setup with 5 boost units achieved an open-circuit DC voltage above 1 kV.

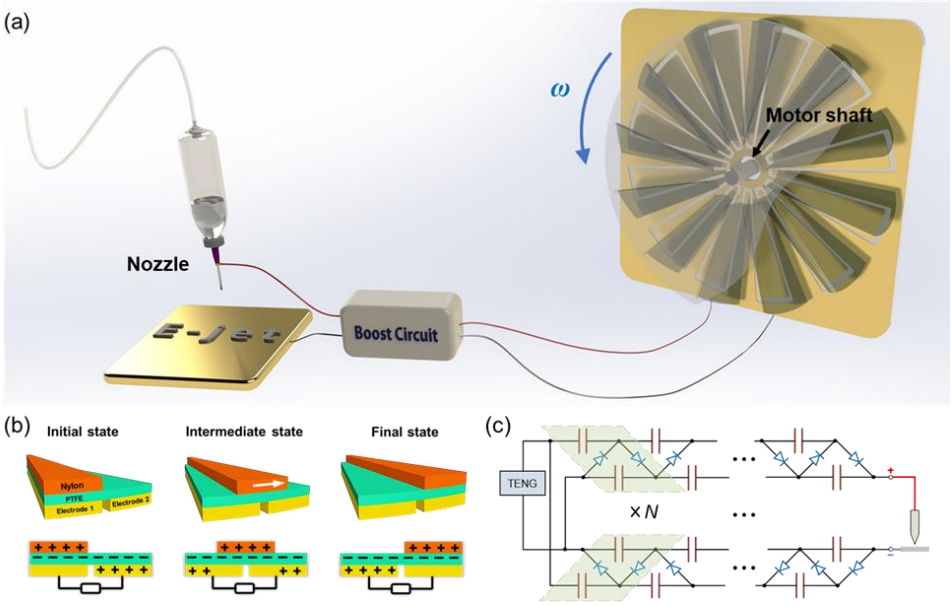


**Figure 51. TENG-driven e-jet process.** (a) Schematic of the proposed process. (b) Working mechanism of the sliding freestanding TENG. (c) Equivalent electrical circuit model of the boost circuit. Reproduced with permission.[225] Copyright 2019, Wiley-VCH.

The nozzle-to-substrate distance is critical in the e-jet printing process. As shown in Figure 52a with a nozzle size of 340 μm, when the distance was too small (~0.5 mm), the ink would deform and contact the substrate without droplet formation; when the distance was too large (~2.5 mm), the jetted droplets would breakup and thus a spray, rather than a series of drops, would be collected on the substrate, which is exactly the case for electrospraying.[226] Only with a proper distance (~1 mm), a stable stream of ink droplets could be ejected onto the substrate to achieve desirable printing resolution. To further validate the e-jet process driven by TENG, its droplet formation and ejection process was recorded using a high-speed camera (nac Image Technology, MEMRECAM HX-7), with one complete cycle shown as in Figure 52b and Figure 52c for a motor rotation speed of

600 RPM and 1000 RPM respectively. The nozzle-to-substrate distance (~5 mm) was larger than that used in normal printing so that the camera lens could find a good focus position, and 5 boost units and a nozzle size of 600 μm were used for the recording. During the e-jet process, the ink meniscus at the nozzle tip expands from spherical to conical shape and then contracts back to spherical shape periodically due to the electric field. A complete cycle can be divided into four phases, liquid accumulation, cone formation, droplet ejection and relaxation.[218] During the liquid accumulation phase (Figure 52b&c, i), ink accumulates at the nozzle tip and the meniscus is spherical with the surface tension as the dominant stress. Subsequently (Figure 52b&c, ii-iv), charges in the ink starts to accumulate at the meniscus surface under the electric field and the resulted Maxwell stress from coulombic repulsion transforms the meniscus into a conical shape. Once the Maxwell stress exceeds the surface tension (Figure 52b&c, v-viii), the radius of curvature at the cone apex reaches its minimum, and some charged ink liquid at the apex is ejected from the nozzle towards the collecting substrate and turns in to a droplet during the fall, resulting in a decrease in cone volume and charge amount. After the droplet ejection (Figure 52b&c, ix-x), the surface tension becomes dominant again and the meniscus retracts back to the spherical shape quickly, which is followed by the next cycle. This matches well with the droplet generation and ejection process reported in previous literature where a conventional DC HV is applied.[218, 219]

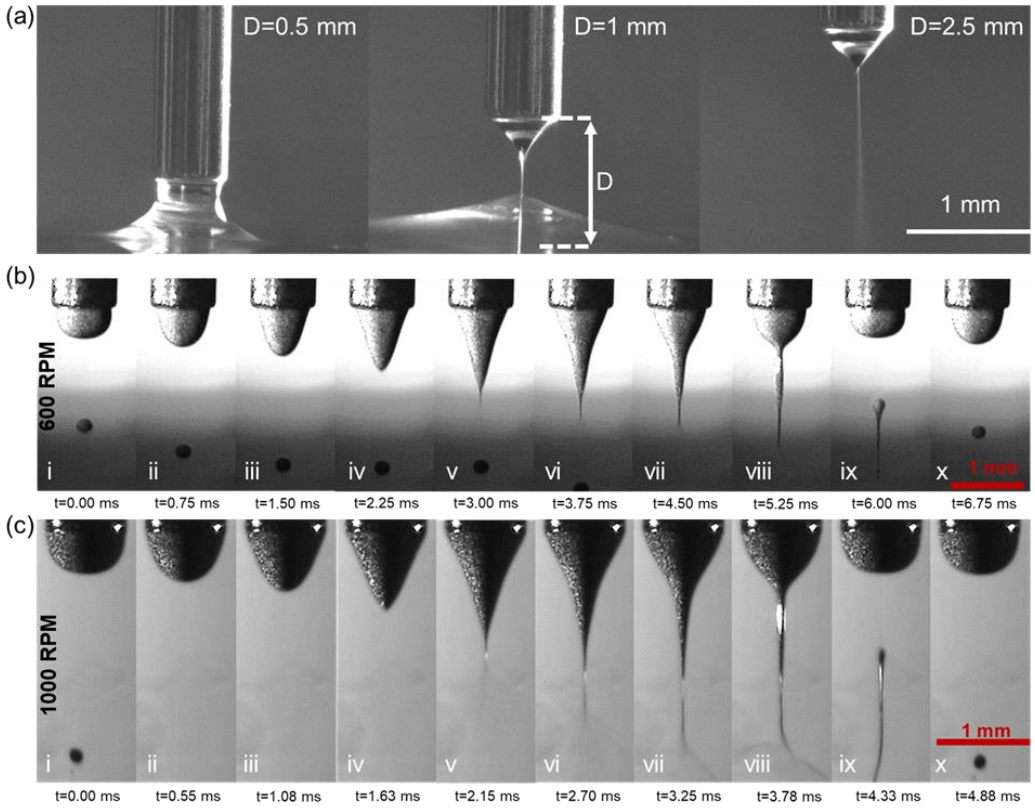


**Figure 52. Photographs of TENG-driven e-jet process.** (a) The significance of nozzle-to-substrate distance on achieving stable ink jetting. (b-c) Droplet formation and ejection process recorded by high-speed camera with a motor rotation speed of 600 RPM (b) and 1000 RPM (c). Reproduced with permission.[225] Copyright 2019, Wiley-VCH.

### *5.2.2 Performance of TENG-Driven E-Jet Printing*

To study the effects of printing parameters on our TENG-driven e-jet process, we printed line and dot features at various nozzle moving speeds and nozzle sizes. For nozzle sizes of 160 μm and 210 μm, a nozzle-to-substrate distance of 0.75 mm and 3 boost units were used; for 410 μm and 600 μm, 1.5 mm and 4 boost units were used. The feature images are presented in Figure 53 for a motor rotation speed of 600 RPM and 1000 RPM, and the results are summarized in Figure 54. Several observations can be made as follows. For one specific nozzle size, the width of the printed line feature decreased with the nozzle

moving speed due to the reduced overlapping between successive droplets, until discrete dot features were printed. At a nozzle moving speed of 15 cm/s, printed feature sizes smaller than the nozzle sizes were achieved for all, which clearly demonstrates the potential of high-resolution printing of our TENG-driven e-jet setup. The plots in Figure 54 also show a monotonically increasing correlation between the nozzle size and feature size as expected, regardless of the feature being line or dot.

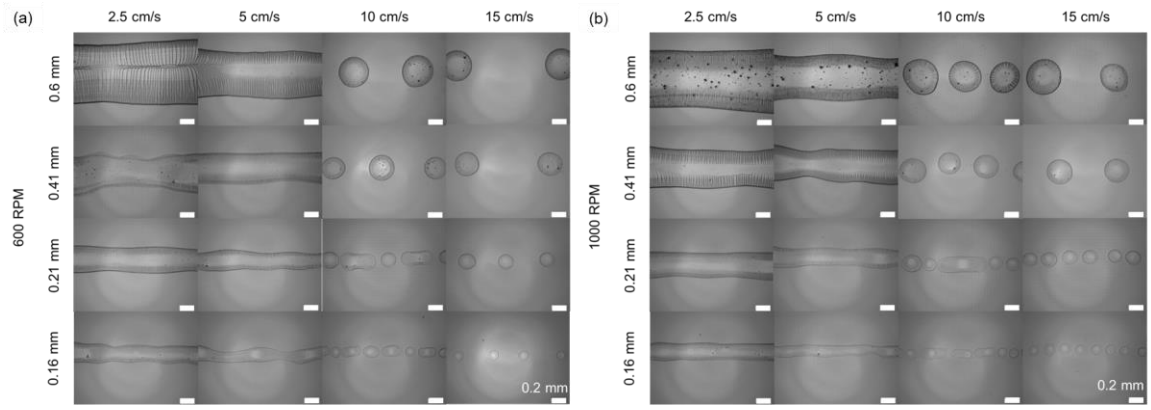


**Figure 53. Printed features at different nozzle sizes and moving speeds with different motor rotation speeds.** (a) 600 RPM. (b) 1000 RPM. Reproduced with permission.[225] Copyright 2019, Wiley-VCH.

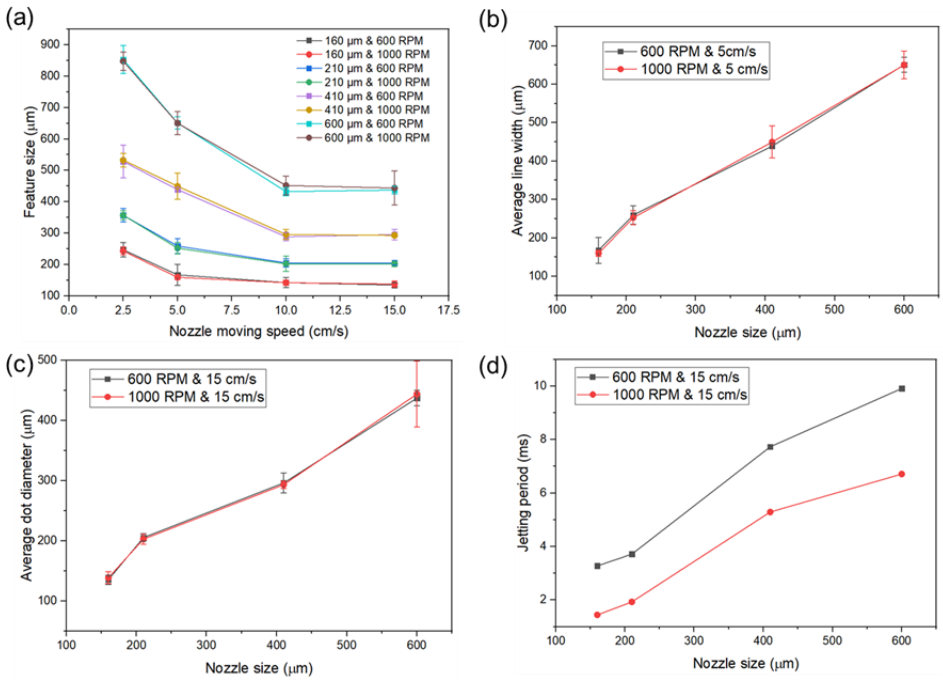


**Figure 54. Effects of nozzle moving speed and nozzle size on printed features.** (a) Printed feature size with respect to different nozzle moving speed, nozzle size and motor rotation speed. (b) Printed line width at a constant nozzle moving speed of 5 cm/s with various nozzle sizes and motor rotation speeds. (c) Printed dot diameter at a constant nozzle moving speed of 15 cm/s with various nozzle sizes and motor rotation speeds. (d) Droplet jetting period with respect to different motor rotation speed. Reproduced with permission.[225] Copyright 2019, Wiley-VCH.

Figure 54(a-c) shows that the change in motor rotation speed did not pose significant influence on the feature size in our experiments. However, one thing worth noting is that with all other parameters (ink, nozzle size, nozzle-to-substrate distance, nozzle moving speed, etc.) kept the same, the increase in motor rotation speed and thus TENG operation/voltage frequency decreased the jetting period, or increased the jetting frequency, which is supported by both the plot in Figure 54d and the images in Figure 52. In previous literature about pulsed e-jet printing, such dependence of jetting frequency on the voltage frequency is generally attributed to the time interval between two successive pulses since one voltage pulse only ejects one droplet.[227-229] Two critical differences,

however, existed in our setup. Firstly, the TENG was operated in a continuous rotation mode and no time interval existed between two voltage cycles. Secondly, the motor rotation speed of 600 RPM and 1000 RPM corresponds to a voltage frequency of 120 Hz and 200 Hz, i.e., a voltage cycle of 8.3 ms and 5 ms, respectively. In such cases, for nozzle sizes of 160 μm and 210 μm, more than one droplet was jetted within one TENG operation or voltage cycle. With a conventional power supply, a single voltage cycle with longer duration in the HV region gives more time for droplet ejection, and thus should have more droplets, which is contradictory to our experimental results. This is because of the unique characteristic of TENG, a power source with limited charge transfer. The output voltage of TENG when connected to a load is determined by the amount of charge transfer during the operation cycle and can be expressed as

$$V = -\frac{1}{C(z)} \times Q + V_{OC}(z) \tag{22}$$

where $C$, $z$, $Q$ and $V_{oc}$ are the equivalent capacitance, displacement, charge transfer and open-circuit voltage respectively.[19] Meanwhile, it is the charge accumulation at the meniscus, rather the applied voltage, that directly triggers and is the root cause of the droplet ejection.[218] Therefore, it makes more sense to explain the results from the perspective of charge transfer. The maximum charge transfer per TENG operation cycle is independent of the operation frequency but the rate of charge transfer depends on the frequency. With the boost circuit, non-ideal capacitors and diodes would consume more charges when the operation cycle is longer, resulting in less amount that can be used for the jetting process. Consequently, the more rapidly the TENG rotates, the more quickly the charges accumulate at the liquid meniscus, and thus the faster the droplets jet.

To better evaluate the performance of the TENG-driven e-jet printing process, a comparison study with the DC-driven process was conducted. With the same experimental setup, a DC voltage of 2000 V and a nozzle-to-substrate distance of 1 mm was applied to achieve stable ink jetting, whose printing results using different nozzles and moving speeds are presented in Figure 55. Based on the comparison of Figure 55a and Figure 53, the DC-driven jetting process produced all line features even at the highest moving speed of our robotic arm (15 cm/s), while the TENG-driven jetting process could generate dot features at smaller moving speeds (10 cm/s). This indicates that a DC power supply, compared to our TENG, would give a much higher droplet jetting frequency. It could also be expected that by increasing the operation frequency of TENG, the printing results would become more similar with the DC-driven results. The motor rotation speed, i.e. TENG operation frequency, provides a facile method of controlling the droplet jetting frequency and the printed feature pattern (line or dot), especially in the case where nozzle moving speed is limited. A more quantitative comparison of the printed feature sizes (Figure 55b and Figure 54a) showed that the printed resolution using TENG is comparable with that using a DC power supply. Therefore, the TENG-driven e-jet printing process offers a promising alternative to conventional ones, not only with comparable resolution, but also with additional merits including low cost, extra safety, better feature controllability at low printing speeds, etc.

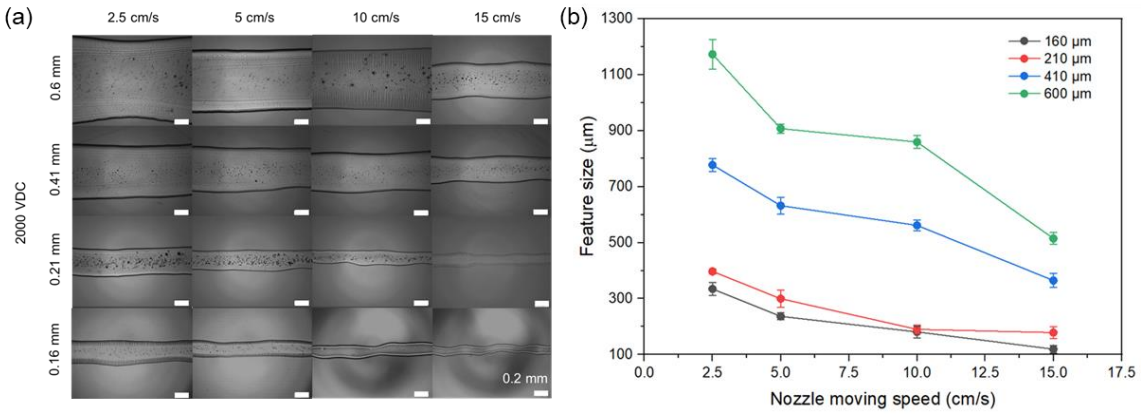


**Figure 55. Printed features at different nozzle sizes and moving speeds with a DC voltage of 2000 V.** (a) Photographs. (b) Summarized feature size. Reproduced with permission.[225] Copyright 2019, Wiley-VCH.

### *5.2.3 Demonstrations using TENG-Driven E-Jet Printing*

E-jet printing is commonly used for graphic arts,[219] so we firstly tried our TENG-driven setup for art printing. A pair of gears was printed as in Figure 56a. Printing of electrical components were also realized using our setup. Figure 56b shows two printed S-shaped conductive interconnects that could deliver the electric power from a battery to a LED for lighting. In Figure 56c, we printed four conductive arrow patterns on a note paper. By integration with a MakeyMakey circuit, the patterns were successfully used as a sensing array and functioned as a directional keypad for controlling the gameplay of a virtual piano.

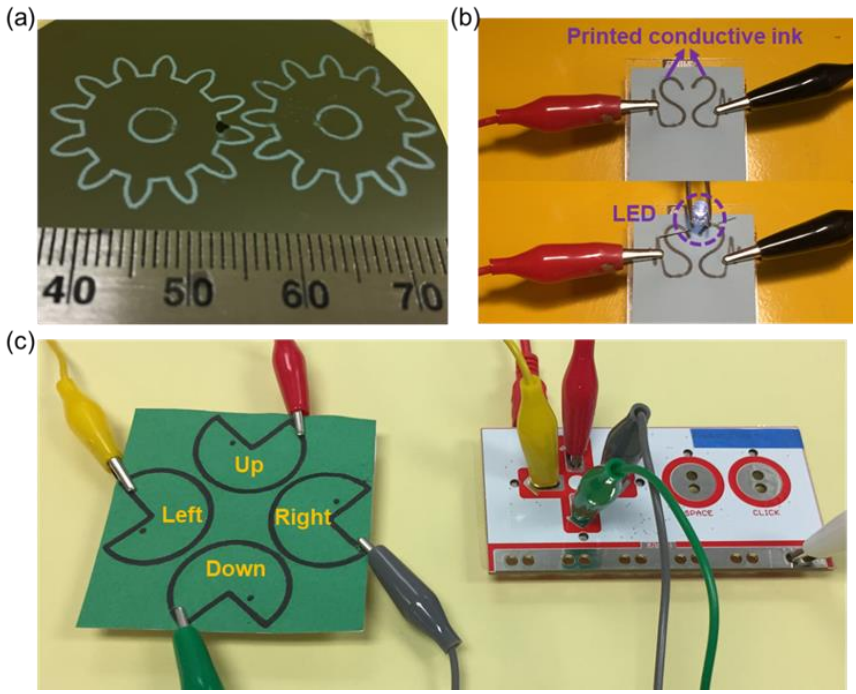


**Figure 56. Demonstrations using the TENG-driven e-jet setup.** (a) Printed gear pattern. (b) Printed electric interconnect. (c) Printed sensor array for game control. Reproduced with permission.[225] Copyright 2019, Wiley-VCH.

In this work, we explored the application of TENG in the field of printed electronics for the first time. A RF-TENG, together with a simple voltage boost circuit, was demonstrated to drive the e-jet printing process. The corresponding droplet formation and ejection process was examined using high-speed photography, and effects of various printing parameters, such as nozzle size and moving speed, nozzle-to-substrate distance and motor rotation frequency, were studied. Results suggested that a configuration of smaller nozzle size, large nozzle moving speed and optimal nozzle-to-substrate distance would yields smaller features. High resolution printing with feature size smaller than nozzle size was achieved using our TENG-driven e-jet setup. Owing to the charge-dominating output characteristic of TENG, the droplet jetting frequency could be controlled by the TENG operation frequency. Several demonstrations, such as the printing

of graphic art and the fabrication of conductive interconnects and touch sensors, were conducted to validate the potential of practical application of the TENG-driven e-jet printing process. This works not only expands the application field of TENG, but also provides an alternative way of driving the high-resolution e-jet printing with unprecedented merits of safety, cost-effectiveness, and controllability.

### *5.2.4 Experimental Methods*

#### 5.2.4.1 TENG Fabrication

The acrylic substrates (1/8 inch thick) of the stator and rotator were prepared using laser cutting. Two Al films were pasted onto the inner and outer sections of the stator to function as the electrodes, and then covered by a PTFE film (200 μm thick) as one triboelectric material. The prepared nylon films (50 μm thick) were partially inserted into and fixed on the slits of the rotator. All nylon films were bended in one direction so that they would not be twisted when sweeping across the stator clockwise. The rotator was fixed on the shaft of a rotating motor (Oriental Motor, BLFM230-A, 30 W & 0.6 kg) for motion control and the distance between the rotator and stator was adjusted so that the free part of a nylon film can cover about one electrode sector during rotation. The open-circuit voltage of the TENG was measured using a Keithley 6514 electrometer and a resistance-based voltage divider.

#### 5.2.4.2 E-Jet Printing

To perform the e-jet printing, the setup given in Figure 1a was prepared. The positive output of the boost circuit was attached to liquid dispensing nozzles (Brostown)

having different diameters. The neutral output of the boost circuit was attached to a conductive silicon wafer (University Wafers 2270). The nozzle was attached to a syringe barrel (Nordson EFD) and the pressure inside the syringe barrel was controlled with a pneumatic dispenser (Nordson EFD, Ultimus III). A charge coupled device (CCD) camera (Sentech STC, MB33USB) was used to observe the nozzle tip and meniscus formation. The printing head, which consists of the dispensing nozzle, syringe barrel and pneumatic dispenser, was placed on the end effector of a customized 3D printer (Geeetech-Rostock 301) and its motion as well as the moving speed was controlled by prepared g-codes. For a typical e-jet printing job, firstly, the vacuum level inside the printing head was adjusted so that a spherical meniscus could be observed at the nozzle tip without ink dropping. Following that, the printing head was moved to the home position at a distance of 150 mm from the substrate. In this position, due to the high distance between the substrate and nozzle tip, jetting would not start even if the TENG device was in operation. Afterwards, the TENG device was started and the printing head was lowered to adjust the distance between the substrate and nozzle tip (~ 0.5 – 3 mm). Once the printing head moved to the suitable position and jetting was observed through the CCD camera, we immediately started the printing job using the previously prepared g-codes. Except the Pac-Man patterns which used an aqueous carbon nanotube ink (Chasm Advanced Materials, AC100), all other printing jobs were completed with an Ag nanoparticles ink (Genes Ink, Smart Ink S-CS01130).

#### 5.2.4.3 Gameplay Demonstration

For this demonstration, we used a commercial off-the-shelf electronic board from MakeyMakey, which could transform a variety of common objects into a user input device.

It has the functions of arrow keys and space button from the keyboard and left click function from the mouse. In our experiment, we e-jet printed four arrow patterns on a piece of note paper using an aqueous carbon nanotube ink. We connected these patterns to the ports for arrow keys on the MakeyMakey board and grounded the board with one hand of the user using the white alligator clip, as shown in Figure 56c. As the user touched the printed patterns using the other hand, corresponding activation signals for the arrow keys were sent to the computer, and the user was able to play the Pac-Man game with the e-jet printed sensing array.

## 5.3 Field Emission of Electrons Powered by TENG

Field emission of electrons has been studied for over one century, which is related to the early research about electrons. [230-233] This phenomenon is now intensively involved in the technologies that require electron emissions, including but not limited to electron microscopy,[234] e-beam lithography,[235] field-emission display,[236] and nanoelectronics. In recent decades, with the rapid development of nanotechnology, various nanostructured materials have been demonstrated for field emission through their field-enhancing effect at sharp tips and corners.[237-243] However, to satisfy the high electric field required for field emission, HV of at least 100 V is usually applied, which greatly limits the applications of field emission due to the high cost of HV instrument, limited controllability, stability concerns, and portability issues.

In this work, the TENG-powered tribo-field emission was presented for the first time. The emitter was fabricated by zinc oxide (ZnO) NW arrays grown on highly-doped Si substrates. Field emissions driven by commercial HV source and TENG were

demonstrated on the fabricated emitter, with the electric outputs carefully characterized. As driven by TENG, the voltage and the charge amount per cycle can be controlled precisely through the choice of the operation parameters, which can produce emission of electrons “as demanded”. The limited amount of charge delivered by TENG can also prevent the ZnO nanostructures from exfoliating off from the substrate, which enhances the stability of the system. A unidirectional continuous field emission was achieved through rectifying circuits. The tribo-field emission display was demonstrated by a modified commercial cathode ray tube (CRT), with more than 100 mins illumination achieved by only one sliding motion. Such results open a new era for the development of cost-effective, controllable, stable, and portable field-emission systems.

### *5.3.1 Tribo-Field Emission*

The setup for the field emission measurement is shown in Figure 57a. The emitter was fabricated by two pieces of highly-doped conductive Si substrates with grown ZnO NW arrays facing to each other. These ZnO NWs were hydrothermally grown on the pre-deposited ZnO film on the two Si substrates, each with an effective area of 1 cm × 1 cm. Through SEM, these NWs were characterized with < 50 nm in the tip thickness and 1-2 μm in length (Figure 57b inset). Kapton double-side tapes with thickness of 25 μm were used as spacers to separate the two substrates. This emitter was placed in a vacuum chamber with a pressure of $< 10^{-6}$ torr. TENG or commercially available DC HV source was connected to the backsides of the Si substrates to supply the HV required. The voltage and current/charge transfer were measured by electrometers separately.

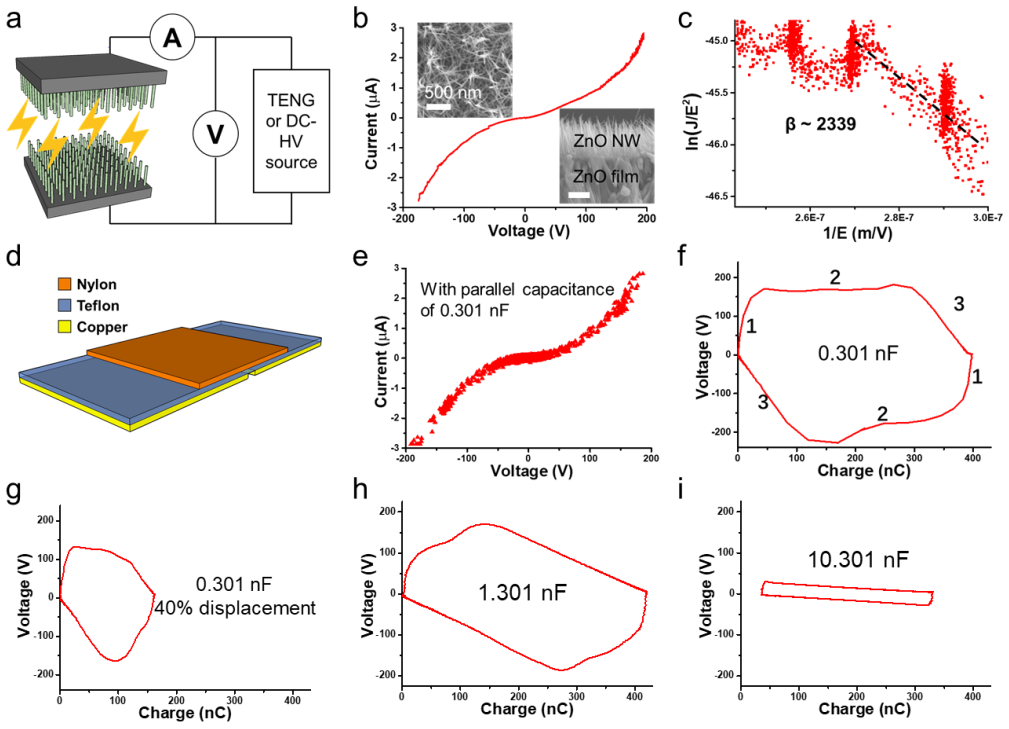


**Figure 57. Tribo-field emission.** (a) The schematic diagram showing the emitter, the power source and the measurement circuit. (b) The measured I-V curve with SEM pictures of ZnO NWs in top view (*top left*) and cross-sectional view (*bottom right*) as insets. Scale bars: 500 nm. (c) The $\ln(J/E^2)$-$1/E$ curve showing the slope and the $\beta$ value. (d) Schematic of the fabricated TENG. (e) The *V-I* curves of the tribo-field emission with parallel capacitance of 0.301 nF. (f-i) The *V-Q* plots with parallel capacitance of (f) 0.301 nF, (g) 0.301 nF and only ~40% displacement, (h) 1.301 nF, and (i) 10.301 nF. Reproduced with permission.[216] Copyright 2018, Elsevier.

By using the DC-HV power source, the measured voltage-current (*V-I*) curve of the fabricated emitter is shown in Figure 57b. The emission characteristics can be explained by the Fowler–Nordheim equation as below:[231, 244, 245]

$$J = (A\beta^2 E^2 / \varphi)\exp(-B\varphi^{3/2} / \beta E) \tag{23}$$

here $\varphi \sim 5.3$ eV is the emission potential barrier of ZnO,[244, 246-248] $A = 1.56 \times 10^{-10}$ A·V$^{-2}$eV and B = $6.83 \times 10^3$ V·eV$^{-3/2}$μm$^{-1}$ are two constants, and $\beta$ is the field enhancement factor

brought by the nanostructured surface. Based on this equation, the measured $\ln(J/E^2) - 1/E$ curve is presented in Figure 57c and $\beta \sim 2339$ can be obtained. This $\beta$ value is a little bit higher than previous reported values,[244, 246-248] which might be attributed to the field-enhancing effect brought by the sharp tips of the grown NWs as shown in insets of Figure 57b.[249] These results validate the successful field emission from our fabricated ZnO NW based emitter.

To demonstrate the tribo-field emission, a freestanding sliding (FS) mode TENG was fabricated as shown in Figure 57d. The operation mechanism of the FS-TENG has been reported in previous literature,[8, 21, 208, 250] with the nylon (slider, usually 8 cm × 8 cm) and Teflon (stator) film as the positive and negative triboelectric surfaces, respectively. This TENG was used to power the tribo-field emission process. By connecting TENG to the emitter, with the voltage electrometer having a capacitance of 0.301 nF in parallel, the *I-V* curve as triggered by the TENG was measured and consistent with those measured using the DC-HV power source (Figure 57e). Then the *V-Q* plot, which was proposed previously for TENG analysis and optimizations,[72, 96] was utilized to understand the operation cycle. As shown in Figure 57f, in each half-cycle of the operation, there are three stages as marked by the numbers: in Step 1, the TENG charges the emitter like a capacitor, and there is negligible current leakage; in Step 2, when the voltage is over ~100 V, the emission current becomes much larger, which induces a voltage plateau of about ~200 V until the fully displacement of the slider being reached in TENG; in Step 3, the charge is fully released with the decreasing voltage and current. The other half-cycle operates similarly, with the negative voltage and the opposite charge transfer direction. The total transferred charge was about 400 nC.

Through the controlled operation of the TENG, the emission voltage and the charge transfer per cycle can be tuned. By operating TENG with only ~40% of the original displacement, the total charge transfer was only ~160 nC and the maximum absolute voltage could only achieve ~150 V (Figure 57g). Through this method, the emission voltage and the charge transfer can be lowered simultaneously. By using additional capacitors in parallel, the total charge transfer keeps the same but the emission voltage decreases greatly. With an additional 1 nF capacitor in parallel, the maximum absolute voltage became about 160-180 V, while the charge transfer was maintained at about 400 nC (Figure 57h). However, if an additional 10 nF capacitor was connected, the voltage could only reach ~30 V, which is not high enough to power the effective field emission (Figure 57i).

### *5.3.2 Enhanced Safety of Using TENG as HV Source*

Various emission materials/structures have been reported to be destroyed during the field emission under HV,[251, 252] which affects the long-term stability. As tested in our study, by gradually increasing the voltage provided by the DC-HV source to be ~280 V, the current suddenly increased with huge oscillations, as shown in Figure 58a. And then the voltage across the emitter could not be maintained at the set point. This indicates that the original structure inside the emitter might be destroyed by the HV. As observed in SEM in the insets of Figure 58a, some parts of the ZnO film with NW structures were exfoliated from the Si substrates, which made the two substrates electrically shorted at certain points.

Since the charge transfer per cycle is limited for TENG, the HV produced by TENG can be safer for instrument.[208] A partial voltage measurement method was used to estimate

the peak voltage achieved here (Figure 58b). With a larger sliding area of 9.5 cm × 10 cm, the peak voltage generated by the TENG could be pushed to be over 3000 V (Figure 58b), and the measured *V-I* curve (Figure 58c) was still consistent with the previously measured ones. This result indicates that the emitter was kept intact under the TENG-HV supply. In fact, even in the worst situation that a short circuit occurs, the safety would not be a concern for systems driven by TENG given its limited charge density.[150]

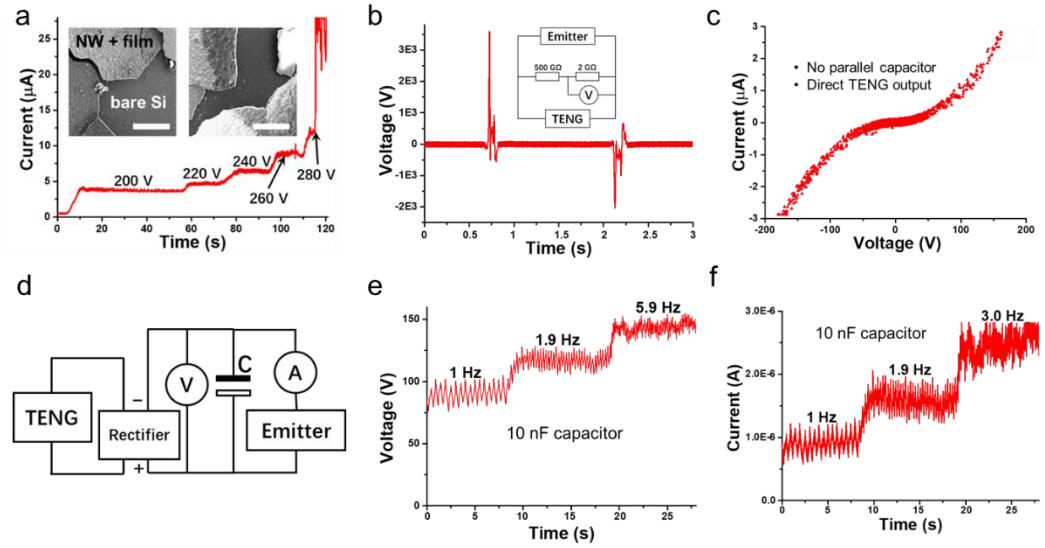


**Figure 58. Merits of using TENG as HV source for field emission of electrons.** (a-c) The safety test of the emitter under DC-HV and the TENG-HV. (a) The current through the emitter with gradually increased DC voltage until ~280 V. The insets show the exfoliated ZnO film with NWs after test. Scale bars: 100 μm. (b) The measurement of TENG-HV through a partial voltage measurement circuit. (c) The measured *V-I* curve after TENG-HV test, which is consistent with the previously measured curves. (d-f) Continuous unidirectional tribo-field emission output. (d) Equivalent electrical circuits. (e) voltage and (f) current output achieved with a 10 nF capacitor under various frequencies. Reproduced with permission.[216] Copyright 2018, Elsevier.

### *5.3.3 Controllability of Using TENG as HV Source*

Given that a continuous unidirectional output of field emission is usually preferred for most applications, relatively stable voltage for tribo-field emission is achieved via a

rationally designed circuit. The output of the TENG is firstly connected to a capacitor through a full-wave bridge rectifier, and then the emitter is connected in parallel with the capacitor (Figure 58d). Therefore, the capacitor can supply a stable voltage output for the emitter, at the same time the charge consumption in the capacitor can be replenished by the TENG. One electrometer is connected in parallel to measure the voltage of the emitter, and the other one is connected in series to measure the current through the emitter. With a capacitor of 10 nC, the measured voltage and current are shown in Figure 58e and Figure 58f, respectively, with the TENG operation frequencies of 1 Hz, 1.9 Hz, and 3 Hz. A more stable output can be achieved by increasing the capacitance in parallel. Hence, through this method, the unidirectional continuous tribo-field emission with over 100 V in voltage and several μA in current is achieved, and the output magnitude can be tuned by the operation frequency.

### *5.3.4 Application of TENG to Power A Commercial CRT*

To demonstrate possible application of the tribo-field emission, we used TENG to power the field emission in a commercial CRT for display purpose. The schematic diagram of this CRT is shown in Figure 59a. There are three voltage inputs required for this CRT: the heating voltage ($V_H$) of 6-8 V is used to heat the filament; the wehnelt/focus voltage ($V_W$) of 10 V is for the focus adjustment of the electron beam; and the anode voltage ($V_A$) of 200-230 V is used for field emission of the electrons. The emitted electrons hit the inner surface with the fluorescent coating, and the interacted spot is illuminated to be green. Here $V_H$ and $V_W$ can be easily supplied by batteries, and the most difficult part is the HV power supply for $V_A$, which is provided by TENG in our experiment. As we demonstrated, the emission could be turned on and off by simply performing one sliding motion

(corresponding to a half cycle) back and forth. The voltage after triggering the tribo-field emission was measured as only about ~210 V (Figure 59c), which might be related to the threshold voltage set by the protection circuit inside the CRT. After a fully displacement of the slider in TENG to turn the emission on, through an instantaneously connected electrometer in short-circuit condition, the total charge release was measured as ~45 nC (Figure 59d inset). Therefore, the capacitance of this emitter was estimated as ~0.21 nF. At the same time, the emission current was measured to be only about 2.5-3.0 pA (Figure 59d), which means the electron emission could last for more than ~ 100 min until the voltage is below the threshold emission voltage. These results demonstrate a possible portable solution of CRT based on tribo-field emission for long-lasting-time display with minimum power consumption.

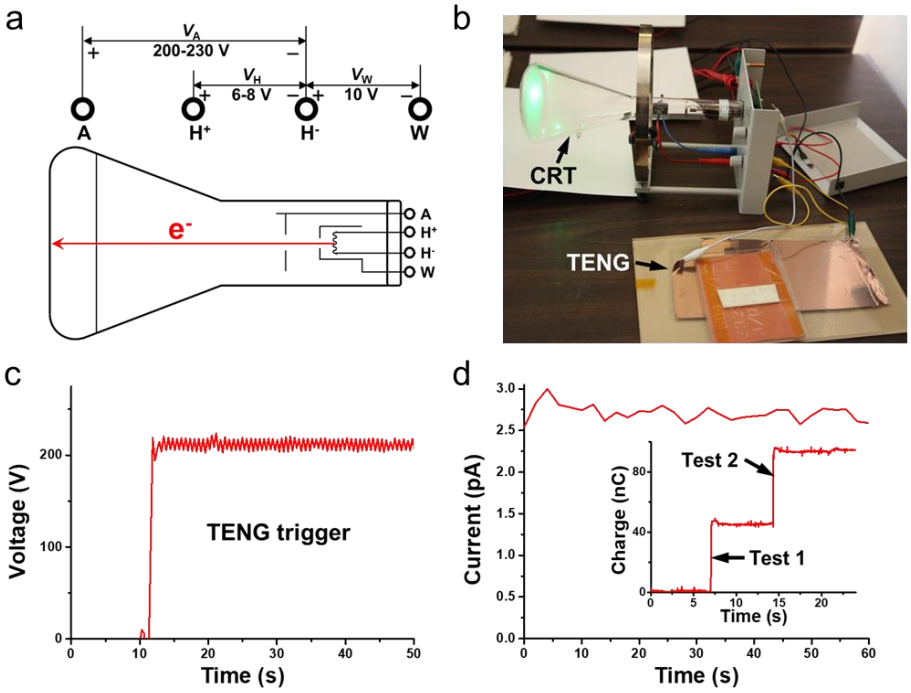


**Figure 59. The tribo-field emission enabled CRT display.** (a) The schematic diagram of the CRT with required power supply. (b) A photo showing successful display enabled by

TENG. (c) The measured voltage before and after the sliding motion. (d) The measured emission current and the measured total charge release (twice) as inset. Reproduced with permission.[216] Copyright 2018, Elsevier.

In summary, TENG has been demonstrated to supply HV to enable the tribo-field emission of electrons. The fabricated ZnO NW array based emitter is powered by TENG, with controllable voltage and charge transfer achieved. This approach is demonstrated to be more favorable than the DC-HV source in terms of emitter protection. The unidirectional continuous emission is enabled through rectifying circuits, with the emission voltage tunable by the operation frequency. The tribo-field emission is also demonstrated in a CRT for a portable, low-power, and long-lasting-time display. The tribo-field emission represents a potential solution for the next-generation low-cost field emission instrument with enhanced stability, controllability and portability.

### *5.3.5 Experimental Methods*

#### 5.3.5.1 ZnO NW Array Growth

First, ZnO film as the seed layer was directly deposited on the highly-doped silicon wafer (p-type (100), B doped, 1−10 Ω•cm, from University Wafer) by radio frequency magnetron sputtering (PVD 75, from Kurt. J. Lesker Company) at the power of 100 W with the chamber pressure of 8 mTorr for 30 min. Then, the ZnO seed layer coated silicon wafer substrate was then placed into a mixed nutrient solution containing 25 mM zinc acetate (from Alfa Aesar) and 25 mM hexamethylenetetramine (HMTA) (from Alfa Aesar) for ZnO NW growth at 95 $^{o}$C for 2 h in an oven. After cooling, the obtained sample was cleaned with deionized water and dried at 70 °C.

#### 5.3.5.2 Fabrication of Emitter for Field Emission

One piece of Si substrate is attached with double-side Kapton tape on the ZnO NW side as the spacer, confining a 1 cm × 1 cm effective area. The other piece of Si substrate is attached with the ZnO NW side facing inside. The back sides of Si substrates are coated with silver paste and connected out as electrodes. To remove possible gases from the tape, the samples were left in the ultra-high vacuum for more than one day before measurements.

#### 5.3.5.3 Fabrication of FS-TENG

The Teflon (FEP) film is firstly deposited with Cu film using PVD 75 system. A narrow tape is used as the mask to separate the deposited area into two parts as electrodes, each with area of 8.5 cm × 10 cm. The Cu side of this Teflon film is attached on an acrylic board as the stator. Two sliders are fabricated by attaching nylon films on PU foams and acrylic boards, with areas of 8 cm × 8 cm and 9.5 cm × 10 cm. The materials are all purchased from McMasters

#### 5.3.5.4 Characterization Methods

The motions in most of experiments are triggered by hands, except the $V_{OC}$ and $Q_{SC}$ tests are conducted through a linear motor. The electrical measurements are mostly conducted by Keithley 6514 electrometers, except the ~pA level current in Figure 5 is measured by a Keithley 4200 electrometer system. The commercial HV source is 3B Scientific U33000-230 DC Power Supply (0-500 V) purchased from Amazon. The CRT is 3B Scientific U8481350 Training Oscilloscope purchased from Amazon, with the function wave generator disconnected from the circuits to avoid consumption of charges.

# CHAPTER 6. CONCLUSION

In this dissertation, my major research achievements as a Ph.D. student at Georgia Tech have been presented. One major goal of my research is to develop high performance TENG with desired merits including higher power density and energy efficiency, better mechanical property, and versatile functionality. The other major goal is to find novel applications of TENG that can provide affordable, safe, and convenient solutions for energy challenges in IoT. In this chapter, I will briefly summarize my achievements and propose a roadmap of TENG research that provides a guideline for future endeavors in the field.

## 6.1 High Performance TENG

High performance TENG with targeted merits including higher power density, better mechanical property, and versatile functionality, has been pursued. A method for increasing triboelectric charge density and thus power density by coupling surface polarization from triboelectrification and hysteretic dielectric polarization from ferroelectric material in vacuum ($P \sim 10^{-6}$ torr) was reported. Without the constraint of air breakdown, a record-high triboelectric charge density of $1003\ \mu C/m^2$, which is one magnitude higher than previously reported values and close to the limit of dielectric breakdown, has been attained. The concept of spring-based mechanical amplifier was introduced into the emerging field of TENG to improve its performance in harvesting low-frequency vibration energy, and the resulted features of amplified frequency and displacement achieved a performance boost up to 10 times in terms of average output power, which is of great importance for future progress towards the highly anticipated

prospect of large-scale blue energy. A new type of highly stretchable TENG by using the traditional kirigami patterns, whose stretchability originates from the designed structures instead of constituent materials, was proposed. The proposed method enables stretchable TENG to be made from materials without intrinsic stretchability, such as paper, PTFE, PET and Kapton, and thus is very versatile. It presents an important progress of TENG for applications in stretchable electronics and verifies promising applications of traditional kirigami in both power generation and self-powered sensing. A sunlight-triggerable transient TENG, whose degradation is not restricted to aqueous environment and can be achieved within several minutes even under winter sunlight, was developed. The work not only broadens the applicability of TENG as transient power sources and sensors, but also expands the use of transient functional polymers towards advanced energy and sensing applications.

## 6.2 TENG for Self-Powered Systems

Application of TENG as micro power sources for biomedical treatment and wearable power band has been explored. A self-powered wearable iontophoretic TDD system based on biomechanical motion sensing and energy harvesting using TENG was developed. The feasibility of the proposed system was successfully demonstrated on pigskins using dyes as the simulated drugs. It enables electrically-assisted TDD with closed-loop sensation and therapy, and promotes TENG-based self-powered systems towards advanced biomedical treatment in the era of IoT. Also, a self-charging power unit by integrating, for the first time, MXene-based MSCs with a soft and flexible triboelectric nanogenerator was developed. The power system could be worn as a wristband and continuously charged by regular human motion (~5 Hz) without significant current

leakage. The strategy shows that TENG is versatile and can be readily integrated with energy storage devices, which opens new possibilities in wearable/implantable sensor networks.

## 6.3 TENG for Active Sensing

Application of TENG as active sensors for advanced HMI has been explored. A two-factor, keystroke dynamics-based security system consisting of a rationally designed TENG-based keypad and an SVM-based software platform, was developed. It was capable of authenticating and even precisely identifying users through their unique typing behaviors, with an accuracy up to 98.7%. The promising application of this novel system in the financial and computing industry can push cyber security to a new level, where leaked passwords would possibly be of no concern. Furthermore, a self-powered, TENG-driven OWC with the capability of wireless control, sensing and even authentication was developed. The concept of self-powered OWC was proposed for the first time, and TENG-based sensing devices were integrated with a LED array to achieve a wireless transmitter that could convey the information associated with mechanical stimuli without additional electrical power supply. The concept and results may greatly broaden the application of IoT through the integration of OWC and TENG.

## 6.4 TENG for HV Instruments

Application of TENG as cost-effective HV power sources with enhanced safety and portability has been explored. The application of TENG in the field of printed electronics was demonstrated for the first time by using it to drive the e-jet printing process. The TENG-driven e-jet printing setup was able to achieve feature sizes smaller than the nozzle

diameters, with a minimum feature size of 135 μm using a nozzle diameter of 160 μm in unoptimized experiments. With the performance comparable to that using a commercial DC HV power source, the setup provides an alternative way of driving the high-resolution e-jet printing with unprecedented merits of safety, cost-effectiveness, and controllability. Moreover, the HV of TENG has been demonstrated to enable the tribo-field emission of electrons. The voltage and charge amount per cycle from TENG can be controlled precisely through operation parameters, which enables on-demand emission of electrons. The limited amount of charge delivered by TENG can also protect the emitter device from electric shock. A unidirectional continuous field emission was achieved through rectifying circuits. The tribo-field emission represents a potential solution for the next-generation low-cost field emission instrument with enhanced stability, controllability and portability.

## 6.5 Future Work

To guide the future endeavour in the field of TENG, a roadmap is proposed as in Figure 16, which identifies key priority directions and key challenges for TENG. Each field is likely to experience four stages, but the pace at which each stage proceeds may vary from field to field. First, design innovation is required in order to design the best TENG structure for the specific purposes of conjoining the four working modes. Secondly, for the specific design, the most suitable materials are chosen for achieving the maximized performance with consideration of the working environment and durability. Thirdly, system integration, prototype testing, and product development are essential and possibly will take longer for TENG to reach commercialization. Lastly, an industry based on TENGs and related technologies is anticipated for its vast applications and across many fields.

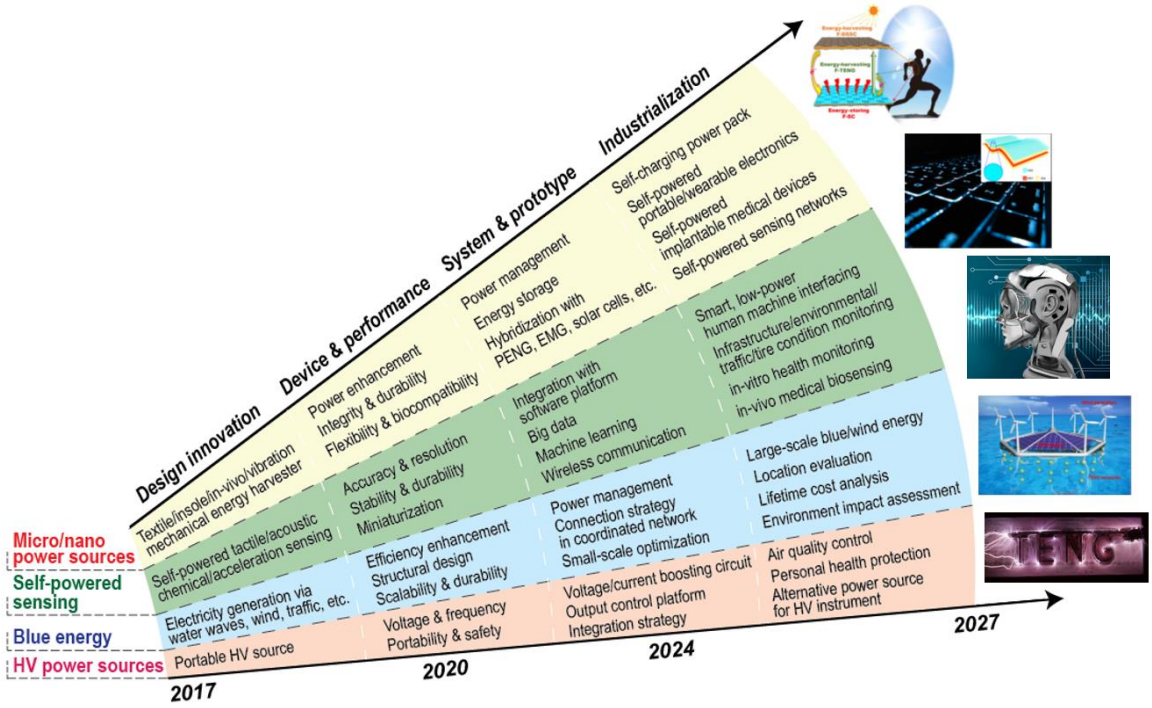


**Figure 60. Roadmap of TENG development from 2017 to 2027.** Reproduced under the terms of the CC-BY-NC 4.0 license.[136] Copyright 2016, The American Association for the Advancement of Science. Reproduced with permission.[180] Copyright 2015, American Chemical Society. Reproduced with permission.[15] Copyright 2017, Elsevier. Reproduced under the terms of the CC-BY 4.0 license.[211] Copyright 2018, Springer Nature. Reproduced with permission.[17] Copyright 2018, Wiley-VCH.

Some specific questions related to TENG development are summarized as follows.

(1) The fundamental physics of triboelectrification remains unclear, and the understanding of the phenomena is critical for achieving high performance TENG with optimized materials and structures.

(2) Advanced power management strategies are required to achieve better energy storage efficiency when TENG is not used directly as power sources. Direct charging of energy storage devices such as batteries and capacitors using TENG is not efficient due to impedance mismatch.

(3) Many proof-of-concept demonstrations have been made using TENG, but the robustness and durability of proposed systems need to be improved for practical applications.

# REFERENCES


1. F. A. Furfari, *A history of the Van de Graaff generator*. IEEE Industry Applications Magazine, 2005. **11**(1): p. 10-14.

2. Feng-Ru Fan, Zhong-Qun Tian, and Zhong Lin Wang, *Flexible triboelectric generator*. Nano Energy, 2012. **1**(2): p. 328-334.

3. Zhong Lin Wang, *Triboelectric nanogenerators as new energy technology and self-powered sensors - Principles, problems and perspectives.* Faraday Discussions, 2014. **176**(0): p. 447-458.

4. Sihong Wang, Long Lin, and Zhong Lin Wang, *Nanoscale Triboelectric-Effect-Enabled Energy Conversion for Sustainably Powering Portable Electronics.* Nano Letters, 2012. **12**(12): p. 6339-6346.

5. Sihong Wang, Long Lin, Yannan Xie, Qingshen Jing, Simiao Niu, and Zhong Lin Wang, *Sliding-Triboelectric Nanogenerators Based on In-Plane Charge-Separation Mechanism.* Nano Letters, 2013. **13**(5): p. 2226-2233.

6. Guang Zhu, Jun Chen, Ying Liu, Peng Bai, Yu Sheng Zhou, Qingshen Jing, Caofeng Pan, and Zhong Lin Wang, *Linear-Grating Triboelectric Generator Based on Sliding Electrification.* Nano Letters, 2013. **13**(5): p. 2282-2289.

7. Ya Yang, Hulin Zhang, Jun Chen, Qingshen Jing, Yu Sheng Zhou, Xiaonan Wen, and Zhong Lin Wang, *Single-Electrode-Based Sliding Triboelectric Nanogenerator for Self-Powered Displacement Vector Sensor System.* ACS Nano, 2013. **7**(8): p. 7342-7351.

8. Sihong Wang, Yannan Xie, Simiao Niu, Long Lin, and Zhong Lin Wang, *Freestanding Triboelectric-Layer-Based Nanogenerators for Harvesting Energy from a Moving Object or Human Motion in Contact and Non-contact Modes.* Advanced Materials, 2014. **26**(18): p. 2818-2824.

9. Zhong Lin Wang, *Triboelectric Nanogenerators as New Energy Technology for Self-Powered Systems and as Active Mechanical and Chemical Sensors.* ACS Nano, 2013. **7**(11): p. 9533-9557.

10. Zhong Lin Wang, Jun Chen, and Long Lin, *Progress in triboelectric nanogenerators as a new energy technology and self-powered sensors.* Energy & Environmental Science, 2015. **8**(8): p. 2250-2282.

11. Aurelia Chi Wang, Changsheng Wu, Dario Pisignano, Zhong Lin Wang, and Luana Persano, *Polymer nanogenerators: Opportunities and challenges for large-scale applications.* Journal of Applied Polymer Science, 2018. **135**(24): p. 45674.

12. Cheng Xu, Yunlong Zi, Aurelia Chi Wang, Haiyang Zou, Yejing Dai, Xu He, Peihong Wang, Yi-Cheng Wang, Peizhong Feng, Dawei Li, and Zhong Lin Wang, *On the Electron-Transfer Mechanism in the Contact-Electrification Effect.* Advanced Materials, 2018. **30**(15): p. 1706790.

13. Cheng Xu, Aurelia Chi Wang, Haiyang Zou, Binbin Zhang, Chunli Zhang, Yunlong Zi, Lun Pan, Peihong Wang, Peizhong Feng, Zhiqun Lin, and Zhong Lin Wang, *Raising the Working Temperature of a Triboelectric Nanogenerator by Quenching down Electron Thermionic Emission in Contact-Electrification.* Advanced Materials, 2018. **0**(0): p. 1803968.

14. Guang Zhu, Yu Sheng Zhou, Peng Bai, Xian Song Meng, Qingshen Jing, Jun Chen, and Zhong Lin Wang, *A Shape-Adaptive Thin-Film-Based Approach for 50% High-Efficiency Energy Generation Through Micro-Grating Sliding Electrification.* Advanced Materials, 2014. **26**(23): p. 3788-3796.

15. Zhong Lin Wang, Tao Jiang, and Liang Xu, *Toward the blue energy dream by triboelectric nanogenerator networks.* Nano Energy, 2017. **39**: p. 9-23.

16. Zhong Lin Wang, *On Maxwell's displacement current for energy and sensors: the origin of nanogenerators.* Materials Today, 2017. **20**(2): p. 74-82.

17. Changsheng Wu, Aurelia C. Wang, Wenbo Ding, Hengyu Guo, and Zhong Lin Wang, *Triboelectric Nanogenerator: A Foundation of the Energy for the New Era.* Advanced Energy Materials, 2019. **9**(1): p. 1802906.

18. Simiao Niu, Sihong Wang, Long Lin, Ying Liu, Yu Sheng Zhou, Youfan Hu, and Zhong Lin Wang, *Theoretical study of contact-mode triboelectric nanogenerators as an effective power source.* Energy & Environmental Science, 2013. **6**(12): p. 3576-3583.

19. Simiao Niu, Ying Liu, Sihong Wang, Long Lin, Yu Sheng Zhou, Youfan Hu, and Zhong Lin Wang, *Theory of Sliding-Mode Triboelectric Nanogenerators.* Advanced Materials, 2013. **25**(43): p. 6184-6193.

20. Simiao Niu, Sihong Wang, Ying Liu, Yu Sheng Zhou, Long Lin, Youfan Hu, Ken C. Pradel, and Zhong Lin Wang, *A theoretical study of grating structured triboelectric nanogenerators.* Energy & Environmental Science, 2014. **7**(7): p. 2339-2349.

21. Simiao Niu, Ying Liu, Xiangyu Chen, Sihong Wang, Yu Sheng Zhou, Long Lin, Yannan Xie, and Zhong Lin Wang, *Theory of freestanding triboelectric-layer-based nanogenerators.* Nano Energy, 2015. **12**(0): p. 760-774.

22. Niu Simiao, Liu Ying, Zhou Yu Sheng, Wang Sihong, Lin Long, and Wang Zhong Lin, *Optimization of Triboelectric Nanogenerator Charging Systems for Efficient Energy Harvesting and Storage.* Electron Devices, IEEE Transactions on, 2015. **62**(2): p. 641-647.

23. Tao Jiang, Xiangyu Chen, Chang Bao Han, Wei Tang, and Zhong Lin Wang, *Theoretical Study of Rotary Freestanding Triboelectric Nanogenerators.* Advanced Functional Materials, 2015. **25**(19): p. 2928-2938.

24. R. D. Ishara G. Dharmasena, Jonathan H. B. Deane, and S. Ravi P. Silva, *Nature of Power Generation and Output Optimization Criteria for Triboelectric Nanogenerators.* Advanced Energy Materials. **0**(0): p. 1802190.

25. R. D. I. G. Dharmasena, K. D. G. I. Jayawardena, C. A. Mills, J. H. B. Deane, J. V. Anguita, R. A. Dorey, and S. R. P. Silva, *Triboelectric nanogenerators: providing a fundamental framework.* Energy & Environmental Science, 2017. **10**(8): p. 1801-1811.

26. Simiao Niu and Zhong Lin Wang, *Theoretical systems of triboelectric nanogenerators.* Nano Energy, 2015. **14**: p. 161-192.

27. Simiao Niu, Ying Liu, Sihong Wang, Long Lin, Yu Sheng Zhou, Youfan Hu, and Zhong Lin Wang, *Theoretical Investigation and Structural Optimization of Single-Electrode Triboelectric Nanogenerators.* Advanced Functional Materials, 2014. **24**(22): p. 3332-3340.

28. Weiqing Yang, Jun Chen, Guang Zhu, Jin Yang, Peng Bai, Yuanjie Su, Qingsheng Jing, Xia Cao, and Zhong Lin Wang, *Harvesting Energy from the Natural Vibration of Human Walking.* ACS Nano, 2013. **7**(12): p. 11317-11324.

29. Arunkumar Chandrasekhar, Nagamalleswara Rao Alluri, Venkateswaran Vivekananthan, Yuvasree Purusothaman, and Sang-Jae Kim, *A sustainable freestanding biomechanical energy harvesting smart backpack as a portable-wearable power source.* Journal of Materials Chemistry C, 2017. **5**(6): p. 1488-1493.

30. Ting Quan, Xue Wang, Zhong Lin Wang, and Ya Yang, *Hybridized Electromagnetic–Triboelectric Nanogenerator for a Self-Powered Electronic Watch.* ACS Nano, 2015. **9**(12): p. 12301-12310.

31. Jin Yang, Jun Chen, Ying Liu, Weiqing Yang, Yuanjie Su, and Zhong Lin Wang, *Triboelectrification-Based Organic Film Nanogenerator for Acoustic Energy Harvesting and Self-Powered Active Acoustic Sensing.* ACS Nano, 2014. **8**(3): p. 2649-2657.

32. Xing Fan, Jun Chen, Jin Yang, Peng Bai, Zhaoling Li, and Zhong Lin Wang, *Ultrathin, Rollable, Paper-Based Triboelectric Nanogenerator for Acoustic Energy Harvesting and Self-Powered Sound Recording.* ACS Nano, 2015. **9**(4): p. 4236-4243.

33. Ya Yang, Hulin Zhang, Zong-Hong Lin, Yu Sheng Zhou, Qingshen Jing, Yuanjie Su, Jin Yang, Jun Chen, Chenguo Hu, and Zhong Lin Wang, *Human Skin Based*

*Triboelectric Nanogenerators for Harvesting Biomechanical Energy and as Self-Powered Active Tactile Sensor System.* ACS Nano, 2013. **7**(10): p. 9213-9222.

34. Long Lin, Yannan Xie, Sihong Wang, Wenzhuo Wu, Simiao Niu, Xiaonan Wen, and Zhong Lin Wang, *Triboelectric Active Sensor Array for Self-Powered Static and Dynamic Pressure Detection and Tactile Imaging.* ACS Nano, 2013. **7**(9): p. 8266-8274.

35. Guang Zhu, Wei Qing Yang, Tiejun Zhang, Qingshen Jing, Jun Chen, Yu Sheng Zhou, Peng Bai, and Zhong Lin Wang, *Self-Powered, Ultrasensitive, Flexible Tactile Sensors Based on Contact Electrification.* Nano Letters, 2014. **14**(6): p. 3208-3213.

36. Aifang Yu, Ming Song, Yan Zhang, Yang Zhang, Libo Chen, Junyi Zhai, and ZhongLin Wang, *Self-powered acoustic source locator in underwater environment based on organic film triboelectric nanogenerator.* Nano Research, 2015. **8**(3): p. 765-773.

37. Nivedita Arora, Steven L. Zhang, Fereshteh Shahmiri, Diego Osorio, Yi-Cheng Wang, Mohit Gupta, Zhengjun Wang, Thad Starner, Zhong Lin Wang, and Gregory D. Abowd, *SATURN: A Thin and Flexible Self-powered Microphone Leveraging Triboelectric Nanogenerator.* Proc. ACM Interact. Mob. Wearable Ubiquitous Technol., 2018. **2**(2): p. 1-28.

38. Yu Sheng Zhou, Guang Zhu, Simiao Niu, Ying Liu, Peng Bai, Qingsheng Jing, and Zhong Lin Wang, *Nanometer Resolution Self-Powered Static and Dynamic Motion Sensor Based on Micro-Grated Triboelectrification.* Advanced Materials, 2014. **26**(11): p. 1719-1724.

39. Fang Yi, Long Lin, Simiao Niu, Jin Yang, Wenzhuo Wu, Sihong Wang, Qingliang Liao, Yue Zhang, and Zhong Lin Wang, *Self-Powered Trajectory, Velocity, and Acceleration Tracking of a Moving Object/Body using a Triboelectric Sensor.* Advanced Functional Materials, 2014. **24**(47): p. 7488-7494.

40. Changsheng Wu, Xin Wang, Long Lin, Hengyu Guo, and Zhong Lin Wang, *Paper-Based Triboelectric Nanogenerators Made of Stretchable Interlocking Kirigami Patterns.* ACS Nano, 2016. **10**(4): p. 4652-4659.

41. Zong-Hong Lin, Guang Zhu, Yu Sheng Zhou, Ya Yang, Peng Bai, Jun Chen, and Zhong Lin Wang, *A Self-Powered Triboelectric Nanosensor for Mercury Ion Detection.* Angewandte Chemie International Edition, 2013. **52**(19): p. 5065-5069.

42. Zhaoling Li, Jun Chen, Jin Yang, Yuanjie Su, Xing Fan, Ying Wu, Chongwen Yu, and Zhong Lin Wang, *[small beta]-cyclodextrin enhanced triboelectrification for self-powered phenol detection and electrochemical degradation.* Energy & Environmental Science, 2015. **8**(3): p. 887-896.

43. Zhen Wen, Jun Chen, Min-Hsin Yeh, Hengyu Guo, Zhaoling Li, Xing Fan, Tiejun Zhang, Liping Zhu, and Zhong Lin Wang, *Blow-driven triboelectric nanogenerator as an active alcohol breath analyzer.* Nano Energy, 2015. **16**: p. 38-46.

44. Hulin Zhang, Ya Yang, Yuanjie Su, Jun Chen, Chenguo Hu, Zhenkun Wu, Yan Liu, Ching Ping Wong, Yoshio Bando, and Zhong Lin Wang, *Triboelectric nanogenerator as self-powered active sensors for detecting liquid/gaseous water/ethanol.* Nano Energy, 2013. **2**(5): p. 693-701.

45. Stephen Ornes, *Core Concept: The Internet of Things and the explosion of interconnectivity.* Proceedings of the National Academy of Sciences, 2016. **113**(40): p. 11059-11060.

46. Luigi Atzori, Antonio Iera, and Giacomo Morabito, *The Internet of Things: A survey.* Computer Networks, 2010. **54**(15): p. 2787-2805.

47. Xianjie Pu, Hengyu Guo, Jie Chen, Xue Wang, Yi Xi, Chenguo Hu, and Zhong Lin Wang, *Eye motion triggered self-powered mechnosensational communication system using triboelectric nanogenerator.* Science Advances, 2017. **3**(7): p. e1700694.

48. Hengyu Guo, Xianjie Pu, Jie Chen, Yan Meng, Min-Hsin Yeh, Guanlin Liu, Qian Tang, Baodong Chen, Di Liu, Song Qi, Changsheng Wu, Chenguo Hu, Jie Wang, and Zhong Lin Wang, *A highly sensitive, self-powered triboelectric auditory sensor for social robotics and hearing aids.* Science Robotics, 2018. **3**(20): p. eaat2516.

49. Ya Yang, Guang Zhu, Hulin Zhang, Jun Chen, Xiandai Zhong, Zong-Hong Lin, Yuanjie Su, Peng Bai, Xiaonan Wen, and Zhong Lin Wang, *Triboelectric Nanogenerator for Harvesting Wind Energy and as Self-Powered Wind Vector Sensor System.* ACS Nano, 2013. **7**(10): p. 9461-9468.

50. Jihyun Bae, Jeongsu Lee, SeongMin Kim, Jaewook Ha, Byoung-Sun Lee, YoungJun Park, Chweelin Choong, Jin-Baek Kim, Zhong Lin Wang, Ho-Young Kim, Jong-Jin Park, and U. In Chung, *Flutter-driven triboelectrification for harvesting wind energy.* Nature Communications, 2014. **5**.

51. Jiyu Wang, Wenbo Ding, Lun Pan, Changsheng Wu, Hua Yu, Lijun Yang, Ruijin Liao, and Zhong Lin Wang, *Self-Powered Wind Sensor System for Detecting Wind Speed and Direction Based on a Triboelectric Nanogenerator.* ACS Nano, 2018. **12**(4): p. 3954-3963.

52. Bo Chen, Ya Yang, and Zhong Lin Wang, *Scavenging Wind Energy by Triboelectric Nanogenerators.* Advanced Energy Materials, 2018. **8**(10): p. 1702649.

53. Li Zheng, Zong-Hong Lin, Gang Cheng, Wenzhuo Wu, Xiaonan Wen, Sangmin Lee, and Zhong Lin Wang, *Silicon-based hybrid cell for harvesting solar energy and raindrop electrostatic energy.* Nano Energy, 2014. **9**(0): p. 291-300.

54. Hua Rui Zhu, Wei Tang, Cai Zhen Gao, Yu Han, Tao Li, Xia Cao, and Zhong Lin Wang, *Self-powered metal surface anti-corrosion protection using energy harvested from rain drops and wind.* Nano Energy, 2015. **14**: p. 193-200.

55. Min-Hsin Yeh, Long Lin, Po-Kang Yang, and Zhong Lin Wang, *Motion-Driven Electrochromic Reactions for Self-Powered Smart Window System.* ACS Nano, 2015. **9**(5): p. 4757-4765.

56. Yi Xi, Jie Wang, Yunlong Zi, Xiaogan Li, Changbao Han, Xia Cao, Chenguo Hu, and Zhonglin Wang, *High efficient harvesting of underwater ultrasonic wave energy by triboelectric nanogenerator.* Nano Energy, 2017. **38**: p. 101-108.

57. Ya Yang, Hulin Zhang, Ruoyu Liu, Xiaonan Wen, Te-Chien Hou, and Zhong Lin Wang, *Fully Enclosed Triboelectric Nanogenerators for Applications in Water and Harsh Environments.* Advanced Energy Materials, 2013. **3**(12): p. 1563-1568.

58. Xiaonan Wen, Weiqing Yang, Qingshen Jing, and Zhong Lin Wang, *Harvesting Broadband Kinetic Impact Energy from Mechanical Triggering/Vibration and Water Waves.* ACS Nano, 2014. **8**(7): p. 7405-7412.

59. Li Min Zhang, Chang Bao Han, Tao Jiang, Tao Zhou, Xiao Hui Li, Chi Zhang, and Zhong Lin Wang, *Multilayer wavy-structured robust triboelectric nanogenerator for harvesting water wave energy.* Nano Energy, 2016. **22**: p. 87-94.

60. Z. L. Wang, *Catch wave power in floating nets.* Nature, 2017. **542**(7640): p. 159-160.

61. Yunlong Zi, Hengyu Guo, Zhen Wen, Min-Hsin Yeh, Chenguo Hu, and Zhong Lin Wang, *Harvesting Low-Frequency (<5 Hz) Irregular Mechanical Energy: A Possible Killer Application of Triboelectric Nanogenerator.* ACS Nano, 2016. **10**(4): p. 4797-4805.

62. Hassan Askari, Amir Khajepour, Mir Behrad Khamesee, Zia Saadatnia, and Zhong Lin Wang, *Piezoelectric and triboelectric nanogenerators: Trends and impacts.* Nano Today, 2018.

63. Munan Li, Alan L. Porter, and Zhong Lin Wang, *Evolutionary trend analysis of nanogenerator research based on a novel perspective of phased bibliographic coupling.* Nano Energy, 2017. **34**: p. 93-102.

64. Haoshu Peng, Xudong Fang, Samira Ranaei, Zhen Wen, and Alan L. Porter, *Forecasting potential sensor applications of triboelectric nanogenerators through tech mining.* Nano Energy, 2017. **35**: p. 358-369.

65. Abdelsalam Ahmed, Islam Hassan, Taofeeq Ibn-Mohammed, Hassan Mostafa, Ian M. Reaney, Lenny S. C. Koh, Jean Zu, and Zhong Lin Wang, *Environmental life cycle assessment and techno-economic analysis of triboelectric nanogenerators.* Energy & Environmental Science, 2017. **10**(3): p. 653-671.

66. Baicun Wang, Yufei Liu, Yuan Zhou, and Zhen Wen, *Emerging nanogenerator technology in China: A review and forecast using integrating bibliometrics, patent analysis and technology roadmapping methods.* Nano Energy, 2018. **46**: p. 322-330.

67. Shuwen Chen, Caizhen Gao, Wei Tang, Huarui Zhu, Yu Han, Qianwen Jiang, Tao Li, Xia Cao, and Zhonglin Wang, *Self-powered cleaning of air pollution by wind driven triboelectric nanogenerator.* Nano Energy, 2015. **14**: p. 217-225.

68. Yu Bai, Chang Bao Han, Chuan He, Guang Qin Gu, Jin Hui Nie, Jia Jia Shao, Tian Xiao Xiao, Chao Ran Deng, and Zhong Lin Wang, *Washable Multilayer Triboelectric Air Filter for Efficient Particulate Matter PM2.5 Removal.* Advanced Functional Materials, 2018. **28**(15): p. 1706680.

69. Sihong Wang, Yannan Xie, Simiao Niu, Long Lin, Chang Liu, Yu Sheng Zhou, and Zhong Lin Wang, *Maximum Surface Charge Density for Triboelectric Nanogenerators Achieved by Ionized-Air Injection: Methodology and Theoretical Understanding.* Advanced Materials, 2014. **26**(39): p. 6720-6728.

70. Jie Wang, Shengming Li, Fang Yi, Yunlong Zi, Jun Lin, Xiaofeng Wang, Youlong Xu, and Zhong Lin Wang, *Sustainably powering wearable electronics solely by biomechanical energy.* Nature Communications, 2016. **7**: p. 12744.

71. Jie Wang, Changsheng Wu, Yejing Dai, Zhihao Zhao, Aurelia Wang, Tiejun Zhang, and Zhong Lin Wang, *Achieving ultrahigh triboelectric charge density for efficient energy harvesting.* Nature Communications, 2017. **8**(1): p. 88.

72. Yunlong Zi, Simiao Niu, Jie Wang, Zhen Wen, Wei Tang, and Zhong Lin Wang, *Standards and figure-of-merits for quantifying the performance of triboelectric nanogenerators.* Nature Communications, 2015. **6**: p. 8376.

73. H. T. Baytekin, A. Z. Patashinski, M. Branicki, B. Baytekin, S. Soh, and B. A. Grzybowski, *The Mosaic of Surface Charge in Contact Electrification.* Science, 2011. **333**(6040): p. 308.

74. Jun Chen, Jin Yang, Zhaoling Li, Xing Fan, Yunlong Zi, Qingshen Jing, Hengyu Guo, Zhen Wen, Ken C. Pradel, Simiao Niu, and Zhong Lin Wang, *Networks of Triboelectric Nanogenerators for Harvesting Water Wave Energy: A Potential Approach toward Blue Energy.* ACS Nano, 2015. **9**(3): p. 3324-3331.

75. Xiaofeng Wang, Simiao Niu, Yajiang Yin, Fang Yi, Zheng You, and Zhong Lin Wang, *Triboelectric Nanogenerator Based on Fully Enclosed Rolling Spherical Structure for Harvesting Low-Frequency Water Wave Energy.* Advanced Energy Materials, 2015. **5**(24): p. 1501467.

76. D. Friedman, H. Heinrich, and D. W. Duan. *A low-power CMOS integrated circuit for field-powered radio frequency identification tags*. in *Solid-State Circuits*

*Conference, 1997. Digest of Technical Papers. 43rd ISSCC., 1997 IEEE International*. 1997.

77. M. Chinchilla, S. Arnaltes, and J. C. Burgos, *Control of permanent-magnet generators applied to variable-speed wind-energy systems connected to the grid.* IEEE Transactions on Energy Conversion, 2006. **21**(1): p. 130-135.

78. S. Rahman, *Green power: what is it and where can we find it?* IEEE Power and Energy Magazine, 2003. **1**(1): p. 30-37.

79. H. Kulah and K. Najafi. *An electromagnetic micro power generator for low-frequency environmental vibrations*. in *Micro Electro Mechanical Systems, 2004. 17th IEEE International Conference on. (MEMS)*. 2004.

80. Hyung-Jo Jung, In-Ho Kim, Dong Yi Min, Sung-Han Sim, and Jeong-Hoi Koo. *A hybrid electromagnetic energy harvesting device for low frequency vibration*. 2013.

81. S. Palagummi and F. G. Yuan. *A vibration energy harvester using diamagnetic levitation*. 2013.

82. Jin Yang, Jun Chen, Ya Yang, Hulin Zhang, Weiqing Yang, Peng Bai, Yuanjie Su, and Zhong Lin Wang, *Broadband Vibrational Energy Harvesting Based on a Triboelectric Nanogenerator.* Advanced Energy Materials, 2014. **4**(6): p. n/a-n/a.

83. Jun Chen, Guang Zhu, Weiqing Yang, Qingshen Jing, Peng Bai, Ya Yang, Te-Chien Hou, and Zhong Lin Wang, *Harmonic-Resonator-Based Triboelectric Nanogenerator as a Sustainable Power Source and a Self-Powered Active Vibration Sensor.* Advanced Materials, 2013. **25**(42): p. 6094-6099.

84. Sihong Wang, Simiao Niu, Jin Yang, Long Lin, and Zhong Lin Wang, *Quantitative Measurements of Vibration Amplitude Using a Contact-Mode Freestanding Triboelectric Nanogenerator.* ACS Nano, 2014. **8**(12): p. 12004-12013.

85. Changsheng Wu, Ruiyuan Liu, Jie Wang, Yunlong Zi, Long Lin, and Zhong Lin Wang, *A spring-based resonance coupling for hugely enhancing the performance of triboelectric nanogenerators for harvesting low-frequency vibration energy.* Nano Energy, 2017. **32**: p. 287-293.

86. Scott D. Moss, Genevieve A. Hart, Stephen K. Burke, and Gregory P. Carman, *Hybrid rotary-translational vibration energy harvester using cycloidal motion as a mechanical amplifier.* Applied Physics Letters, 2014. **104**(3): p. 033506.

87. Francesco Cottone, Ronan Frizzell, Suresh Goyal, Gerard Kelly, and Jeff Punch, *Enhanced vibrational energy harvester based on velocity amplification.* Journal of Intelligent Material Systems and Structures, 2014. **25**(4): p. 443-451.

88. x00D, Zorlu, E. T. Topal, and H. Kulah, *A Vibration-Based Electromagnetic Energy Harvester Using Mechanical Frequency Up-Conversion Method.* IEEE Sensors Journal, 2011. **11**(2): p. 481-488.

89. S. Ju, S. H. Chae, Y. Choi, S. Jun, S. M. Park, S. Lee, H. W. Lee, and C. H. Ji, *Frequency Up-Converted Low Frequency Vibration Energy Harvester Using Trampoline Effect.* Journal of Physics: Conference Series, 2013. **476**(1): p. 012089.

90. Bryan Rodgers, Suresh Goyal, Gerard Kelly, and Michael Sheehy, *The Dynamics of Multiple Pair-Wise Collisions in a Chain for Designing Optimal Shock Amplifiers.* Shock and Vibration, 2009. **16**(1).

91. D. O'Donoghue, R. Frizzell, G. Kelly, K. Nolan, and J. Punch, *The influence of mass configurations on velocity amplified vibrational energy harvesters.* Smart Materials and Structures, 2016. **25**(5): p. 055012.

92. Long Lin, Yannan Xie, Simiao Niu, Sihong Wang, Po-Kang Yang, and Zhong Lin Wang, *Robust Triboelectric Nanogenerator Based on Rolling Electrification and Electrostatic Induction at an Instantaneous Energy Conversion Efficiency of ~55%.* ACS Nano, 2015. **9**(1): p. 922-930.

93. Mehmet Kanik, Mehmet Girayhan Say, Bihter Daglar, Ahmet Faruk Yavuz, Muhammet Halit Dolas, Mostafa M. El-Ashry, and Mehmet Bayindir, *A Motion- and Sound-Activated, 3D-Printed, Chalcogenide-Based Triboelectric Nanogenerator.* Advanced Materials, 2015. **27**(14): p. 2367-2376.

94. Guang Zhu, Jun Chen, Tiejun Zhang, Qingshen Jing, and Zhong Lin Wang, *Radial-arrayed rotary electrification for high performance triboelectric generator.* Nature Communications, 2014. **5**.

95. Gang Cheng, Zong-Hong Lin, Long Lin, Zu-liang Du, and Zhong Lin Wang, *Pulsed Nanogenerator with Huge Instantaneous Output Power Density.* ACS Nano, 2013. **7**(8): p. 7383-7391.

96. Yunlong Zi, Jie Wang, Sihong Wang, Shengming Li, Zhen Wen, Hengyu Guo, and Zhong Lin Wang, *Effective energy storage from a triboelectric nanogenerator.* Nature Communications, 2016. **7**: p. 10987.

97. Alex Chortos and Zhenan Bao, *Skin-inspired electronic devices.* Materials Today, 2014. **17**(7): p. 321-331.

98. Takeo Yamada, Yuhei Hayamizu, Yuki Yamamoto, Yoshiki Yomogida, Ali Izadi-Najafabadi, Don N. Futaba, and Kenji Hata, *A stretchable carbon nanotube strain sensor for human-motion detection.* Nature Nanotechnology, 2011. **6**(5): p. 296-301.

99. Tsuyoshi Sekitani, Hiroyoshi Nakajima, Hiroki Maeda, Takanori Fukushima, Takuzo Aida, Kenji Hata, and Takao Someya, *Stretchable active-matrix organic*

*light-emitting diode display using printable elastic conductors.* Nature Materials, 2009. **8**(6): p. 494-499.

100. Dae-Hyeong Kim, Jong-Hyun Ahn, Won Mook Choi, Hoon-Sik Kim, Tae-Ho Kim, Jizhou Song, Yonggang Y. Huang, Zhuangjian Liu, Chun Lu, and John A. Rogers, *Stretchable and Foldable Silicon Integrated Circuits.* Science, 2008. **320**(5875): p. 507-511.

101. Lizhi Xu, Sarah R. Gutbrod, Andrew P. Bonifas, Yewang Su, Matthew S. Sulkin, Nanshu Lu, Hyun-Joong Chung, Kyung-In Jang, Zhuangjian Liu, Ming Ying, Chi Lu, R. Chad Webb, Jong-Seon Kim, Jacob I. Laughner, Huanyu Cheng, Yuhao Liu, Abid Ameen, Jae-Woong Jeong, Gwang-Tae Kim, Yonggang Huang, Igor R. Efimov, and John A. Rogers, *3D multifunctional integumentary membranes for spatiotemporal cardiac measurements and stimulation across the entire epicardium.* Nature Communications, 2014. **5**.

102. Terry C. Shyu, Pablo F. Damasceno, Paul M. Dodd, Aaron Lamoureux, Lizhi Xu, Matthew Shlian, Max Shtein, Sharon C. Glotzer, and Nicholas A. Kotov, *A kirigami approach to engineering elasticity in nanocomposites through patterned defects.* Nature Materials, 2015. **14**(8): p. 785-789.

103. Aaron Lamoureux, Kyusang Lee, Matthew Shlian, Stephen R. Forrest, and Max Shtein, *Dynamic kirigami structures for integrated solar tracking.* Nature Communications, 2015. **6**.

104. Zeming Song, Teng Ma, Rui Tang, Qian Cheng, Xu Wang, Deepakshyam Krishnaraju, Rahul Panat, Candace K. Chan, Hongyu Yu, and Hanqing Jiang, *Origami lithium-ion batteries.* Nature Communications, 2014. **5**.

105. Jesse L. Silverberg, Arthur A. Evans, Lauren McLeod, Ryan C. Hayward, Thomas Hull, Christian D. Santangelo, and Itai Cohen, *Using origami design principles to fold reprogrammable mechanical metamaterials.* Science, 2014. **345**(6197): p. 647-650.

106. Jeong-Hyun Cho, Michael D. Keung, Niels Verellen, Liesbet Lagae, Victor V. Moshchalkov, Pol Van Dorpe, and David H. Gracias, *Nanoscale Origami for 3D Optics.* Small, 2011. **7**(14): p. 1943-1948.

107. Chang Kyu Jeong, Kwang Min Baek, Simiao Niu, Tae Won Nam, Yoon Hyung Hur, Dae Yong Park, Geon-Tae Hwang, Myunghwan Byun, Zhong Lin Wang, Yeon Sik Jung, and Keon Jae Lee, *Topographically-Designed Triboelectric Nanogenerator via Block Copolymer Self-Assembly.* Nano Letters, 2014. **14**(12): p. 7031-7038.

108. Yannan Xie, Sihong Wang, Simiao Niu, Long Lin, Qingshen Jing, Jin Yang, Zhengyun Wu, and Zhong Lin Wang, *Grating-Structured Freestanding Triboelectric-Layer Nanogenerator for Harvesting Mechanical Energy at 85% Total Conversion Efficiency.* Advanced Materials, 2014. **26**(38): p. 6599-6607.

109. Hao Fang, Wenzhuo Wu, Jinhui Song, and Zhong Lin Wang, *Controlled Growth of Aligned Polymer Nanowires.* The Journal of Physical Chemistry C, 2009. **113**(38): p. 16571-16574.

110. Suk-Won Hwang, Hu Tao, Dae-Hyeong Kim, Huanyu Cheng, Jun-Kyul Song, Elliott Rill, Mark A. Brenckle, Bruce Panilaitis, Sang Min Won, Yun-Soung Kim, Young Min Song, Ki Jun Yu, Abid Ameen, Rui Li, Yewang Su, Miaomiao Yang, David L. Kaplan, Mitchell R. Zakin, Marvin J. Slepian, Yonggang Huang, Fiorenzo G. Omenetto, and John A. Rogers, *A Physically Transient Form of Silicon Electronics.* Science, 2012. **337**(6102): p. 1640.

111. Suk-Won Hwang, Gayoung Park, Huanyu Cheng, Jun-Kyul Song, Seung-Kyun Kang, Lan Yin, Jae-Hwan Kim, Fiorenzo G. Omenetto, Yonggang Huang, Kyung-Mi Lee, and John A. Rogers, *25th Anniversary Article: Materials for High-Performance Biodegradable Semiconductor Devices.* Advanced Materials, 2014. **26**(13): p. 1992-2000.

112. G. Gourdin, O. Phillips, J. Schwartz, A. Engler, and P. Kohl. *Phototriggerable, Fully Transient Electronics: Component and Device Fabrication*. in *2017 IEEE 67th Electronic Components and Technology Conference (ECTC)*. 2017. Orlando, FL, USA.

113. Qiang Zheng, Yang Zou, Yalan Zhang, Zhuo Liu, Bojing Shi, Xinxin Wang, Yiming Jin, Han Ouyang, Zhou Li, and Zhong Lin Wang, *Biodegradable triboelectric nanogenerator as a life-time designed implantable power source.* Science Advances, 2016. **2**(3): p. e1501478.

114. Kyung Min Lee, Oluwadamilola Phillips, Anthony Engler, Paul A. Kohl, and Barry P. Rand, *Phototriggered Depolymerization of Flexible Poly(phthalaldehyde) Substrates by Integrated Organic Light-Emitting Diodes.* ACS Applied Materials & Interfaces, 2018. **10**(33): p. 28062-28068.

115. Suk-Won Hwang, Dae-Hyeong Kim, Hu Tao, Tae-il Kim, Stanley Kim, Ki Jun Yu, Bruce Panilaitis, Jae-Woong Jeong, Jun-Kyul Song, Fiorenzo G. Omenetto, and John. A. Rogers, *Materials and Fabrication Processes for Transient and Bioresorbable High-Performance Electronics.* Advanced Functional Materials, 2013. **23**(33): p. 4087-4093.

116. Dae-Hyeong Kim, Jonathan Viventi, Jason J. Amsden, Jianliang Xiao, Leif Vigeland, Yun-Soung Kim, Justin A. Blanco, Bruce Panilaitis, Eric S. Frechette, Diego Contreras, David L. Kaplan, Fiorenzo G. Omenetto, Yonggang Huang, Keh-Chih Hwang, Mitchell R. Zakin, Brian Litt, and John A. Rogers, *Dissolvable films of silk fibroin for ultrathin conformal bio-integrated electronics.* Nature Materials, 2010. **9**: p. 511.

117. Christopher J. Bettinger and Zhenan Bao, *Organic Thin-Film Transistors Fabricated on Resorbable Biomaterial Substrates.* Advanced Materials, 2010. **22**(5): p. 651-655.

118. Handan Acar, Simge Çınar, Mahendra Thunga, Michael R. Kessler, Nastaran Hashemi, and Reza Montazami, *Study of Physically Transient Insulating Materials as a Potential Platform for Transient Electronics and Bioelectronics.* Advanced Functional Materials, 2014. **24**(26): p. 4135-4143.

119. Suk-Won Hwang, Xian Huang, Jung-Hun Seo, Jun-Kyul Song, Stanley Kim, Sami Hage-Ali, Hyun-Joong Chung, Hu Tao, Fiorenzo G. Omenetto, Zhenqiang Ma, and John A. Rogers, *Materials for Bioresorbable Radio Frequency Electronics.* Advanced Materials, 2013. **25**(26): p. 3526-3531.

120. Canan Dagdeviren, Suk-Won Hwang, Yewang Su, Stanley Kim, Huanyu Cheng, Onur Gur, Ryan Haney, Fiorenzo G. Omenetto, Yonggang Huang, and John A. Rogers, *Transient, Biocompatible Electronics and Energy Harvesters Based on ZnO.* Small, 2013. **9**(20): p. 3398-3404.

121. Hector Lopez Hernandez, Seung-Kyun Kang, Olivia P. Lee, Suk-Won Hwang, Joshua A. Kaitz, Bora Inci, Chan Woo Park, Sangjin Chung, Nancy R. Sottos, Jeffrey S. Moore, John A. Rogers, and Scott R. White, *Triggered Transience of Metastable Poly(phthalaldehyde) for Transient Electronics.* Advanced Materials, 2014. **26**(45): p. 7637-7642.

122. Chan Woo Park, Seung-Kyun Kang, Hector Lopez Hernandez, Joshua A. Kaitz, Dae Seung Wie, Jiho Shin, Olivia P. Lee, Nancy R. Sottos, Jeffrey S. Moore, John A. Rogers, and Scott R. White, *Thermally Triggered Degradation of Transient Electronic Devices.* Advanced Materials, 2015. **27**(25): p. 3783-3788.

123. Wen Jiang, Hu Li, Zhuo Liu, Zhe Li, Jingjing Tian, Bojing Shi, Yang Zou, Han Ouyang, Chaochao Zhao, Luming Zhao, Rong Sun, Hairong Zheng, Yubo Fan, Zhong Lin Wang, and Zhou Li, *Fully Bioabsorbable Natural-Materials-Based Triboelectric Nanogenerators.* Advanced Materials, 2018. **30**(32): p. 1801895.

124. Zhe Li, Hongqing Feng, Qiang Zheng, Hu Li, Chaochao Zhao, Han Ouyang, Sehrish Noreen, Min Yu, Fan Su, Ruping Liu, Linlin Li, Zhong Lin Wang, and Zhou Li, *Photothermally tunable biodegradation of implantable triboelectric nanogenerators for tissue repairing.* Nano Energy, 2018. **54**: p. 390-399.

125. Jared M. Schwartz, Oluwadamilola Phillips, Anthony Engler, Alexandra Sutlief, Jihyun Lee, and Paul A. Kohl, *Stable, High-Molecular-Weight Poly(phthalaldehyde).* Journal of Polymer Science Part A: Polymer Chemistry, 2017. **55**(7): p. 1166-1172.

126. Minoru Tsuda, Masayuki Hata, Rie Nishida, and Setsuko Oikawa, *Acid-catalyzed degradation mechanism of poly(phthalaldehyde): Unzipping reaction of chemical amplification resist.* Journal of Polymer Science Part A: Polymer Chemistry, 1997. **35**(1): p. 77-89.

127. O. Phillips, A. Engler, J. M. Schwartz, J. Jiang, C. Tobin, Y. A. Guta, and P. A. Kohl, *Sunlight photodepolymerization of transient polymers.* Journal of Applied Polymer Science, 2019. **136**(9): p. 47141.

128. James V. Crivello and Myoungsouk Jang, *Anthracene electron-transfer photosensitizers for onium salt induced cationic photopolymerizations.* Journal of Photochemistry and Photobiology A: Chemistry, 2003. **159**(2): p. 173-188.

129. Jisu Jiang, Oluwadamilola Phillips, Anthony Engler, Man Hou Vong, and Paul A. Kohl, *Photodegradable transient bilayered poly(phthalaldehyde) with improved shelf life.* Polymers for Advanced Technologies, 2019: p. 1-7.

130. Wenbo Ding, Changsheng Wu, Yunlong Zi, Haiyang Zou, Jiyu Wang, Jia Cheng, Aurelia C. Wang, and Zhong Lin Wang, *Self-powered wireless optical transmission of mechanical agitation signals.* Nano Energy, 2018. **47**: p. 566-572.

131. Fang Yi, Xiaofeng Wang, Simiao Niu, Shengming Li, Yajiang Yin, Keren Dai, Guangjie Zhang, Long Lin, Zhen Wen, Hengyu Guo, Jie Wang, Min-Hsin Yeh, Yunlong Zi, Qingliang Liao, Zheng You, Yue Zhang, and Zhong Lin Wang, *A highly shape-adaptive, stretchable design based on conductive liquid for energy harvesting and self-powered biomechanical monitoring.* Science Advances, 2016. **2**(6): p. e1501624.

132. Xiong Pu, Mengmeng Liu, Xiangyu Chen, Jiangman Sun, Chunhua Du, Yang Zhang, Junyi Zhai, Weiguo Hu, and Zhong Lin Wang, *Ultrastretchable, transparent triboelectric nanogenerator as electronic skin for biomechanical energy harvesting and tactile sensing.* Science Advances, 2017. **3**(5): p. e1700015.

133. Junwen Zhong, Yan Zhang, Qize Zhong, Qiyi Hu, Bin Hu, Zhong Lin Wang, and Jun Zhou, *Fiber-Based Generator for Wearable Electronics and Mobile Medication.* ACS Nano, 2014. **8**(6): p. 6273-6280.

134. Jun Chen, Yi Huang, Nannan Zhang, Haiyang Zou, Ruiyuan Liu, Changyuan Tao, Xing Fan, and Zhong Lin Wang, *Micro-cable structured textile for simultaneously harvesting solar and mechanical energy.* Nature Energy, 2016. **1**: p. 16138.

135. Kai Dong, Jianan Deng, Yunlong Zi, Yi-Cheng Wang, Cheng Xu, Haiyang Zou, Wenbo Ding, Yejing Dai, Bohong Gu, Baozhong Sun, and Zhong Lin Wang, *3D Orthogonal Woven Triboelectric Nanogenerator for Effective Biomechanical Energy Harvesting and as Self-Powered Active Motion Sensors.* Advanced Materials, 2017. **29**(38): p. 1702648.

136. Zhen Wen, Min-Hsin Yeh, Hengyu Guo, Jie Wang, Yunlong Zi, Weidong Xu, Jianan Deng, Lei Zhu, Xin Wang, Chenguo Hu, Liping Zhu, Xuhui Sun, and Zhong Lin Wang, *Self-powered textile for wearable electronics by hybridizing fiber-shaped nanogenerators, solar cells, and supercapacitors.* Science Advances, 2016. **2**(10): p. e1600097.

137. Mark R. Prausnitz and Robert Langer, *Transdermal drug delivery*. Nature Biotechnology, 2008. **26**: p. 1261.

138. Rong Yang, Tuo Wei, Hannah Goldberg, Weiping Wang, Kathleen Cullion, and Daniel S. Kohane, *Getting Drugs Across Biological Barriers.* Advanced Materials, 2017. **29**(37): p. 1606596.

139. Owen S. Fenton, Katy N. Olafson, Padmini S. Pillai, Michael J. Mitchell, and Robert Langer, *Advances in Biomaterials for Drug Delivery.* Advanced Materials, 2018. **30**(29): p. 1705328.

140. Morteza Amjadi, Sahar Sheykhansari, Bradley J. Nelson, and Metin Sitti, *Recent Advances in Wearable Transdermal Delivery Systems.* Advanced Materials, 2018. **30**(7): p. 1704530.

141. Yogeshvar N. Kalia, Aarti Naik, James Garrison, and Richard H. Guy, *Iontophoretic drug delivery.* Advanced Drug Delivery Reviews, 2004. **56**(5): p. 619-658.

142. Jim E. Riviere and Mark C. Heit, *Electrically-Assisted Transdermal Drug Delivery*. Pharmaceutical Research, 1997. **14**(6): p. 687-697.

143. Y. T. Yi, J. Y. Sun, Y. W. Lu, and Y. C. Liao, *Programmable and on-demand drug release using electrical stimulation.* Biomicrofluidics, 2015. **9**(2): p. 022401.

144. Yudai Ogawa, Koichiro Kato, Takeo Miyake, Kuniaki Nagamine, Takuya Ofuji, Syuhei Yoshino, and Matsuhiko Nishizawa, *Organic Transdermal Iontophoresis Patch with Built-in Biofuel Cell.* Advanced Healthcare Materials, 2015. **4**(4): p. 506-510.

145. Qiu Jiang, Changsheng Wu, Zhengjun Wang, Aurelia Chi Wang, Jr-Hau He, Zhong Lin Wang, and Husam N. Alshareef, *MXene electrochemical microsupercapacitor integrated with triboelectric nanogenerator as a wearable self-charging power unit.* Nano Energy, 2018. **45**: p. 266-272.

146. Xu He, Yunlong Zi, Hengyu Guo, Haiwu Zheng, Yi Xi, Changsheng Wu, Jie Wang, Wei Zhang, Canhui Lu, and Zhong Lin Wang, *A Highly Stretchable Fiber-Based Triboelectric Nanogenerator for Self-Powered Wearable Electronics.* Advanced Functional Materials, 2017. **27**(4): p. 1604378.

147. Ying-Chih Lai, Jianan Deng, Simiao Niu, Wenbo Peng, Changsheng Wu, Ruiyuan Liu, Zhen Wen, and Zhong Lin Wang, *Electric Eel-Skin-Inspired Mechanically Durable and Super-Stretchable Nanogenerator for Deformable Power Source and Fully Autonomous Conformable Electronic-Skin Applications.* Advanced Materials, 2016. **28**(45): p. 10024-10032.

148. Peiyi Song, Shuangyang Kuang, Nishtha Panwar, Guang Yang, Danny Jian Hang Tng, Swee Chuan Tjin, Wun Jern Ng, Maszenan Bin Abdul Majid, Guang Zhu,

Ken-Tye Yong, and Zhong Lin Wang, *A Self-Powered Implantable Drug-Delivery System Using Biokinetic Energy.* Advanced Materials, 2017. **29**(11): p. 1605668.

149. Zhirong Liu, Jinhui Nie, Bin Miao, Jiadong Li, Yuanbo Cui, Shu Wang, Xiaodi Zhang, Gengrui Zhao, Yongbo Deng, Yihui Wu, Zhou Li, Linlin Li, and Zhong Lin Wang, *Self-Powered Intracellular Drug Delivery by a Biomechanical Energy-Driven Triboelectric Nanogenerator.* Advanced Materials. **0**(0): p. 1807795.

150. Yunlong Zi, Changsheng Wu, Wenbo Ding, and Zhong Lin Wang, *Maximized Effective Energy Output of Contact-Separation-Triggered Triboelectric Nanogenerators as Limited by Air Breakdown.* Advanced Functional Materials, 2017. **27**(24): p. 1700049.

151. Changsheng Wu, Wenbo Ding, Ruiyuan Liu, Jiyu Wang, Aurelia C. Wang, Jie Wang, Shengming Li, Yunlong Zi, and Zhong Lin Wang, *Keystroke dynamics enabled authentication and identification using triboelectric nanogenerator array.* Materials Today, 2018. **21**(3): p. 216-222.

152. Murat Oz, Dietrich E. Lorke, and George A. Petroianu, *Methylene blue and Alzheimer's disease.* Biochemical Pharmacology, 2009. **78**(8): p. 927-932.

153. Amir Fakhari, Marta Corcoran, and Alexander Schwarz, *Thermogelling properties of purified poloxamer 407.* Heliyon, 2017. **3**(8): p. e00390.

154. Xiong Pu, Linxuan Li, Huanqiao Song, Chunhua Du, Zhengfu Zhao, Chunyan Jiang, Guozhong Cao, Weiguo Hu, and Zhong Lin Wang, *A Self-Charging Power Unit by Integration of a Textile Triboelectric Nanogenerator and a Flexible Lithium-Ion Battery for Wearable Electronics.* Advanced Materials, 2015. **27**(15): p. 2472-2478.

155. Xiong Pu, Linxuan Li, Mengmeng Liu, Chunyan Jiang, Chunhua Du, Zhenfu Zhao, Weiguo Hu, and Zhong Lin Wang, *Wearable Self-Charging Power Textile Based on Flexible Yarn Supercapacitors and Fabric Nanogenerators.* Advanced Materials, 2016. **28**(1): p. 98-105.

156. Simiao Niu, Xiaofeng Wang, Fang Yi, Yu Sheng Zhou, and Zhong Lin Wang, *A universal self-charging system driven by random biomechanical energy for sustainable operation of mobile electronics.* Nature Communications, 2015. **6**: p. 8975.

157. Guang Zhu, Peng Bai, Jun Chen, and Zhong Lin Wang, *Power-generating shoe insole based on triboelectric nanogenerators for self-powered consumer electronics.* Nano Energy, 2013. **2**(5): p. 688-692.

158. Jie Wang, Xiuhan Li, Yunlong Zi, Sihong Wang, Zhaoling Li, Li Zheng, Fang Yi, Shengming Li, and Zhong Lin Wang, *A Flexible Fiber-Based Supercapacitor–Triboelectric-Nanogenerator Power System for Wearable Electronics.* Advanced Materials, 2015. **27**(33): p. 4830-4836.

159. Hengyu Guo, Min-Hsin Yeh, Yunlong Zi, Zhen Wen, Jie Chen, Guanlin Liu, Chenguo Hu, and Zhong Lin Wang, *Ultralight Cut-Paper-Based Self-Charging Power Unit for Self-Powered Portable Electronic and Medical Systems.* ACS Nano, 2017. **11**(5): p. 4475-4482.

160. You-Yu Peng, Bilen Akuzum, Narendra Kurra, Meng-Qiang Zhao, Mohamed Alhabeb, Babak Anasori, Emin Caglan Kumbur, Husam N. Alshareef, Ming-Der Ger, and Yury Gogotsi, *All-MXene (2D titanium carbide) solid-state microsupercapacitors for on-chip energy storage.* Energy & Environmental Science, 2016. **9**(9): p. 2847-2854.

161. Narendra Kurra, Bilal Ahmed, Yury Gogotsi, and Husam N. Alshareef, *MXene-on-Paper Coplanar Microsupercapacitors.* Advanced Energy Materials, 2016. **6**(24): p. 1601372.

162. Tao Hu, Jiemin Wang, Hui Zhang, Zhaojin Li, Minmin Hu, and Xiaohui Wang, *Vibrational properties of Ti3C2 and Ti3C2T2 (T = O, F, OH) monosheets by first-principles calculations: a comparative study.* Physical Chemistry Chemical Physics, 2015. **17**(15): p. 9997-10003.

163. Kai Wang, Xiong Zhang, Chen Li, Xianzhong Sun, Qinghai Meng, Yanwei Ma, and Zhixiang Wei, *Chemically Crosslinked Hydrogel Film Leads to Integrated Flexible Supercapacitors with Superior Performance.* Advanced Materials, 2015. **27**(45): p. 7451-7457.

164. Majid Beidaghi and Chunlei Wang, *Micro-Supercapacitors Based on Interdigital Electrodes of Reduced Graphene Oxide and Carbon Nanotube Composites with Ultrahigh Power Handling Performance.* Advanced Functional Materials, 2012. **22**(21): p. 4501-4510.

165. Jian Lin, Zhiwei Peng, Yuanyue Liu, Francisco Ruiz-Zepeda, Ruquan Ye, Errol L. G. Samuel, Miguel Jose Yacaman, Boris I. Yakobson, and James M. Tour, *Laser-induced porous graphene films from commercial polymers.* Nature Communications, 2014. **5**: p. 5714.

166. Maher F. El-Kady, Veronica Strong, Sergey Dubin, and Richard B. Kaner, *Laser Scribing of High-Performance and Flexible Graphene-Based Electrochemical Capacitors.* Science, 2012. **335**(6074): p. 1326.

167. Dianpeng Qi, Zhiyuan Liu, Yan Liu, Wan Ru Leow, Bowen Zhu, Hui Yang, Jiancan Yu, Wei Wang, Hua Wang, Shengyan Yin, and Xiaodong Chen, *Suspended Wavy Graphene Microribbons for Highly Stretchable Microsupercapacitors.* Advanced Materials, 2015. **27**(37): p. 5559-5566.

168. Hengyu Guo, Min-Hsin Yeh, Ying-Chih Lai, Yunlong Zi, Changsheng Wu, Zhen Wen, Chenguo Hu, and Zhong Lin Wang, *All-in-One Shape-Adaptive Self-Charging Power Package for Wearable Electronics.* ACS Nano, 2016. **10**(11): p. 10580-10588.

169. Mohamed Alhabeb, Kathleen Maleski, Babak Anasori, Pavel Lelyukh, Leah Clark, Saleesha Sin, and Yury Gogotsi, *Guidelines for Synthesis and Processing of Two-Dimensional Titanium Carbide (Ti3C2Tx MXene).* Chemistry of Materials, 2017. **29**(18): p. 7633-7644.

170. R. J. Spillane, *Keyboard Apparatus for Personal Identification.* Technical Disclosure Bulletin, 1975. **17**(3346).

171. Salil P Banerjee and Damon L Woodard, *Biometric authentication and identification using keystroke dynamics: A survey.* Journal of Pattern Recognition Research, 2012. **7**(1): p. 116-139.

172. Md Liakat Ali, John V. Monaco, Charles C. Tappert, and Meikang Qiu, *Keystroke Biometric Systems for User Authentication.* Journal of Signal Processing Systems, 2017. **86**(2): p. 175-190.

173. Fabian Monrose and Aviel D. Rubin, *Keystroke dynamics as a biometric for authentication.* Future Gener. Comput. Syst., 2000. **16**(4): p. 351-359.

174. William E. Burr, Donna F. Dodson, Elaine M. Newton, Ray A. Perlner, W. Timothy Polk, Sarbari Gupta, and Emad A. Nabbus, *SP 800-63-1. Electronic Authentication Guideline*. 2011, National Institute of Standards \& Technology.

175. R Stockton Gaines, William Lisowski, S James Press, and Norman Shapiro, *Authentication by keystroke timing: Some preliminary results*. 1980, RAND CORP SANTA MONICA CA.

176. A. Sulong, Wahyudi, and M. U. Siddiqi. *Intelligent keystroke pressure-based typing biometrics authentication system using radial basis function network*. in *2009 5th International Colloquium on Signal Processing & Its Applications*. 2009.

177. Hasimah Ali, Wahyudi, and M. J. E. Salami. *Keystroke pressure based typing biometrics authentication system by combining ANN and ANFIS-based classifiers*. in *2009 5th International Colloquium on Signal Processing & Its Applications*. 2009.

178. Chen Change Loy, W Lai, and C Lim, *Development of a pressure-based typing biometrics user authentication system.* ASEAN Virtual Instrumentation Applications Contest Submission, 2005.

179. S. S. Shen, S. H. Lin, T. H. Kang, and W. Chien. *Enhanced keystroke dynamics authentication utilizing pressure detection*. in *2016 International Conference on Applied System Innovation (ICASI)*. 2016.

180. Jun Chen, Guang Zhu, Jin Yang, Qingshen Jing, Peng Bai, Weiqing Yang, Xuewei Qi, Yuanjie Su, and Zhong Lin Wang, *Personalized Keystroke Dynamics for Self-Powered Human–Machine Interfacing.* ACS Nano, 2015. **9**(1): p. 105-116.

181. Corinna Cortes and Vladimir Vapnik, *Support-Vector Networks.* Machine Learning, 1995. **20**(3): p. 273-297.

182. Shengming Li, Wenbo Peng, Jie Wang, Long Lin, Yunlong Zi, Gong Zhang, and Zhong Lin Wang, *All-Elastomer-Based Triboelectric Nanogenerator as a Keyboard Cover To Harvest Typing Energy*. ACS Nano, 2016. **10**(8): p. 7973-7981.

183. François Baccelli and Bartłomiej Błaszczyszyn, *Stochastic geometry and wireless networks: Volume II Applications.* Foundations and Trends® in Networking, 2010. **4**(1–2): p. 1-312.

184. I. T. Jolliffe, *Choosing a Subset of Principal Components or Variables*, in *Principal Component Analysis*, I.T. Jolliffe, Editor. 2002, Springer New York: New York, NY. p. 111-149.

185. Chih-Chung Chang and Chih-Jen Lin, *LIBSVM: A library for support vector machines.* ACM Trans. Intell. Syst. Technol., 2011. **2**(3): p. 1-27.

186. Rong-En Fan, Pai-Hsuen Chen, and Chih-Jen Lin, *Working Set Selection Using Second Order Information for Training Support Vector Machines.* J. Mach. Learn. Res., 2005. **6**: p. 1889-1918.

187. Hsu Chih-Wei and Lin Chih-Jen, *A comparison of methods for multiclass support vector machines.* IEEE Transactions on Neural Networks, 2002. **13**(2): p. 415-425.

188. He Wang, Dimitrios Lymberopoulos, and Jie Liu, *Sensor-Based User Authentication*, in *Wireless Sensor Networks: 12th European Conference, EWSN 2015, Porto, Portugal, February 9-11, 2015. Proceedings*, T. Abdelzaher, N. Pereira, and E. Tovar, Editors. 2015, Springer International Publishing: Cham. p. 168-185.

189. Robert G. Gallager, *Poisson Processes*, in *Discrete Stochastic Processes*, R.G. Gallager, Editor. 1996, Springer US: Boston, MA. p. 31-55.

190. A. Zanella, N. Bui, A. Castellani, L. Vangelista, and M. Zorzi, *Internet of Things for Smart Cities.* IEEE Internet of Things Journal, 2014. **1**(1): p. 22-32.

191. F. Boccardi, R. W. Heath, A. Lozano, T. L. Marzetta, and P. Popovski, *Five disruptive technology directions for 5G.* IEEE Communications Magazine, 2014. **52**(2): p. 74-80.

192. E. Ferro and F. Potorti, *Bluetooth and Wi-Fi wireless protocols: a survey and a comparison.* IEEE Wireless Communications, 2005. **12**(1): p. 12-26.

193. Paolo Baronti, Prashant Pillai, Vince W. C. Chook, Stefano Chessa, Alberto Gotta, and Y. Fun Hu, *Wireless sensor networks: A survey on the state of the art and the 802.15.4 and ZigBee standards.* Computer Communications, 2007. **30**(7): p. 1655-1695.

194. A. Juels, *RFID security and privacy: a research survey.* IEEE Journal on Selected Areas in Communications, 2006. **24**(2): p. 381-394.

195. Gang Zhou, John A Stankovic, and Sang H Son, *Crowded spectrum in wireless sensor networks.* IEEE EmNets, 2006. **6**.

196. J. Bonin, C. Evci, and A. L. Sanders, *Securing spectrum through the ITU to fuel the growth of next-generation wireless technologies.* Bell Labs Technical Journal, 2013. **18**(2): p. 99-115.

197. J. Song, W. Ding, F. Yang, H. Yang, B. Yu, and H. Zhang, *An Indoor Broadband Broadcasting System Based on PLC and VLC.* IEEE Transactions on Broadcasting, 2015. **61**(2): p. 299-308.

198. L. Zeng, D. C. O' Brien, H. L. Minh, G. E. Faulkner, K. Lee, D. Jung, Y. Oh, and E. T. Won, *High data rate multiple input multiple output (MIMO) optical wireless communications using white led lighting.* IEEE Journal on Selected Areas in Communications, 2009. **27**(9): p. 1654-1662.

199. A. M. Street, P. N. Stavrinou, D. C. O'Brien, and D. J. Edwards, *Indoor optical wireless systems–a review.* Optical and Quantum Electronics, 1997. **29**(3): p. 349-378.

200. H. Elgala, R. Mesleh, and H. Haas, *Indoor optical wireless communication: potential and state-of-the-art.* IEEE Communications Magazine, 2011. **49**(9): p. 56-62.

201. L. Grobe, A. Paraskevopoulos, J. Hilt, D. Schulz, F. Lassak, F. Hartlieb, C. Kottke, V. Jungnickel, and K. Langer, *High-speed visible light communication systems.* IEEE Communications Magazine, 2013. **51**(12): p. 60-66.

202. Sujan Rajbhandari, Zabih Ghassemlooy, and Maia Angelova, *Experimental wavelet based denoising for indoor infrared wireless communications.* Optics Express, 2013. **21**(11): p. 13779-13784.

203. P. Brandl, R. Enne, T. Jukić, and H. Zimmermann, *OWC Using a Fully Integrated Optical Receiver With Large-Diameter APD.* IEEE Photonics Technology Letters, 2015. **27**(5): p. 482-485.

204. P. Luo, M. Zhang, Z. Ghassemlooy, H. Le Minh, H. Tsai, X. Tang, L. C. Png, and D. Han, *Experimental Demonstration of RGB LED-Based Optical Camera Communications.* IEEE Photonics Journal, 2015. **7**(5): p. 1-12.

205. Xing Fan, Jun Chen, Jin Yang, Peng Bai, Zhaoling Li, and Zhong Lin Wang, *Ultrathin, Rollable, Paper-Based Triboelectric Nanogenerator for Acoustic Energy Harvesting and Self-Powered Sound Recording.* ACS Nano, 2015.

206. C. E. Shannon, *Communication in the Presence of Noise.* Proceedings of the IRE, 1949. **37**(1): p. 10-21.

207. S. B. Kotsiantis, I. D. Zaharakis, and P. E. Pintelas, *Machine learning: a review of classification and combining techniques.* Artificial Intelligence Review, 2006. **26**(3): p. 159-190.

208. Anyin Li, Yunlong Zi, Hengyu Guo, Zhong Lin Wang, and Facundo M. Fernández, *Triboelectric nanogenerators for sensitive nano-coulomb molecular mass spectrometry.* Nature Nanotechnology, 2017. **12**: p. 481.

209. Chang Bao Han, Tao Jiang, Chi Zhang, Xiaohui Li, Chaoying Zhang, Xia Cao, and Zhong Lin Wang, *Removal of Particulate Matter Emissions from a Vehicle Using a Self-Powered Triboelectric Filter.* ACS Nano, 2015. **9**(12): p. 12552-12561.

210. Jinhui Nie, Zewei Ren, Jiajia Shao, Chaoran Deng, Liang Xu, Xiangyu Chen, Meicheng Li, and Zhong Lin Wang, *Self-Powered Microfluidic Transport System Based on Triboelectric Nanogenerator and Electrowetting Technique.* ACS Nano, 2018. **12**(2): p. 1491-1499.

211. Jia Cheng, Wenbo Ding, Yunlong Zi, Yijia Lu, Linhong Ji, Fan Liu, Changsheng Wu, and Zhong Lin Wang, *Triboelectric microplasma powered by mechanical stimuli.* Nature Communications, 2018. **9**(1): p. 3733.

212. Xiangyu Chen, Tao Jiang, Yanyan Yao, Liang Xu, Zhenfu Zhao, and Zhong Lin Wang, *Stimulating Acrylic Elastomers by a Triboelectric Nanogenerator – Toward Self-Powered Electronic Skin and Artificial Muscle.* Advanced Functional Materials, 2016. **26**(27): p. 4906-4913.

213. Xiangyu Chen, Yali Wu, Aifang Yu, Liang Xu, Li Zheng, Yongsheng Liu, Hexing Li, and Zhong Lin Wang, *Self-powered modulation of elastomeric optical grating by using triboelectric nanogenerator.* Nano Energy, 2017. **38**: p. 91-100.

214. Li Zheng, Yali Wu, Xiangyu Chen, Aifang Yu, Liang Xu, Yongsheng Liu, Hexing Li, and Zhong Lin Wang, *Self-Powered Electrostatic Actuation Systems for Manipulating the Movement of both Microfluid and Solid Objects by Using Triboelectric Nanogenerator.* Advanced Functional Materials, 2017. **27**(16): p. 1606408.

215. Congju Li, Yingying Yin, Bin Wang, Tao Zhou, Jiaona Wang, Jianjun Luo, Wei Tang, Ran Cao, Zuqing Yuan, Nianwu Li, Xinyu Du, Chunru Wang, Shuyu Zhao, Yuebo Liu, and Zhong Lin Wang, *Self-Powered Electrospinning System Driven by a Triboelectric Nanogenerator.* ACS Nano, 2017. **11**(10): p. 10439-10445.

216. Yunlong Zi, Changsheng Wu, Wenbo Ding, Xingfu Wang, Yejing Dai, Jia Cheng, Jiyu Wang, Zhengjun Wang, and Zhong Lin Wang, *Field Emission of Electrons Powered by a Triboelectric Nanogenerator.* Advanced Functional Materials, 2018. **28**(21): p. 1800610.

217. Ingram Taylor Geoffrey, *Disintegration of water drops in an electric field.* Proceedings of the Royal Society of London. Series A. Mathematical and Physical Sciences, 1964. **280**(1382): p. 383-397.

218. Ioan Marginean, Lida Parvin, Linda Heffernan, and Akos Vertes, *Flexing the Electrified Meniscus: The Birth of a Jet in Electrosprays.* Analytical Chemistry, 2004. **76**(14): p. 4202-4207.

219. Jang-Ung Park, Matt Hardy, Seong Jun Kang, Kira Barton, Kurt Adair, Deep kishore Mukhopadhyay, Chang Young Lee, Michael S. Strano, Andrew G. Alleyne, John G. Georgiadis, Placid M. Ferreira, and John A. Rogers, *High-resolution electrohydrodynamic jet printing.* Nature Materials, 2007. **6**: p. 782.

220. Ke Wang, Mark D. Paine, and John P. W. Stark, *Fully voltage-controlled electrohydrodynamic jet printing of conductive silver tracks with a sub-100 μm linewidth.* Journal of Applied Physics, 2009. **106**(2): p. 024907.

221. Lee Dae-Young, Lee Jae-Chang, Shin Yun-Soo, Park Sung-Eun, U. Yu Tae, Kim Yong-Jun, and Hwang Jungho, *Structuring of conductive silver line by electrohydrodynamic jet printing and its electrical characterization.* Journal of Physics: Conference Series, 2008. **142**(1): p. 012039.

222. Jang-Ung Park, Jung Heon Lee, Ungyu Paik, Yi Lu, and John A. Rogers, *Nanoscale Patterns of Oligonucleotides Formed by Electrohydrodynamic Jet Printing with Applications in Biosensing and Nanomaterials Assembly.* Nano Letters, 2008. **8**(12): p. 4210-4216.

223. Bong Hoon Kim, M. Serdar Onses, Jong Bin Lim, Sooji Nam, Nuri Oh, Hojun Kim, Ki Jun Yu, Jung Woo Lee, Jae-Hwan Kim, Seung-Kyun Kang, Chi Hwan Lee, Jungyup Lee, Jae Ho Shin, Nam Heon Kim, Cecilia Leal, Moonsub Shim, and John A. Rogers, *High-Resolution Patterns of Quantum Dots Formed by Electrohydrodynamic Jet Printing for Light-Emitting Diodes.* Nano Letters, 2015. **15**(2): p. 969-973.

224. Kukjoo Kim, Gyeomuk Kim, Bo Ram Lee, Sangyoon Ji, So-Yun Kim, Byeong Wan An, Myoung Hoon Song, and Jang-Ung Park, *High-resolution electrohydrodynamic jet printing of small-molecule organic light-emitting diodes.* Nanoscale, 2015. **7**(32): p. 13410-13415.

225. Changsheng Wu, Halil Tetik, Jia Cheng, Wenbo Ding, Hengyu Guo, Xingtian Tao, Nanjia Zhou, Yunlong Zi, Zhiyi Wu, Huixuan Wu, Dong Lin, and Zhong Lin Wang, *Electrohydrodynamic Jet Printing Driven by a Triboelectric Nanogenerator.* Advanced Functional Materials, 2019: p. 1901102.

226. C. H. Chen, D. A. Saville, and I. A. Aksay, *Scaling laws for pulsed electrohydrodynamic drop formation.* Applied Physics Letters, 2006. **89**(12): p. 124103.

227. Yuan Xin and Xiong Zhenhua, *High frequency pulsed electrohydrodynamic printing with controllable fine droplets.* Journal of Micromechanics and Microengineering, 2018. **28**(9): p. 095008.

228. S. Mishra, K. L. Barton, A. G. Alleyne, P. M. Ferreira, and J. A. Rogers, *High-speed and drop-on-demand printing with a pulsed electrohydrodynamic jet.* Journal of Micromechanics and Microengineering, 2010. **20**(9): p. 095026.

229. Jungkeun Yang, Baekhyun Cho, and Jaewon Chung, *Optimization of pulsed voltage waveform for electrohydrodynamic jetting on-demand.* Journal of Mechanical Science and Technology, 2018. **32**(8): p. 3775-3786.

230. R. A. Millikan and Carl F. Eyring, *Laws Governing the Pulling of Electrons out of Metals by Intense Electrical Fields.* Physical Review, 1926. **27**(1): p. 51-67.

231. F. R. S. R. H. Fowler, Dr. L. Nordheim, *Electron emission in intense electric fields.* Proceedings of the Royal Society of London. Series A, 1928. **119**(781): p. 173.

232. C. Kleint, *On the early history of field emission including attempts of tunneling spectroscopy.* Progress in Surface Science, 1993. **42**(1): p. 101-115.

233. Christian Kleint, *Comments and references relating to early work in field electron emission.* Surface and Interface Analysis, 2004. **36**(5-6): p. 387-390.

234. A. V. Crewe, M. Isaacson, and D. Johnson, *A Simple Scanning Electron Microscope.* Review of Scientific Instruments, 1969. **40**(2): p. 241-246.

235. T. M. Mayer, D. P. Adams, and B. M. Marder, *Field emission characteristics of the scanning tunneling microscope for nanolithography.* Journal of Vacuum Science & Technology B: Microelectronics and Nanometer Structures Processing, Measurement, and Phenomena, 1996. **14**(4): p. 2438-2444.

236. Q. H. Wang, A. A. Setlur, J. M. Lauerhaas, J. Y. Dai, E. W. Seelig, and R. P. H. Chang, *A nanotube-based field-emission flat panel display.* Applied Physics Letters, 1998. **72**(22): p. 2912-2913.

237. P. H. Cutler, N. M. Miskovsky, P. B. Lerner, and Moon S. Chung, *The use of internal field emission to inject electronic charge carriers into the conduction band of diamond films: a review.* Applied Surface Science, 1999. **146**(1): p. 126-133.

238. Walt A. de Heer, A. Châtelain, and D. Ugarte, *A Carbon Nanotube Field-Emission Electron Source.* Science, 1995. **270**(5239): p. 1179.

239. Shoushan Fan, Michael G. Chapline, Nathan R. Franklin, Thomas W. Tombler, Alan M. Cassell, and Hongjie Dai, *Self-Oriented Regular Arrays of Carbon Nanotubes and Their Field Emission Properties.* Science, 1999. **283**(5401): p. 512.

240. S. H. Jo, D. Banerjee, and Z. F. Ren, *Field emission of zinc oxide nanowires grown on carbon cloth.* Applied Physics Letters, 2004. **85**(8): p. 1407-1409.

241. J. Zhou, N. S. Xu, S. Z. Deng, J. Chen, J. C. She, and Z. L. Wang, *Large-Area Nanowire Arrays of Molybdenum and Molybdenum Oxides: Synthesis and Field Emission Properties.* Advanced Materials, 2003. **15**(21): p. 1835-1840.

242. Jun Chen, S. Z. Deng, N. S. Xu, Suhua Wang, Xiaogang Wen, Shihe Yang, Chunlei Yang, Jiannong Wang, and Weikun Ge, *Field emission from crystalline copper sulphide nanowire arrays.* Applied Physics Letters, 2002. **80**(19): p. 3620-3622.

243. J. H He, R. S Yang, Y. L Chueh, L. J Chou, L. J Chen, and Z. L Wang, *Aligned AlN Nanorods with Multi-tipped Surfaces—Growth, Field-Emission, and Cathodoluminescence Properties.* Advanced Materials, 2006. **18**(5): p. 650-654.

244. C. X. Xu and X. W. Sun, *Field emission from zinc oxide nanopins.* Applied Physics Letters, 2003. **83**(18): p. 3806-3808.

245. Richard G. Forbes, *Physics of generalized Fowler-Nordheim-type equations.* Journal of Vacuum Science & Technology B: Microelectronics and Nanometer Structures Processing, Measurement, and Phenomena, 2008. **26**(2): p. 788-793.

246. C. J. Lee, T. J. Lee, S. C. Lyu, Y. Zhang, H. Ruh, and H. J. Lee, *Field emission from well-aligned zinc oxide nanowires grown at low temperature.* Applied Physics Letters, 2002. **81**(19): p. 3648-3650.

247. X. D Wang, J. Zhou, C. S Lao, J. H Song, N. S Xu, and Z. L Wang, *In Situ Field Emission of Density-Controlled ZnO Nanowire Arrays.* Advanced Materials, 2007. **19**(12): p. 1627-1631.

248. Y. K. Tseng, C. J. Huang, H. M. Cheng, I. N. Lin, K. S. Liu, and I. C. Chen, *Characterization and Field-Emission Properties of Needle-like Zinc Oxide Nanowires Grown Vertically on Conductive Zinc Oxide Films.* Advanced Functional Materials, 2003. **13**(10): p. 811-814.

249. Philip G. Collins and A. Zettl, *A simple and robust electron beam source from carbon nanotubes.* Applied Physics Letters, 1996. **69**(13): p. 1969-1971.

250. Yunlong Zi, Hengyu Guo, Jie Wang, Zhen Wen, Shengming Li, Chenguo Hu, and Zhong Lin Wang, *An inductor-free auto-power-management design built-in triboelectric nanogenerators.* Nano Energy, 2017. **31**: p. 302-310.

251. Ai Leen Koh, Emily Gidcumb, Otto Zhou, and Robert Sinclair, *The dissipation of field emitting carbon nanotubes in an oxygen environment as revealed by in situ transmission electron microscopy.* Nanoscale, 2016. **8**(36): p. 16405-16415.

252. Zhi Xu, X. D. Bai, E. G. Wang, and Zhong L. Wang, *Field emission of individual carbon nanotube with in situ tip image and real work function.* Applied Physics Letters, 2005. **87**(16): p. 163106.